Alma Mater Studiorum - Università di Bologna

DOTTORATO DI RICERCA IN
BIOLOGIA CELLULARE E MOLECOLARE

Ciclo XXIX

Settore Concorsuale di afferenza: 05/D1

Settore Scientifico disciplinare: SSD BIO/09 - Fisiologia

Organic bio-electronics for interfacing, stimulating and recording of neural cells

Presentata da: **Saskia Katharina Karges**

Coordinatore Dottorato
Prof. Giovanni Capranico

Relatore
Prof. Barbara Monti

Co-relatore
Prof. Marco Caprini
Dr. Valentina Benfenati

Esame finale anno 2017

If you can dream it, you can do it.

— Walt Disney

Dedicated to my family.

ABSTRACT

One of the main reasons for the difficulty of providing a treatment of a huge number of disorders and diseases, especially for a complex organ as the brain, is the lack of deeper insight on how it actually works. And even after centuries of research, at present there are no efficient tools at hand to create this deeper insight yet. Recently, an increasing attention is focused on an emerging interdisciplinary field called organic bioelectronics, aimed at engineering, fabrication and characterization of improved biocompatible, conformable and low cost processing devices that enable stimulation and recording of neural cells *in vitro* and *in vivo*, providing an unprecedented insight into the brain's physiology and pathophysiology. These new devices are hot candidates in order to create efficient tools for research and diagnosis and to establish a working 'machine-to-brain' communication.

Still there is a lot of room for improvement in the used materials, for example in the biocompatibility. To this aim, a novel quaterthiophene (T4) semiconductor, covalently modified with lysine- ends (T4Lys), was fabricated and characterized, rendering additional surface coating unnecessary. The material was then tested as interface for DRG primary neurons. By whole-cell patch-clamp, it was examined if the biofunctionality of neurons cultured on T4Lys was preserved and if T4Lys as an organic interface enabled functional differentiation of DRG primary neurons.

Not only neurons but also astrocytes, their ion channels and calcium signalling play a crucial role in the physiology and pathophysiology of the central nervous system. In this context novel tools are needed to also monitor and/or modulate the astrocytic biochemical and bioelectrical activity. To this end, an organic field effect transistor device (O-CST), previously reported to enable real-time recording and manipulation of communication signals of primary neurons, was interfaced with primary astroglial cells. In this context the biocompatibility of the organic material P13 and its preservation of the astrocytic electrophysiological properties *in vitro* was investigated, and the impact of a P13-based organic field effect transistor on the astrocytic ionic conductance studied. The evoked astrocytic response to device stimulation was bio-physically and pharmacologically characterized and the necessity of device integrity investigated.

PUBLICATIONS

Some ideas and figures have appeared previously in the following publications on which this thesis is based on:

I S. Bonetti, A. Pistone, M. Brucale, **S. Karges**, L. Favaretto, M. Zambianchi, T. Posati, A. Sagnella, M. Caprini, S. Toffanin, R. Zamboni, N. Camaioni, M. Muccini, M. Melucci, V. Benfenati: A Lysinated Thiophene-Based Semiconductor as a Multifunctional Neural Bioorganic Interface. Adv. Healthcare Mater, 2014, 00, 1-12

II A. I. Borrachero-Conejo, S. Bonetti, **S. Karges**, A. Pistone, S. D. Quiroga, M. Natali, M. Muccini, S. Toffanin, I. Grishin, S. Pecqueur, G. Generali, M. Caprini, V. Benfenati: An organic transistor architecture for stimulation of calcium signalling in primary rat cortical astrocytes. Proceedings of the 15th IEEE International Conference on Nanotechnology July 27-30, 2015, Rome, Italy, 1532-1534

III S. Bonetti, M. Prosa, A. Pistone, L. Favaretto, A. Sagnella, I. Grisin, M. Zambianchi, **S. Karges**, A. Lorenzoni, T. Posati, R. Zamboni, N. Camaioni, F. Mercuri, M. Muccini, M. Melucci and V. Benfenati: A Self-assembled Lysinated Perylene Diimide Film as Multifunctional Material for Neural Interfacing. J. Mater. Chem. B, 2016, 4, 2921-2932

IV **S. Karges**, A.I. Borrachero-Conejo, S. Bonetti, A. Pistone, I. Grishin, S. Pecqueur, G. Donati, S.D. Quiroga, G. Generali, M. Caprini, S. Toffanin, F. Mercuri, M. Muccini, V. Benfenati: Organic cell stimulator and sensing transistor architecture stimulates TRPV4 mediated calcium signaling and whole-cell conductance in primary cortical astrocytes. (in preparation)

ACKNOWLEDGEMENTS

I would like to thank...

Valentina Benfenati (CNR-ISOF), Michele Muccini (CNR-ISMN) and Giampiero Ruani (CNR-ISMN) for the possibility to do my PhD in their laboratory at CNR-ISMN.

The OLIMPIA-project (EU-FP7-2012-PEOPLE-ITN Marie Curie Actions Grant Agreement 316832) for funding.

Prof. Marco Caprini (University of Bologna) for reviewing my PhD work.

Prof. Barbara Monti (University of Bologna) for reviewing my PhD work.

Prof. Stefano Ferroni (University of Bologna) for excellent advice.

My colleagues from CNR Francesco, Tamara, Mario, Emanuela, Assunta, Simone, Anna and Ana; Ilja, Sebastien and Eric from E.T.C. srl and Jarmila and Alessia from UniBo for the great time in the lab, the office, the fun and your help.

The collaborators from different CNR research groups: Francesco Mercuri, Stefano Toffanin, Gianluca Generali and Alessandro Tugnoli.

The OLIMPIA-fellows for the discussions, fun and the great time.

The teams of Histocell and the IIT in Milan for the great internship-time.

My friends in Bologna, Germany and all over the world.

My family for their loving support and help, for infinite patience, even in the hard times. Thank you for always believing in me.

CONTENTS

ACRONYMS

4α PDD 4α -phorbol 12,13-didecanoate

AHP After hyperpolarization period

ArAc Arabinofuranosyl cytidine

AQP4 Aquaporin 4

AP Action potential

ATP Adenosine triphosphate

Au Gold

CBX Carbenoxolone

CNS Central nervous system

CVD Chemical vapor deposition

DAG Diacylglycerol

div Days in vitro

DMEM Dulbecco's Modified Eagle's medium

DNA Deoxyribonucleic acid

DRG Dorsal root ganglion

E Battery

ECoG Electrocorticography

EDTA Ethylenediamine tetraacedic acid

EEG Electroencephalography

EGTA Ethylene glycol-bis(2-aminoethylether)-N,N,N′,N′-tetraacetic acid

EtOH Ethanol

FBS Fetal bovine serum

FDA Fluorescin diacetate

FET Field effect transistor

Fig. Figure

g Gram

G Conductance

GABA Gamma-aminobutyric acid

GAP43 Growth associated protein 43

GPCR G-protein coupled receptors

h Hour(s)

HEPES N-2-Hydroxyethylpiperazin-N′-2-ethane sulfonic acid

Hz Hertz

I Current

iGLUR Ionotropic glutamate receptor

IP3 Inositol 1,4,5 Triphosphate

ITO Indium Tin Oxide

l Liter

LED Light emitting diode

LSCM Laser scanning confocal microscopy

M Molar [mol/l]

MEA Multielectrode array

mGLUR Metabotropic glutamate receptor

min Minutes

ms Milliseconds

mV Milllivolt

N normal

nA Nanoampere

nm Nanometer

NGF Nerve growth factor

NeuN Neuronal nuclear protein

O-CST Organic cell stimulating and sensing transistor

OECT Organic electrochemical transistor

OFET Organic field effect transistor

OTFT Organic Thin Film Transistor

P13 N,N′-Ditridecylperylene-3,4,9,10-tetracarboxylic diimide

P2Y Family of purinergic G protein-coupled receptors

P3HT Poly(3-hexylthiophene)

p.a. pro analysis

pA Picoampere

PBS Phosphate buffered saline

PCBM [6,6]-phenyl-C61-butyric acid methyl ester

PDI Perylene diimide

PDI-Lys Perylene diimide bearing lysine end substituents

PDL Poly-D-Lysine

PEDOT Poly-3,4-ethylenedioxythiophene

PenStrep Penicillin-Streptomycin

PLL Poly-L-Lysine

PIP2 Phosphatidylinositol 4,5-bisphosphate

PMMA Polymethylmethactrylate

PSS Polystyrene sulfonate

PVD Physical vapor deposition

RNA Ribonucleic acid

rpm Revolutions per minute

RR Ruthenium Red

RT Room temperature

RVD Regulatory volume decrease

SEEG Stereoelectroencephalography

T4 Tetrathiophene

T4Lys Tetratiophene bearing Lysine-ends

TRP Transient receptor potential

TRPA1 Transient receptor potential channel, subfamily A, member 1

TRPC Transient receptor potential channel, subfamily C

TRPV4 Transient receptor potential channel, subfamily V, member 4

UV Ultraviolet

V Volt

V_h Holding potential

V_{mem} Membrane potential

VGCC Voltage gated calcium channels

WHO World Health Organization

Part I

INTRODUCTION

1 MOTIVATION

1.1 MOTIVATION

The human brain is probably the most complex of organs and understanding how it works is one of the greatest challenges science and engineering are facing. But the brain was not always held in high regard: perhaps the most stunning and best known feature of the ancient Egyptian mummification is the neglect of the brain. When creating a mummy, the brain was often removed transnasally and thrown away, while the other internal organs were carefully preserved [1]. The Greek philosopher Aristotle attributed the location of intelligence and thought to the heart, while the brain would serve as a cooling agent for body heat. The birth of neuroscience might have begun in the 4th century BC with a contemporary of Aristotle: Hippocrates, one of the most influential medical doctors of all times. Hippocrates identified the brain as the seat of thought, perception, consciousness and the center of intelligence and emotion [2, 3]. It was an historic step, but a deeper insight and a first understanding of the brain's anatomy and function took a long time to follow. Instead, neuroscience was more than once on the wrong track, among which Galen's fluid filled ventricle theories of the brain dominated until well into the 17th century [4].

Centuries later, mankind has made important progress in the understanding of biological systems, body functions and the generation of diseases. Still a complete understanding of the function of the brain, the constant interaction of 50-100 billion neurons or their tasks, the involvement of astrocytes in memory and signalling remains and the pathophysiology of a huge number of disorders and diseases remain to be explored [5].

The WHO World Health report of 2001 states that one in four people worldwide will be affected by mental or neurological disorders at some point in their lives [6]. For 2015, the Alzheimer's association expected an estimated number of 5.3 million Americans to have Alzheimer's disease [7]. The WHO report *Neurological disorders: public health challenges* of 2006 lists the prevalence of neurological disorders by cause (including epilepsy, dementia, Parkinson's disease, multiple sclerosis, migraine and others) predicting for 2015 worldwide 148 out of 1000 people affected by any of these disorders. A figure that has to be seen in the context of more than 7 billion people currently living on the planet - and this number is increasing [8].

Even though great efforts have been taken and scientific progress has been made, for many of these brain-based pathologies, neither a cure nor an effective treatment or prevention has been found to date. One of the main reasons for the difficulty of providing a treatment, especially for a complex organ as the brain, is the lack of deeper insight on how it actually works. On the other hand at present, research and medicine have no efficient tools at hand to create this deeper insight yet [5].

Constructing these efficient tools to develop a working 'machine-to-brain' communication is the challenge of translating the "electron" world of electronic devices into the biological "ionic" world [9].

Recently, an increasing attention is focused on an emerging interdisciplinary field called organic bioelectronics, aimed at engineering, fabrication and characterization of improved biocompatible, conformable and low cost processing devices that enable the stimulation and recording of neural cells *in vitro* and *in vivo*, seeking to enable an unprecedented insight into the brain's physiology and pathophysiology and to become a stepping stone in bridging the brain to the world.

1.2 THESIS OUTLINE

To date, all currently available bio-electronic approaches still require additional treatment of the semiconductor surface to enable cell adhesion. Based on data provided on inorganic neuro-electronic interfaces, it is plausible to suppose that this additional surface coating might cause a decrease of the recording sensibility of organic interfaces, by increasing the cleft distance between electrodes and cells [10, 11, 12]. To this aim, a novel quaterthiophene (T_4) semiconductor covalently modified with lysine-ends (T4Lys) was fabricated and characterized, rendering additional surface coating unnecessary. The material was then tested as interface for DRG primary neurons. By whole-cell patch-clamp, I tested if

- the biofunctionality of neurons cultured on T4Lys was preserved
- and if T4Lys as an organic interface enabled functional differentiation of DRG primary neurons

as described in Chapter 4.

Not only neurons but also astrocytes, their ion channels and calcium signalling, play a crucial role in the physiology and pathophysiology of the central nervous system. Taking this importance of astrocytes in the brain and their involvement in a broad range of diseases and disorders into account, novel tools to monitor and modulate also astrocytic biochemical and bioelectrical activity *in vitro* and *in vivo* is a demand not met by the currently available technology. The group of Dr. Valentina Benfenati at the CNR in Bologna previously reported on transparent Organic Cell Stimulating and Sensing Transistors (O-CSTs) capable of providing bidirectional stimulation and recording of primary DRG neurons. These organic devices were fabricated with a bottom-gate top-contact transistor architecture and N, N'-ditridecylperylene-3,4,9,10-tetracarboxylic diimide (P13) as semiconducting and capping layer [13, 14]. However the possibility to use the introduced O-CST device to monitor and manipulate also astroglial ion channel conductance and calcium signaling remained to be elucidated.

To this end, I

- investigated the biocompatibility of P13 and its preservation of the astrocytic electrophysiological properties *in vitro*,
- studied the impact of a P13-based organic field effect transistor on the astrocytic ionic conductance,

- bio-physically and pharmacologically characterized the evoked astrocytic response to device stimulation,
- investigated the necessity of device integrity for the obtained astrocytic response,
- studied the astrocytic calcium response to device operation

as described in Chapter 5.

All activities were developed thanks to the collaboration with a broad team of researchers of institutes CNR-ISMN and CNR-ISOF in Bologna, E.T.C srl as well as the institute of physiology within the department of pharmacy and biotechnology (FaBiT) of the University of Bologna.

1.3 THE OLIMPIA PROJECT

The research for this thesis was funded by the OLIMPIA project under EU-FP7-2012-PEOPLE-ITN Marie Curie Actions Grant Agreement 316832. OLIMPIA was a training network initiative built on research and development of innovative organic optoelectronic devices, interfaced and integrated with living systems. The living systems of choice were neural cells (astrocytes and neurons) to be interfaced and integrated *in vitro* and *in vivo* with different organic electronic and optoelectronic devices. The OLIMPIA research was aimed to provide radically new understanding of neural cell-cell communication processes and to have an impact on a wide variety of fields, from biomedical research to neuro-regenerative medicine. The OLIMPIA consortium was both: interdisciplinary and intersectorial. The consortium combined 9 partners belonging to 6 European countries from academia, public research centers and industrial laboratories.

The specific scientific and technical objectives of OLIMPIA, to be achieved through an intensive collaborative research program detailed in the next sections, were:

- To develop and fully characterize organic optoelectronic devices suitable for operation in physiological aqueous environment.
- To investigate thin film structures and organic optoelectronic devices that preserve glial cells and neuron bioelectrical functionality *in vitro* and/or *in vivo*.
- To fabricate organic optoelectronic devices integrated with neural cells capable of providing stimulation and transduction of neural cells bioelectrical activity *in vitro* and/or *in vivo*.
- To explore the potential application of organic devices as diagnostic tool for epilepsy and neuro-regenerative medicine.

OLIMPIA activities were aimed at getting a fundamental understanding of the mutual interaction between organic optoelectronic materials and devices and neurobiology. The research approach conceives the living systems of neural cells as integrated and interactive components of the device [15].

2

BIOELECTRONIC INTERFACES

2.1 THE IONIC BASIS OF MEMBRANE POTENTIALS

In 1952, Hodgkin and Huxley recorded sodium currents (I_{Na}) for the first time, using their voltage-clamp technique on the squid giant axon. They inserted electrodes into these giant neurons and measured so the membrane potential in rest and during excitation. They developed a mathematical model (see figure 1) of the ion flux of K^+ and Na^+ through the axon membrane, based on their finding that the membrane potential and the ionic currents were correlated. In their model, the different elements of the cell membrane were regarded as electrical elements. The lipid bilayer of the membrane was thought as a capacitor, voltage-gated K^+ and Na^+ channels were represented as non-linear electrical conductances, leak channels as linear ones [16].

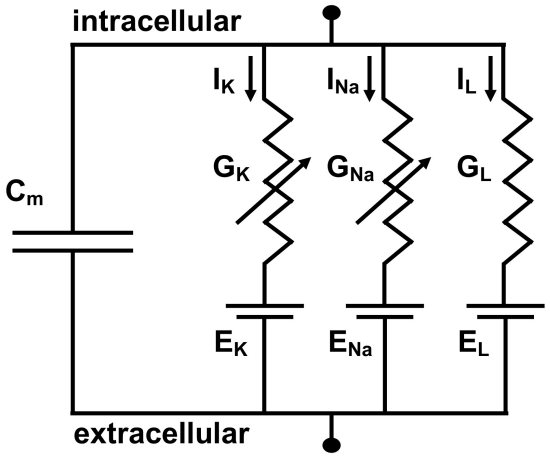

Figure 1: Scheme of the equivalent circuit of the Hodgkin-Huxley model for the membrane of a giant squid axon, representing the biophysical characteristic of cell membranes. The lipid bilayer is represented as a capacitance (C_m) in this model. Voltage-gated ion channels are represented as nonlinear (G_K, G_{Na}), leak ion channels as linear (G_L) conductances, respectively. The electrochemical gradients driving the flow of ions are represented as batteries (E). (Modified from [16])

At that time, the detection of the actual charge movement was technically impossible, still Hodgkin and Huxley deducted that there must be an ion flux across the membrane for each movable membrane charge. They proposed that this transmembrane flux was happening at "active patches" in the membrane. These "active patches" were later found to be voltage-gated K^+ and Na^+ channels. Based on this work, Hodgkin and Keynes found that these currents could be best explained if ions were passing through narrow pores, which they named channels [17]. Finally with the invention of the patch-clamp technique by Neher and Sakmann in 1976, it was possible to measure also currents through single ion channels [18].

In nerve cells, muscle fibers and cardiomyocytes, electrical signals are generated by changing the permeability of the cell membrane to ions. Changes in the membrane permeability, which means changing the open/close state of the membrane ion channels, allows ions to move across the membrane, following their electrochemical gradient. At rest, a cell has a steady electrical potential across the plasma membrane with the intracellular space being more negative with respect to the extracellular space.

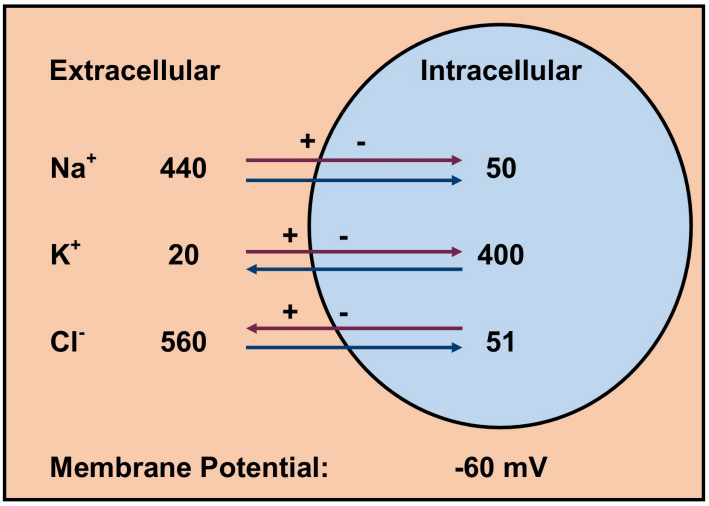

Figure 2: Ion distributions in a model cell of the giant squid axon. The cell membrane is here permeable to K^+, Na^+ and Cl^-, but impermeable to organic anions (A^-) within the cell. With the given ion concentrations (in mM), and a relative cell permeability for K^+, Na^+ and Cl^- of 1.00 : 0.04 : 0.45 the membrane potential calculated with equation 1 is around -60 mV at 20°C. The blue arrows indicate the ion flux direction according to the concentration gradient, the red arrows along the electrical gradient. In a cell in the resting state, these two forces are in equilibrium and the net flux is zero. (Modified from [19])

In figure 2, a model cell for the giant squid axon is shown, with given ion concentrations for K^+, Na^+ and Cl^-. Following the concentration gradient (blue arrows), potassium diffuses out of the cell, while sodium and chloride diffuse in. The membrane potential can be exactly in balance so there is no net flux across the membrane - this membrane potential is composed of the equilibrium potentials of the present ions. In order to maintain the concentration gradients between the intra- and extracellular space, the Na/K ATPase transports K^+ and Na^+ ions actively under the use of ATP against their concentration gradients [19].

$$V_{mem} = \frac{RT}{F} \log \frac{\rho_K [K]_o + \rho_{Na} [Na]_o + \rho_{Cl} [Cl]_i}{\rho_K [K]_i + \rho_{Na} [Na]_i + \rho_{Cl} [Cl]_o} \tag{1}$$

The Nernst equation can be used to calculate the equilibrium potential of each ion and of the whole cell, once the ion concentration gradients across various membranes are known. A modification of it, the so called Goldman-Hodgkin-Katz equation (equation 1, derives the membrane potential (V_{mem}) instead of equilibrium potentials and conductances from ion concentrations inside $[A]_i$ and outside $[A]_o$ the cell together with the membrane permeability (ρ) for each ion. R is the universal gas

constant, T the temperature and F the Faraday constant. Increasing the concentration of one ion or its permeability leads in turn to a change of the membrane potential [20, 21].

2.2 ELECTROPHYSIOLOGICAL SIGNALS OF NEURAL CELLS

2.2.1 *Ion Channels and action potentials in neuronal cells*

Neurons and other excitable cells communicate by sequences of fixed-size electrical impulses that are called action potentials. An action potential is a short-lasting (about 5 ms) localized change in the electrical potential of the cell membrane. The membrane potential of an excitable cell thereby rapidly rises and falls, following a consistent trajectory. A schematic representation is shown in figure 3 with a brief description of an action potential's different phases and the involved ion channels. In neuronal cells, action potentials are transmitting the excitement along the axon for cell-to-cell communication. Over a certain threshold, an action potential is unstoppable released following the "all or none"-law [22, 23].

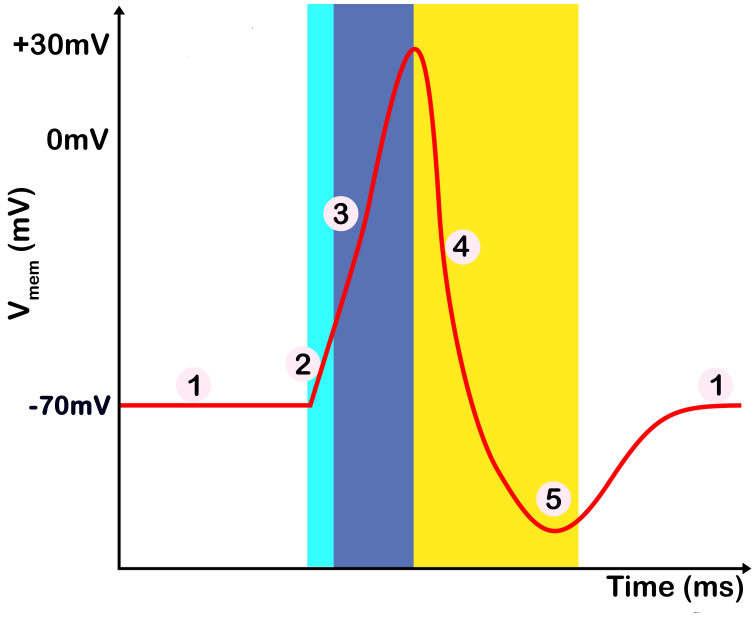

Figure 3: Schematic representation of an action potential (red line). (1) Membrane potential in the resting state, (2) voltage threshold leading to firing of an action potential due to the opening of voltage-gated Na^+ channels (blue background) and influx of Na^+-ions, (3) depolarization phase, the cell membrane depolarizes further by opening of more Na^+-channels (purple background). In the repolarization phase (4), voltage-gated K^+-channels are opening (yellow background), permitting a K^+-efflux, while the voltage-gated Na^+-channels are closed. The strong efflux of K^+-ions is leading to an undershoot or hyperpolarization (5) of the membrane potential, preventing the cell from firing again. The closing of the voltage-gated K^+-channels and voltage-gated Na^+-channels returning to the resting state allows the membrane to restore the resting potential (1), which is maintained by the K^+-Na^+-pump until further firing of the cell. Modified from [24, 25].

The ability of neurons to conduct, transmit, and receive information in form of electric signals results from the opening and closing of specific ion channels. One of

the key players in excitable cells in general are voltage-gated sodium channels (Na_V). Na_V are deactivated at negative potentials around the resting membrane potential of about -70 mV [16, 23].

Membrane depolarization leads to a fast influx of sodium ions which causes a reversion of the plasma membrane polarity. This depolarization in turn rapidly inactivates Na_V within a few milliseconds. As the Na^+-channels close, sodium ions can no longer enter the neuron, and they are actively transported out of the plasma membrane. K^+-channels are then activated and the K^+-outward current is returning the electrochemical gradient to the resting state. In order to prevent an action potential from traveling back, the membrane potential undergoes a transient negative shift, called hyper-polarization or refractory period. It occurs due to the combination of closed sodium and open potassium channels, when the re-polarization is heading towards the equilibrium potential of potassium ions (-75 mV) [26, 27, 28]. The closing of the voltage-gated K^+-channels and voltage-gated Na^+-channels returning to the resting state allows the membrane to restore the resting potential, which is maintained by the K^+-Na^+-ATPase until further firing of the cell.

2.2.2 *Ion channels and Calcium signalling in astrogial cells*

After their discovery, astroglial cells were long regarded as merely supportive glue within the central nervous system (CNS) [29]. This then common opinion slowly changed with the finding of a large number of G-protein coupled receptors (GPCRs) among other receptors for neurotransmitters in astrocytes [30, 31]. Rather strikingly, the existence of most of the ion channels (and several receptors) that were discovered in neurons, could step by step also be confirmed in astrocytes. The following paragraph introduces briefly the most important types of ion channels in glial cells:

The first biophysical studies on astrocytes, more than 50 years ago, demonstrated that glial cells show a hyperpolarized resting potential (-70 to -90 mV) relative to neurons and a large K^+-permeability [32, 33]. The resulting finding of K^+-channels was therefor rather unsurprising, also because the resting membrane potential, predicted by the Nernst equation, was implicating their presence [34]. The resting membrane potential in astrocytes is primarily established by inward rectifying K^+ (K_{ir}) channels that are open close to the resting potential and closed at more depolarized potentials. These channels are mainly responsible for the whole-cell current profile of astrocytes, displaying larger currents negative of the resting potential and smaller ones at potentials that are more positive. K_{ir} channels have been found to have their conductance blocked by Cs^+ and Ba^{2+} [35, 36]. The inwardly rectifying K^+- channel Kir 4.1 is expressed exclusively in glial cells of the CNS. Other types of K^+-channels that were found to be expressed in astrocytes are outwardly or delayed rectifying K^+ channels (K_d), transient "A"-type channels (K_a) and Ca^{2+}-activated K^+-channels (Ka_{Ca}).

The first demonstration of voltage-activated Na^+-channels with the patch-clamp technique was on cultured rat cerebral astrocytes [37]. In comparison to neurons, Na^+ expression densities are about three-fold smaller in almost all types of glial cells [38, 39]. As astrocytes do not generate action potentials, it was suggested in studies on TTX-sensitive Na^+-channels that they create a "return" pathway for the K^+-Na^+-ATPase, possibly modulating the K^+-reuptake from the extracellular space [34].

All cells express transporters and ion channels to move Cl^-, bicarbonate and other anions across the cell membrane, with Cl^- being the primary negative charge carrier. Also glial cells are no exception to this; still their anion channels are probably their least well studied channels, even though they have been demonstrated in cultured astrocytes. Most is hereby known of volume regulated anion channels (VRACs). These channels have been discussed as release routes for transmitters such as ATP [40, 41].

After the discovery of this broad variety of ion channels expressed in astrocytes, they were regarded as electrically non-excitable cells, carrying out various important duties in the CNS with their primary responsibility on creating and controlling the optimal homeostatic environment for neuronal function. Astrocytes maintain the physiological levels of ions and transmitters in the brain, as well as the pH. [42, 43]. One part of the astrocytic regulation of neurotransmitter levels is the excitatory amino acid glutamate. The astrocytic clearing activity prevents the brain from a toxic accumulation of glutamate. And also the re-uptake and recycling of glutamate to glutamine in astrocytes plays an important role in the normal glutamate supply for the inhibitory and excitatory synapses. Neurons use the "recycled" glutamine provided by astrocytes to again transform it into active glutamate for synaptic transmission [44, 45].

Another major astrocytic duty is the maintenance of the brain's water homeostasis. In particular the astrocytic endfeet express the bidirectional water channel aquaporin-4 (AQP4) that together with K^+-channels enables astrocytes to play a pivotal role in the brain's water homeostasis and spatial buffering of extracellular potassium [46, 47]. These astrocytic terminal processes enwrap the brain capillaries, enabling the control of the cerebral blood flux, regulating vasodilation and vasoconstriction, and induce endothelial cells during development to form tight junctions which create the basis of the blood-brain barrier [48, 49, 50]. As astrocytes are in the favorable position to be in contact with the cerebral blood vessels as well as with neuronal axons and synapses, it is currently discussed that they also play a role in the brain metabolism. In the brain, glycogen is found predominantly in astrocytes and by them broken down to lactate during hypoglycemia and transferred to adjacent neurons. Also during periods of intense neuronal activity, it is astrocytic glycogen that ensures the energy supply and the preservation of neuronal function [51, 52].

Last but not least in this non-exhaustive description of glial duties in the CNS, the astrocytic response to diverse forms of brain injury must be mentioned. Under normal circumstances, the brain is very well protected from the entry of immune cells, plasma proteins and other harming molecules on the basis of polarity and size by the blood-brain barrier. In case of an acute trauma, stroke or other CNS disorders, it is astrocytes that detect and integrate the signals of damage and inflammation and regulate the neuroinflammatory response. Astrocytes respond to brain injury with changes in their gene expression and morphology and by proliferation they form a physical barrier to seal off the injury site, prevent entry of harming molecules and keep the inflammation local. This process is referred to as reactive (astro-)gliosis [53, 54, 55, 56].

But still, for not being able to fire action potentials, astrocytes where thought to be unable to actively participate in brain information processing [31].

CALCIUM SIGNALLING AS A FORM OF CELLULAR EXCITABILITY. In the early 1990s, the view on astrocytes was challenged again with the discovery that local application of glutamate can trigger cytosolic Ca^{2+}-elevations in astrocytes that can propagate as Ca^{2+}-waves to neighboring cells [57]. Astrocytes were then found to react to a variety of external stimuli, such as electrical activity of neurons, neurotransmitters, changes in the osmolarity balance or even mechanical stress with intracellular calcium ($[Ca^{2+}]_i$) elevations [58].

The origin of the Ca^{2+} for these Ca^{2+}-elevations can be either Ca^{2+} entering from the extracellular space or Ca^{2+} depleted from the intracellular stores [59]. A schematic to summarize the various ways of Ca^{2+} entry is shown in figure 4. Experiments on astroglial cells have shown that physiological stimulation triggers the production of inositol 1,4,5-triphosphate (IP_3) via the phospholipase C pathway. Activated by the G-protein coupled metabotropic glutamate (mGLUr) and purinergic (P2Y) receptors, PIP2 is broken down into Diacylglycerol (DAG) and IP_3. IP_3 can either bind on IP3R2 receptors on the endoplasmic reticulum to release calcium or propagate through gap junctions to neighboring cells to induce Ca^{2+}-elevations [60]. On the other hand, a rise in $[Ca^{2+}]_i$ can be produced by an influx of extracellular Ca^{2+} entering the cell through different ionotropic receptors such as the glutamate receptor (iGLUR) or the purinergic receptor P2X7 [61]. Hemichannels, constituted of Connexin 43, are permeable to small physiological molecules like Glutamate and ATP and may also be involved in astrocytic calcium signalling [62]. Moreover, extracellular Ca^{2+} can enter astrocytes through voltage gated calcium channels (VGCC) or by activation of transient receptor potential channels (TRP), a wide family of channels from which several of them were shown to be expressed in astroglia. Among those, for example some isoforms of TRPC channels were described to be stretch-activated channels and linked to store-operated Ca^{2+}-entry. They also mediate large Na^+ fluxes that are associated with the endoplasmatic reticulum Ca^{2+}-release [63].

THE TRPV4 CHANNEL. A member of the vanilloid subfamily of TRP channels (TRPV), namely $TRPV_4$, was discovered to be highly abundant in astrocytic endfeet and described as a non-selective cation channel with a high permeability for Ca^{2+} and a lower one for other monovalent cations [64]. $TRPV_4$ channels were found to be activated by a variety of stimuli, including osmotic changes in the cell environment, mechanical stimulation, changes in temperature, chemicals like phorbol esters (such as 4αPDD [65]) and changes in $[Ca^{2+}]_i$ [66, 67, 68, 69]. $TRPV_4$ mediated currents were found to be blocked by the unspecific blockers Ruthenium Red, Gadolinium chloride and the $TRPV_4$ selective inhibitor RN-1734 [70, 71]. $TRPV_4$ channels have also been associated with regulatory volume decrease (RVD) thereby interacting as an osmosensor with the water channel Aquaporin4 (AQP_4). $TRPV_4$ provides a Ca^{2+}-signal for the activation of potassium and anion channels that leads to an efflux of these osmolytes followed by water [72, 73, 74].

THE TRPA1 CHANNEL. TRPA1 is the only member of the ankyrin subfamily of TRP channels expressed in mammals. It is a cation channel like $TRPV_4$, yet poorly selective to Ca^{2+}. Initially, TRPA1 was described as a mediator of noxious cold stimuli in sensory neurons, because this channel responds to cold. However, this view is currently under debate, because more recent studies were not able to confirm

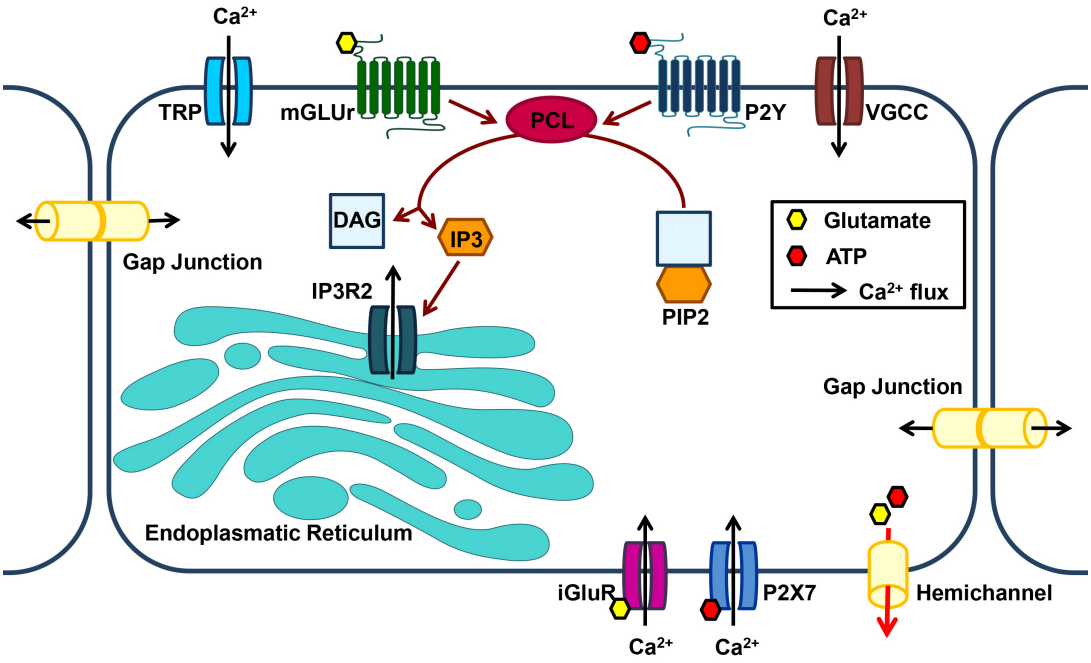

Figure 4: Mechanisms of calcium increases in astrocytes (modified from Agulhon et al. [31])

this cold-sensitivity [75]. In astrocytes, TRPA1 channels were described as regulators of astrocytic basal Ca^{2+}-levels and a blockade was found to reduce long-term potentiation in hippocampal neurons [76]. TRPA1 channels were reported to mediate spatially confined and slow-decaying $[Ca^{2+}]_i$ increases and can be blocked specifically by the TRPA1 antagonist HC-030031 [77, 78]. TRPA1 is embedded into the cell lipid membrane and strongly interacting with it. Therefor an activation by mechanical stimulation is discussed, but also reagents, such as trinitrophenol and lipopolysaccharides that integrate into the membrane are able to indirectly activate TRPA1. TRPA1-channels can also be activated by a rather broad variety of chemical stimuli, such as extracts from mustard and pungent roots, cinnamon, onions and garlic. TRPA1 is also described to be activated by oxidative stress during inflammatory processes, when 4-hydroxy-nonenal and acrolein accumulate during an inflammation [79].

2.2.3 *Astrocytic dysfunction in neurodegeneration.*

Given the fact, that Ca^{2+} acts as an ubiquitous messenger within cells and therefor a tight control over $[Ca^{2+}]_i$ is necessary, it is only plausible to assume that a deregulation of Ca^{2+}-homeostasis leads to cellular malfunction. So it is rather unsurprising that aberrant Ca^{2+}-signaling in astrocytes has been reported to play a role in wide range of neuropathologies, including ischemia, different forms of dementia, but also autism and migraine [80, 42, 81]. But not only aberrant Ca^{2+}-signalling adds a major contribution to brain diseases - any astrocytic malfunction can and often will assist to the formation or onset of an illness. For example the dysfunction of a major astrocytic K^+-channel, namely Kir4.1, has been described in the context of Huntington's disease, where a decrease in functional expression of this channel was attributed to

increased extracellular K^+, which in turn lead to striatal medium spiny neuron dysfunction. The increased firing of these neurons *in vivo* is a characteristic feature of Huntington's disease [82]. A loss of Kir4.1 was also described in Alzheimer's disease and amyotrophic lateral sclerosis [83]. This channel has, among other K^+-channels, also been described in epilepsy, where the occurrence of seizures could be attributed to a disturbed clearance of extracellular K^+ and those abrogated K^+-buffering mechanisms were found to lead to a disturbed re-polarization of neurons [84, 45].

Astrocytes were also found to play a major role in brain edema. The water channel AQP4 expressed (primarily) in their endfeet controls water fluxes into and out of the brain parenchyma, but also contributes to cytotoxic edema following traumatic brain injury. As the brain is encapsulated in the skull, it has only very limited space for volume enlargement, which creates an elevated intracranial pressure that may lead to neuronal death. An increase in AQP4 expression is observed in reactive astrocytes after a traumatic brain injury, enabling such an undue brain swelling. Moreover AQP4 is also dispersed in the cytoplasm in reactive astrocytes. On the other hand, studies demonstrated that mice lacking AQP4 were protected from edema produced by water intoxication, resulting from water uptake due to the traumatic disruption of the blood-brain barrier. In addition to cerebral edema, accumulating evidence suggests that AQP4 participates in the onset and progression of Alzheimer's disease, Parkinson's disease and depression [85, 86, 47, 87]. Moreover, an extreme decrease in the abundance of AQP4 channels in the membranes of hippocampal astrocytes was found in patients with epilepsy [88].

In schizophrenia, post-mortem brains did not show degeneration of neurons but abnormalities in the morphology of astrocytes, together with anomalistic expression of several astrocyte-related genes. Also hypofunction of NMDA receptors as well as aberrant astrocytic glutamate homeostasis have been discussed in order to find explanations for the neurobiology of schizophrenia [89]. As evidence accumulated that in the case of schizophrenia glial cells (instead of neurons) play the leading role and findings of increased microglial densities supporting the hyothesis that proinflammatory cytokines might be relevant in the development of psychosis, also the investigated therapies focus now on astrocytes as potential targets for novel therapeutic agents [90]. Seeing astrocytes as one of the key-players in brain pathophysiology, it has to be underlined that it is high time for this expansion of focus.

2.3 CURRENT TECHNOLOGIES FOR ELECTROPHYSIOLOGICAL RECORDING

2.3.1 *The Patch-Clamp technique*

The physiology of ion channels has always been a main topic of interest in neuroscience research. The patch-clamp technique is currently the gold standard for real-time investigation of ion channel conductance, because it allows the investigation of a small set of ion channels down to single-channel recording. The technique can be applied on single cells in culture as well as on freshly prepared slices of tissue, on cell bodies or on their processes [91]. A scheme representing the equivalent electrical circuit is shown in figure 5. To isolate a membrane patch electrically, a thin glass pipette with a blunt tip is sealed onto the membrane, then mild suction is applied to establish a high-resistance seal in the gigaohm range (*cell-attached configuration*, see 6). Thereby all ions passing through this membrane patch flow into the pipette and can be recorded by a chlorinated silver electrode connected to an electronic amplifier. A grounded bath electrode is used to set the zero level. For many patch-clamp application, the *whole-cell configuration* is the method of choice. By a pulse of suction or voltage, the membrane is ruptured, creating a direct access to the cell interior. In the the *voltage-clamp configuration*, the voltage of the whole cell to be set and controlled, allowing the current response of the cell to be studied. In the the *current-clamp configuration*, a defined current is injected into the cell, while the cellular voltage response is monitored [92, 93, 94].

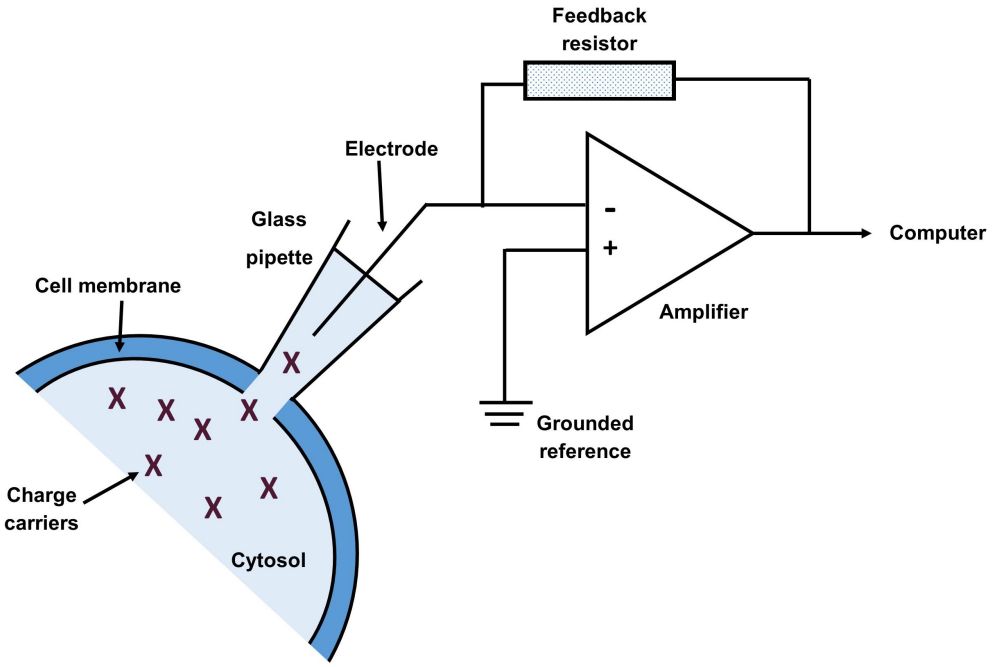

Figure 5: Electrical circuit of a patch-clamp setup. Modified from [95].

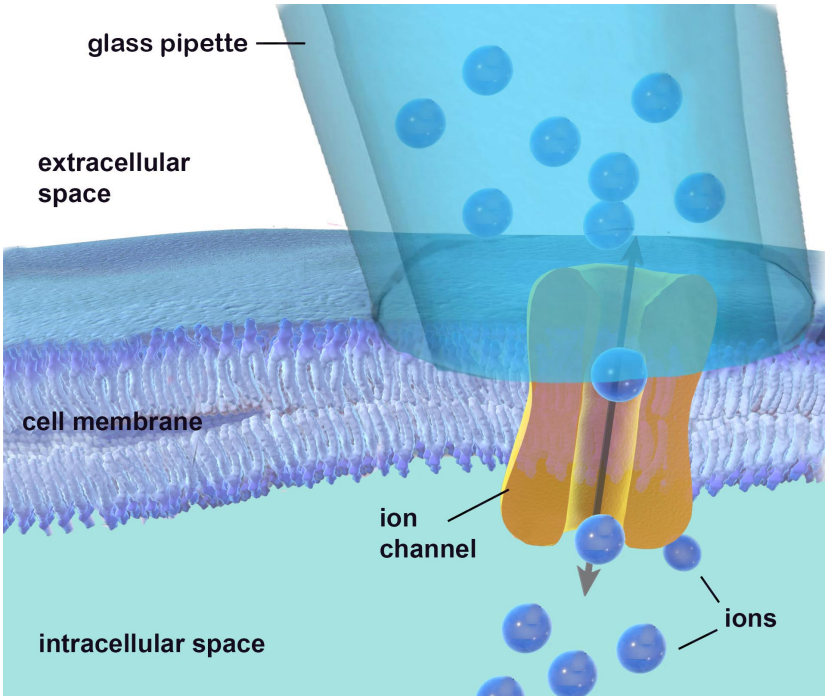

Figure 6: Schematic representation of a cell-attached patch-clamp configuration, where currents through few ion channels of the captured membrane patch can be measured. Rupturing the membrane in this configuration allows to measure currents over the membrane of the entire cell (whole-cell configuration). Modified from [95].

With its unbeaten signal resolution, complex biophysical properties of different ion channels can be studied in depth. Nevertheless the major disadvantage of this technique is its limitation to stimulation and recording of single cells, and therefore neither suitable for high-throughput screening nor for studies on more elaborate neuronal-astrocytic networks.

2.3.2 *Multielectrode Array*

The main methodology so far for extracellular recording, to provide real-time insight into neuronal network activity and deciphering specific neural interactions and circuits, is the use of substrate-integrated multielectrode arrays (MEAs, figure 7A). These two-dimensional arrangements of multiple electrodes are platforms with electrodes and interconnections based on metals and inorganic semi-conducting materials. The high conductivity and high-definition processability with microfabrication technologies, such as vacuum deposition, made these materials so far the materials of choice [96]. Even though MEAs based on flexible substrates have already been realized, most commercially available MEAs remain to be fabricated on glass substrates, due to its transparency and robustness, but also in regard of cost-efficient mass production [97].

The MEA system allows, unlike the patch-clamp technique, the recording with multiple electrodes at a time (in figure 7B, four recording sites of the 64 are shown), rather than recording from single cells. The researcher has also the choice to selectively address different recording sites of one MEA, allowing to set up controls within the same experiment [98]. Moreover, extracellular recording leaves the cell membrane

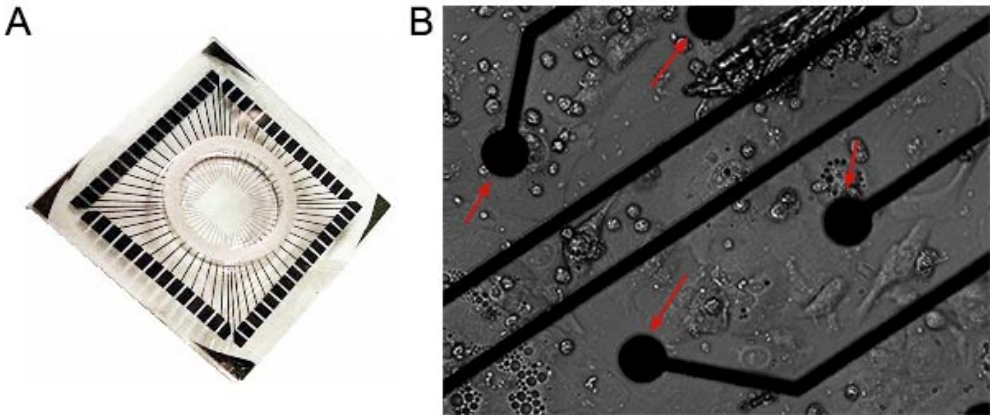

Figure 7: (A) Commercially available MEA used as a reference in our laboratory. (B) Light microscope image of a cardiomyocyte culture (HL-1 cell line, 40x magnification) on the MEA shown in (A). The recording sites are marked by the red arrows. (pictures taken by Saskia Karges)

intact, for as a non-invasive technique, it does not require the breaching of the membrane [99].

Apart from the advantages of the MEA, enabling simultaneous recording of extracellular field potentials generated by action potentials, it still lacks the sensitivity to record also the sub-threshold synaptic potentials and moreover it is not suitable for the recording of electrically passive cells in the nervous system, such as astrocytes [100]. Additionally, their greatest disadvantage comes with their rigidity and mechanical stiffness of the silicon based platforms, making them unsuitable for *in vivo* studies or as implants [14, 96]. Rigid implants tend to damage the surrounding tissue during insertion and impose chronic stress onto the sensitive biological environment due to arising mechanical forces [96, 101]. Injuries in the CNS lead to complex cellular interactions in order to repair the initial tissue damage by triggering a major glial response referred to as *reactive gliosis*. But not only acute injuries are able to cause such an immune reaction, also a lack of biocompatibility of the used material can. In both cases, microphages nest in on the area followed by the recruitment of microglia of the immune system which start to proliferate. Then astrocytes are activated to clear the leftovers which is a fruitless effort in case of an artificial implant, for they are normally built to be resistant to bio-degradation. The result is a "frustrated phagocytosis" leading to a dense glial scar, encapsulating the implant to isolate it from the surrounding delicate tissue within shortest time [101, 102, 103, 104, 105]. This undesired formation of a glial scar changes the electrical coupling of the implant with the surrounding tissue, but may even cause further damage as far as neuronal loss caused by microglia entering in an overactivated state thereby releasing neurotoxic reactive oxygen species. Ideally, an interface should ensure good electrical coupling and while at the same time inducing stable and homogeneous neuronal network formation whereas the formation of glial scar leads to a deterioration and loss of the electrophysiological signal over time [106, 107, 14].

2.3.3 *Calcium Imaging*

Ca^{2+}, as discussed above, is an ubiquitous intracellular messenger and present in many eukaryotic signal-transducing pathways, but also plays a central role in cellular pathophysiology. So it is important to monitor the dynamic changes of Ca^{2+}-levels in living cells with both, spatial and temporal, accuracy. One straight-forward approach is calcium imaging, where changes in the level of intracellular Ca^{2+} ($[Ca^{2+}]_i$) are monitored with the help of Ca^{2+}-indicators and microscopic techniques. Indicators for Ca^{2+}-imaging are often a combination of a calcium chelator and a fluorophore. The binding of Ca^{2+} leads to a change in the emitted fluorescence by changing the intramolecular conformation of the dye [108, 109].

One of the most prominent dyes is Fura-2-AM, a ratiometric Ca^{2+}-indicator (figure 8A). The acetoxymethyl (AM) ester form makes the dye cell permeant and allows the loading of cells in a noninvasive way. Fura-2 emits at a wavelength of 510 nm regardless the presence of Ca^{2+}. The fluorescence intensity shifts when excited from 340 nm to 380 nm upon Ca^{2+}-binding. The ratio of the emissions at these wavelengths is thereby directly related to the amount of intracellular Ca^{2+} [110]. Another type of dyes that is widely used in neuroscience is Fluo-4-AM (figure 8B). It is excited at a wavelength of 488 nm and emits at 516 nm upon Ca^{2+}-binding. It shows no accompanying spectral shift upon Ca^{2+}-binding, whereas the the fluorescence intensity increases about 100 times, providing an optimized signal-to-noise ratio (figure 8C) [29, 111].

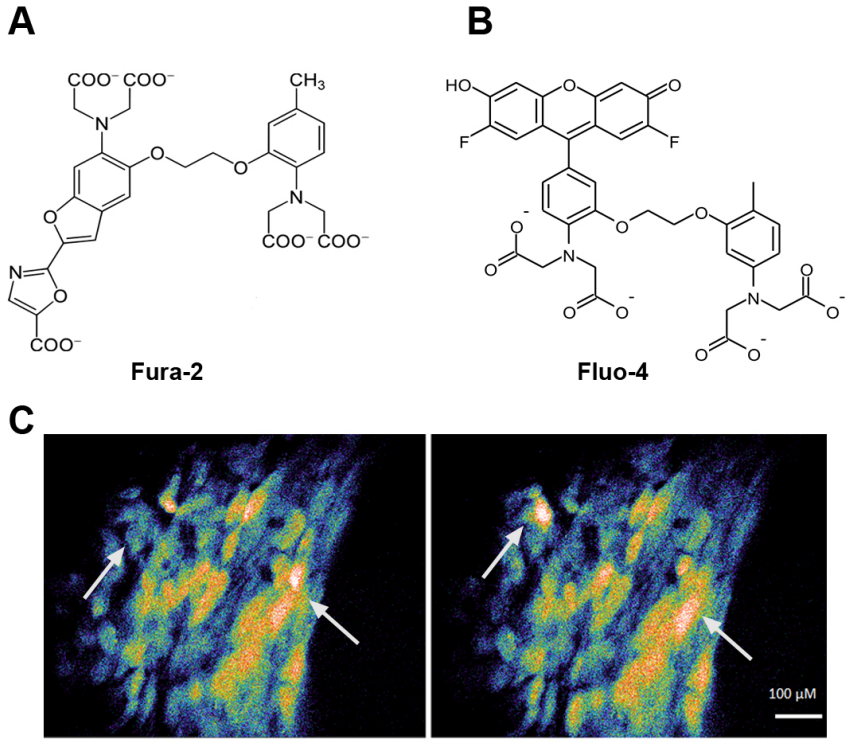

Figure 8: Chemical structure of the Ca^{2+}-indicators (A) Fura-2 [112] and (B) Fluo-4 [113]. (C) False colored fluorescence images of astrocytes loaded with Fluo-4. Arrows indicate prominent changes in intracellular Ca^{2+}-levels during the recording period (blue: basal levels, yellow/red increased levels; pictures taken by Saskia Karges).

2.4 ORGANIC MATERIALS IN FOREFRONT NEURAL INTERFACES

2.4.1 *Properties of organic materials*

Neural interfaces are devices built to exchange information with the nervous system. A variety of (potential) implants are currently used in clinic or under trial in animal models with the goal of improving the quality of life for individuals by restoring their impaired physical, psychological or social functions [101, 114]. Basic neural interface implants already play important medical roles, still research needs to be done to fine-tune for example size, shape, or mechanical properties to enable chronic, stable recordings or (selective) stimulation of neural activity [115].

In order to enable the interfacing of living tissue with any kind of material or device, general criteria regarding the needs of the cells as well as the desired material properties must be met. A summary of these requests is shown in figure 9.

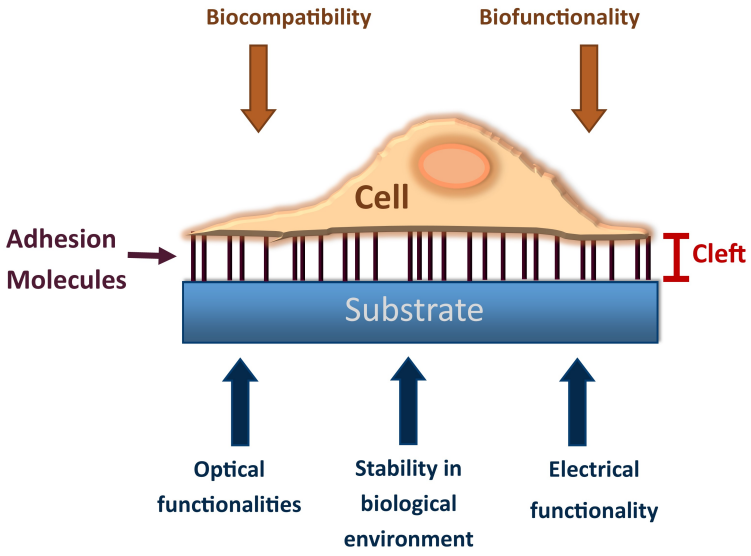

Figure 9: Challenges in developing novel organic neural interface materials. The needs of the living tissue has to be met, therefor the used materials must be biocompatible and biofunctional. The choice of substrate depends on the application and must have the desired optical and electrical functionality but also the stability to perform in the rather harsh biological environment. Most of materials require a treatment with adhesion molecules, causing an increased cleft between the living tissue and the interface. (modified from [116])

To ensure the adhesion and growth of cells, the material must be biocompatible - thereby not having toxic or injurious effects on the living tissue as well as biofunctional, which describes the ability of a device execute its intended function in intimate contact with living tissue [117]. These questions have to be addressed and the reason is straight forward: many materials applied for neural recording and stimulation were not originally developed for neural interfaces. To allow adhesion and growth of cells, materials need to have an homogeneous and unfractured surface combined with an appropriate surface wettability and polarity [116, 118, 117].

As discussed in section 2.3.2, rigidity and mechanical stiffness of implants tend to damage surrounding tissue during insertion and due to arising mechanical forces.

In case of brain implants, the formation of a glial scar has to be avoided at any costs. Traditionally, electronic devices were silicon or metal based, so called 'inorganic' materials that are characterized by a certain stiffness, non-transparency while being at the same time stable and highly conductive. On the other side of the chemical spectrum, the organic materials can be found, a chemical term classically referring to carbon-based compounds [14, 101, 96]. Those organic materials come in a broad range of forms, from crystals all the way to disordered composites, polymers or even gels and many of them have been found to display desired key features such as biodegradability, softness, flexibility and conformability [119, 120]. Organic materials are easily modified in their structure with the almost unlimited possibilities of chemical fine-tuning. By changing for example the side-groups of a molecule, relevant properties such as their topography, biocompatibility or mechanical stiffness can be altered. A very important feature is the relatively low temperature (in comparison to silicon based materials) at which organic materials can be processed - they are often held together by weak molecular interactions which can be easily overcome by mild heating [121]. Another important characteristic is that many organic materials are very colorful, thereby interacting with light, making them interesting for example light emitting diodes or organic solar cells. Other organic materials are transparent or semi-transparent, this being the reason why they are of particular interest for application in tools, where optical read-out techniques such as microscopy are used [122, 123].

2.4.2 *Organic semiconductors*

Apart from the chemical classification in organic or inorganic materials, materials can also be classified according to their conductance: conducing materials, which are often metals and insulating materials. Some of the latter can be made conducting by heating, illumination or enclosure (= doping) of small impurities (= dopants). The resulting conductive materials are called semiconductors [9] and the most famous among them is silicon. A pure silicon crystal is a good insulator, however doping it with small amounts of phosphorus makes it conducting due to the fifth valence electron - which serves as a free charge carrier (figure 10A). Those materials, whose semi-conductance is based on introduced free electrons (negative charges), are called n-type or n-doped. In contrast, using a 3-valent dopant such as boron makes electrons in the valence band of the silicon mobile (figure 10B). These semiconductors are called p-type semiconductors or p-doped, due to the positive 'holes' [124].

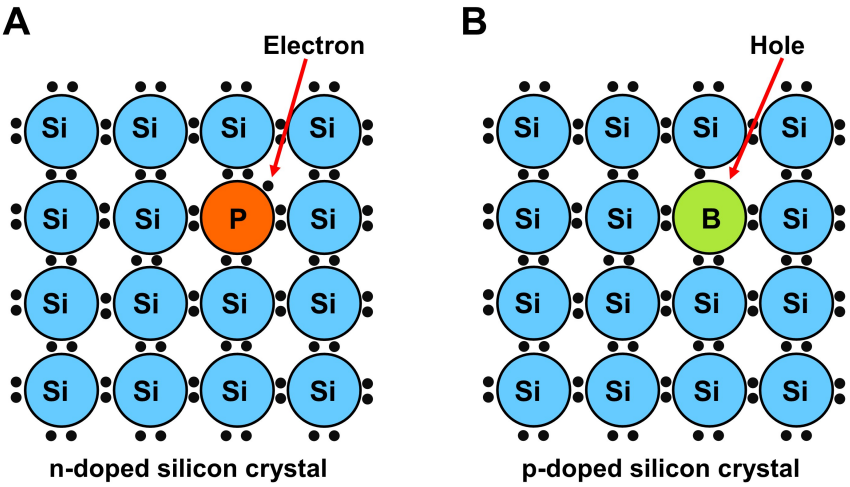

Figure 10: (A) N-type silicon doped with phosphorus. The donor impurity contributes free electrons, increasing the conductivity. (B) P-type silicon doped with boron. The acceptor impurity creates a so called hole. (modified from [125])

Many organic organic compounds can be made semiconducting by doping or are semiconducting by themselves due to their chemical structure. Improvements in carrier mobility can be achieved either by an endless variety through chemical modification towards better characteristics or by creating hybrids of organic and inorganic materials [126, 127]. When building electronic devices with organic semiconductors, only very thin layers of material are needed, making them flexible. Moreover they tend to be rather soft than porous so they are bendable without breaking. This is particularly advantageous when it comes to building interfaces for *in vivo* applications, where it is highly unlikely to find a straight and stark surface. In addition, many of these materials can be produced by standard semiconductor fabrication processes, such as printing, and can be processed at rather low temperatures and without much energy usage [13, 14]. A non-exhaustive list of processing and device fabrication techniques can be found in section 2.5.1.

Taken together, organic materials bear great advantages over inorganic materials. They are extremely versatile and modification with the full toolkit of chemical possibilities offers an unheard possibilities of fine-tuning to create novel materials with application-tailored properties, even though their conductivity is still a weak point. Below, some of the most prominent and promising organic materials are introduced.

2.4.3 *PEDOT:PSS*

Many new daily life applications require flexible electrodes, preferably produced with low-cost approaches. Devices that are supposed to be interfaced with delicate tissue of the human body require conformability and flexibility, also from their electrodes. To date, the material of choice for fabricating transparent electrodes is indium tin oxide (ITO). However this substrate's flexibility decreases with improved conductivity. Doping with silver can circumvent this disadvantage but only at the price of a loss of transparency [128, 129].

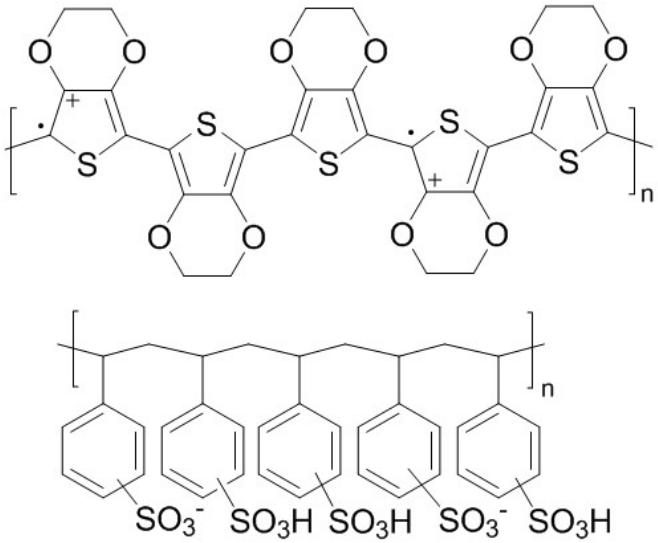

Figure 11: Chemical structure of Poly(3,4-ethylene dioxythiophene) (PEDOT, top) doped with negatively charged poly(styrene sulfonic acid) (PSS, bottom, modified from [125])

Promising candidates for flexible and transparent electrodes were found in conducting polymers, which display apart from their mechanical flexibility also tunable properties via chemical synthesis and superior optical transparency. Among the most used conducting polymers, in particular in bioelectronics, is Poly(3,4-ethylenedioxythiophene) (PEDOT). PEDOT can conduct ions and undergo electrochemical switching. PEDOT itself is a water-insoluble polymer, but by using the water-soluble poly(styrene sulfonic acid) PSS as the charge-balancing dopant, PEDOT:PSS becomes a stable and water soluble polymer mixture (figure 11) [130]. P-doped PEDOT with PSS is well processable and shows an enhanced conductivity up to 10 S cm^{-1}. The conductance can be further increased more than two orders of magnitude by adding secondary dopants to the PEDOT:PSS dispersions, such as different organic compounds like diethylene glycol or dimethyl sulfoxide [131, 132]. The commercially available PEDOT:PSS aqueous dispersion is a deep-blue solution. Films of PEDOT:PSS have a good photo- and electrical-stability in air and can also be heated up to 100°C, without loosing their conductivity. These films are absorbing well in the visible light range, allowing applications in energy conversion and storage devices, organic solar cells, supercapacitors or thermoelectric devices. PEDOT:PSS can be processed by a variety of techniques, from spin-coating to spray deposition up to printing. The resulting continuous thin films on many type of substrates are smooth with a low surface roughness, making them also favorable materials to be interfaced with living tissue [133, 134, 125, 135, 136]. A device using PEDOT:PSS as the semiconducing layer is introduced in section 2.5.4.

2.4.4 *Perylene-derivatives*

Perylene derivatives are molecules based on perylene, which is a poly-cyclic aromatic hydrocarbon with the chemical formula $C_{20}H_{12}$. They belong to a group of so called small organic molecules which display interesting alterable physical, optical and electrical properties. Perylene derivatives, often red, violet or black shaded, have

been used as pigments and dyes for textiles [137]. They are chemically, thermally and photo-chemically stable. They have been used in organic solar cells mainly as electron acceptor materials, because they absorb optically in the visible to near-infrared spectrum, which allows a good "harvesting" of sunlight [138].

Perylene Tetracarboxylic Diimide derivatives belong to the most promising small molecules to fabricate n-channel organic thin film transistors (OTFTs) [139]. These particular perylene derivatives display uncommon n-type transport characteristics due to their strong electron affinity of the imide-groups, a large overlap of the π-electron system, favored by the molecule's planarity and the presence of the alkyl-chains, which enhance the overlap between the molecular orbitals of neighboring molecules. These three factors taken together assume responsibility for field effect charge transport and the optical properties [14, 13].

P13 - AN N-TYPE SEMICONDUCTING PERYLENE DERIVATIVE In particular N,No -ditridecyl perylene-3,4,9,10 tetracarboxylic diimide (P13) [140] was found to be one of the most favorable candidates of n-type perylene based semiconductors in biological applications. It's specific chemical structure is displayed in figure 15. In addition to its electronic properties, another advantage of P13 is its transparency. The hydrophobicity of P13 can be seen as a disadvantage in interfacing this material with living tissue, for it has a contact angle of 97.9 $\pm$ 1.6°, which is rather high in comparison with PDL- and Laminin-coated glass (53.4 $\pm$ 2.5°) [14].

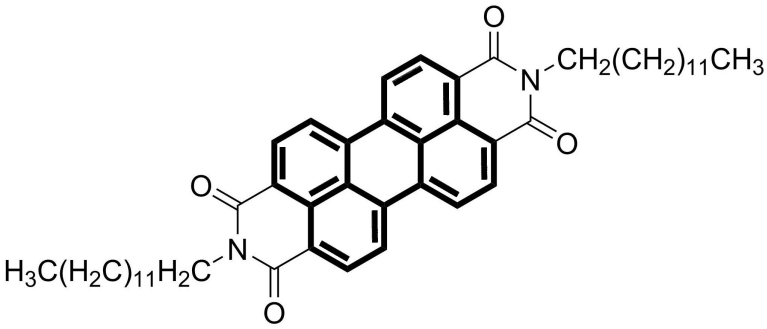

Figure 12: Chemical structure of N,N'-Ditridecylperylene-3,4,9,10-tetracarboxylic diimide (P13, modified from [140]) Marked in bold is the perylene backbone of the molecule.

In a study of our group, P13 thin films have been shown to be stable upon exposure to cell-culture media without significant changes in their morphological, structural and photophysical features. The same study showed that primary sensory DRG neurons from post-natal rats remained viable for many days on PDL-laminin coated P13. Those cells showed neurite outgrowth and their excitability properties resembled those of neurons grown on control PDL-laminin coated glass [14].

2.4.5 *Thiophenes*

Thiophenes are a class of molecules, based on thiophene, also commonly called thiofuran, which is an aromatic flat heterocycle with the formula C_4H_4S (figure 13A). Thiophenes linked with each other to form a polymer are called oligo- and polythiophenes (figure 13B).

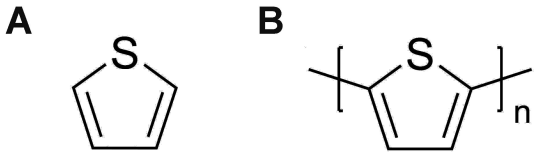

Figure 13: (A) Chemical structure of thiophene. (B) Chemical structure of polythiophene.

From the chemical point of view, thiophenes are stable, easy to process and predestined for modification: at the sulfur atom or at the carbon-ring, a broad range of functionalizations are possible, allowing an extreme fine-tuning of the desired properties. Upon partial oxidation, polythiophenes become electrically (semi-) conductive, making them attractive for integration in electronic devices [141, 142, 143].

Some thiophene oligomers show interesting fluorescence properties, making them valuable materials as active components for applications in light-emitting diodes (LEDs). By attaching different functional side chain substituents bright stable light emission ranging from blue to near-infrared have been realized [144].

Another important field is the integration of oligo- and polythiophenes in optical sensors. One possible application is the detection of various biomolecules such as DNA, RNA, ions or proteins and is also useful in the high-throughput screening of new drugs. Moreover the detection of specific DNA-sequences is crucial for genetic analysis to diagnose various genetic diseases. Novel tools are urgently needed here to skip chemical amplification steps, such as the polymerase chain reaction, for a more rapid assessment [145, 146].

In highly specific DNA-sensors, polythiophenes play already an important role. Such a system consists of two components: a fluorophore labeled single-stranded oligonucleotide capture probe and a cationic polythiophene. The latter serves as a donor for fluorescent energy-transfer, causing a desired signal amplification. The detection mechanism is based on the conformational change of the polythiophene, when interacting with single- or double stranded DNA [147]. A buffered solution with the pure polymer may appear yellow, when interacting with single-stranded DNA red (forming a duplex) and return to yellow, when the single-stranded DNA hybridizes to double-stranded DNA when the complementary strand of the capture probe is added (formation of a triplex). Each change in the thiophene conformation is accompanied by a shift in the absorption spectrum. In case of mismatches of the complementary strand with the capture probe, the absorption will differ from a perfect match [148, 149].

P3HT-PCBM One well-studied thiophene blend is P3HT:PCBM, consisting of the conducting polythiophene poly(3-hexylthiophene) (P3HT) and the fullerene derivative [6,6]-phenyl C61-butyric acid methylester (PCBM, figure 14A).

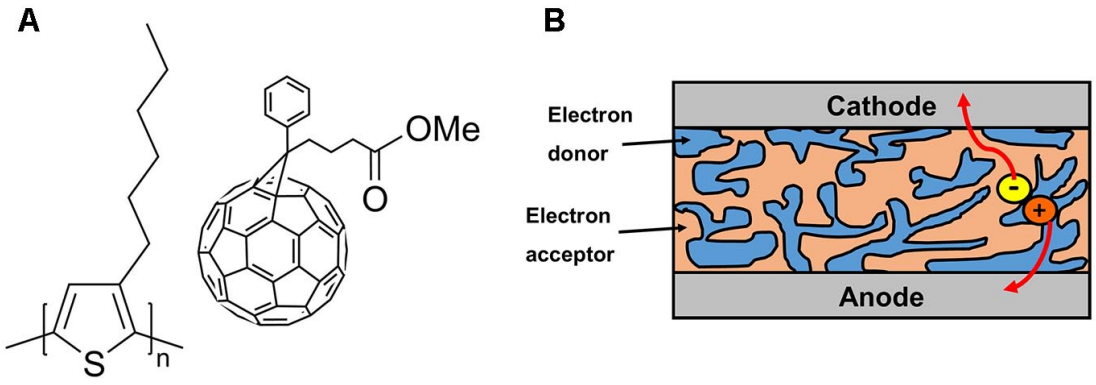

Figure 14: (A) Chemical structure of the P3HT:PCBM blend. Left: poly(3-hexylthiophene) (P3HT), right: [6,6]-phenyl C61-butyric acid methylester (PCBM). (B) Schematic representation of charge separation in a bulk heterojunction device. The created free charges flow through the layer where they are created in to the respective electrode (modified from [150]).

It has to be highlighted that such a blend isn't a homogeneous mixture of two materials, but a so called bulk heterojunction, where the two materials with different electrical properties are forming microdomains in the order of nanometers (figure 14B). This is creating a large interfacial area [151, 152].

P3HT:PCBM, because of its good light absorption, is widely used in organic solar cells, whose function is based on an electron donor-acceptor mechanism. In case of P3HT:PCBM, P3HT is more electron rich and serves as the electron donor, while PCBM plays the role of the electron acceptor. When now exciting the blend with light, light is absorbed and excitons (bound electron-hole pairs), which are split into free charge carriers at the donor/aceptor interface, are created. The donor thereby becomes negatively, the acceptor positively charged. The resulting electron is transported through the acceptor layer towards the electrode. The probability of charge separation is maximized by the blend's large interfacial area while at the same time the recombination process is limited [153, 154]. P3HT based solar cells have a power conversion efficiency exceeding 3-5%, the focus in the organic solar cell research lies on increasing this efficiency, mostly by doping one of the organic components or by changes in the fabrication process, e.g the annealing temperature [126].

Another application, where a broad absorption in the solar spectrum is highly desirable, are retinal prosthetic devices. The idea behind is to couple electronic sensors for example with neuronal tissue to translate information carried by light into electrical activity and communicate this information to neurons. P3HT:PCBM was found to be a promising material, not only for its optical and electrical properties, but also for its biocompatibility and "soft" organic nature to create flexible interfaces. A very particular hybrid organic device with P3HT:PCBM as semiconducting layer, realized by Ghezzi *et al.* is described in section 2.5.5 [152, 155].

2.4.6 *Biomodified organic materials*

To date, most approaches interfacing organic semiconducting materials or devices with neural cells still required a treatment of the material's surface with cell adhesive

proteins from the extracellular matrix (such as poly-lysine, fibronectin, collagen or laminin). However, the use of these proteins bears some disadvantages. On one hand it has been discussed that surface coating, by increasing the cleft at the interface of cell and transistor, could cause a decrease in the recording sensibility of the respective organic devices (see figure 9) [118, 156, 10, 100]. Moreover, protein degradation over time due to cellular proteolytic activity is a crucial issue, making a long-time application *in vivo* impossible. Another non-trivial step is the isolation of these proteins from other organisms and their purification, which an can lead to infections, immune responses and, in case of brain implants, to gliosis [105].

In neuronal tissue culture, poly-L-Lysine is one of the most commonly used substrates. It enhances cell attachment to various substrates by means of its positive charge that interacts with the anionic sites of the plasma membrane [157].

T4LYSINE Oligothiophenes based on quaterthiophene (T4) have already been used as functional semiconducting material for the realization of organic devices, mainly for their high carrier mobilities and well defined length [158]. The chemistry behind has been well established over the past years [159]. But casted T4 alone doesn't meet the requirements for cell adhesion, because it forms large rhomboidal crystals instead of films and is thereby due to its roughness not suitable to be interfaced with cells [118]. To combine the optical and electronic features of T4 with the established cell adhesion and growth functionalities of Poly-L-Lysine, T4 was covalently functionalized to the L-Lysine-ended quarterthiophene T4Lys to become the first of biomodified organic materials [160].

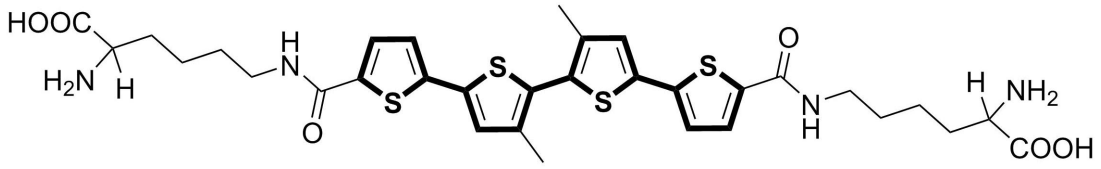

Figure 15: Chemical structure of T4Lysine (T4Lys, modified from [160]) Marked in bold is the tetratiophene (T4) backbone of the molecule.

The results of the biocompatibility study and the electrophysiological characterization of DRG neurons interfaced with T4Lysine are described in chapter 4 of this thesis.

PDI-LYS As described above, the perylene diimide derivative P13 has already been successfully tested as a platform for DRG neurons, even though its hydrophobicity is a disadvantage in terms of cell adhesion. In order to create a suitable interface, the material had to be coated with PDL to circumvent this issue. With the realization of T4Lysine, where lysine was directly integrated into the organic molecule, the additional coating step could be skipped. The same strategy was used to create a perylene diimide derivative bearing lysine groups to combine the properties of lysine to support neuronal adhesion, growth and differentiation with the n-type semiconducting properties of perylene diimide.

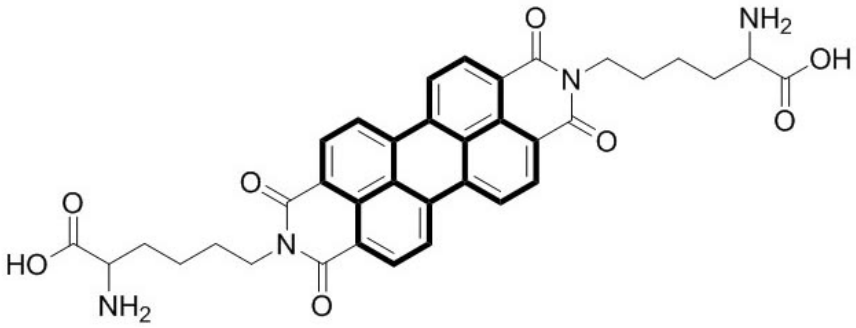

Figure 16: Chemical structure of PDILys (T4Lys, modified from []) Marked in bold is the perylene backbone of the molecule.

It was shown that the lysine-functionalization decreased the high hydrophobicity found in P13 thin- films. In turn also an improved cell adhesion was found with PDI-Lys which is also supporting DRG neuron differentiation. the higher neurite length on PDI-Lys was attributed to the soft nature of this novel organic material, the enhanced *in vitro* biocompatibility to the introduction of lysine [161].

These two example of lysine-functionalized organic materials are promising milestones on the way of finding suitable materials for bio-electronics targeted to neural engineering applications, while skipping the additional coating steps by tailored chemical synthesis.

2.5 ORGANIC BIOELECTRONIC DEVICES FOR ELECTROPHYSIOLOGICAL APPLICATION

Organic electronics is a relatively young scientific field that developed over the past two decades. This technology, even though the realized devices are still inferior in terms of performance, aims to replace the classic inorganic semiconductor devices.

The reason are the advantageous properties such as their lower price (they are much cheaper than silicon), flexibility and transparency. They play already a role in solar cells and organic photovoltaics, being again much cheaper than their silicon-based counterparts. Also organic light-emitting devices and field-effect transistors are already well-developed and partly already commercialized [162, 163].

2.5.1 *Device fabrication techniques*

One of the advantages that comes with the use of organic materials is the variety of device fabrication methods that may be used, whereas inorganic materials are limited to just a few. This section is intended to give a brief overview of some of the currently most used fabrication techniques.

Physical vapor deposition (PVD) PVD is the term to describe a variety of vacuum deposition methods which can be used to produce thin films. For PVD, the substrate to be coated is placed inside a vacuum chamber where it is exposed to precursors that are vaporized by physical techniques (such as heating or sputtering). This vapor begins to condense onto the substrate material and form a uniform layer.

By adjusting the temperature and duration of the process the thickness of the coating can be controlled. For polymer deposition, the monomers are introduced into the chamber, where they react with each other when depositing onto the substrate surface. For metallic compounds, the heated vapor is condensed onto a cooler substrate surface [164].

Chemical vapor deposition (CVD) Just like PVD, in typical CVD, a substrate is exposed to volatile precursors. In principle, a heated substrate surface is exposed to the vaporized coating material. By chemical reactions occurring on the hot surface, a solid component is deposited as a thin film from the gas phase onto the substrate [165].

Spray deposition For spray deposition, molten metal is gas atomized and the spray is caused to hit the substrate while being still in the liquid or semi-solid state and a layer of dense solid metal of a predefined shape is sublimed [166].

These traditional methods, also used to process inorganic materials, generally require a high vacuum and high temperatures, consuming thereby a lot of energy which makes them costly. With organic materials, solution-based preparation methods come into play, which are carried out at room temperature or moderate temperatures and atmospheric pressure. By the choice of the fabrication technique, some of the properties of organic materials may also become tune-able. For example to optimize the charge carrier movement of organic materials, their morphology can be adapted by the use of different solvents. A solvent with a higher boiling point may lead to more crystalline structures, for it needs more time to evaporate [167, 121]. Following is a non-exhaustive list of commonly used fabrication techniques for organic materials.

Etching methods Etching is used to remove layers selectively from a substrate surface in order to create patterns. Before etching the pattern is defined by an etching mask to protect the parts of the material, which should remain. Dry etching with plasma is used for circuit-defining steps, while chemical (=wet) etching is used to clean substrates. Plasma etching is one of the most used processes in semiconductor manufacturing [168].

Spin-coating Spin coating is used to deposit uniform films onto flat substrates. Therefor a small amount of material dissolved in a volatile solvent is applied to the center of the substrate. Then the substrate is rotated at high speed and the majority of the deposited is flung off the side by centrifugal force, leaving the substrate with a highly uniform film from a few nanometers to a few microns in thickness. The advantage of spin coating is its ability to produce very uniform films in short time [169].

Inkjet printing The same technology that is used in customary office printers can be used to print soluble polymers or nanoparticles on a broad variety of substrates, ranging from glass to paper [170].

Screen Printing A method of choice to fabricate conductive connections between electronic components. First a print pattern is created on a mesh surface. This screen mask is placed on top of an alumina substrate, a paste or ink is then applied on top of the screen and then the paste scraped over the mask by a squeegee, transferring the pattern onto the substrate [171].

2.5.2 *OFETs and the O-CST*

Transistors in general are the fundamental element in modern circuitry; they are used as either signal amplifiers or on/off switches. An organic field effect transistor (OFET) consists of a sandwich-like structure of gate, dielectric, the organic semiconducting layers and two metal contacts (source and drain electrode) that are electrically connected to the semiconductor. OFETs can be fabricated in different configurations as shown in figure 17.

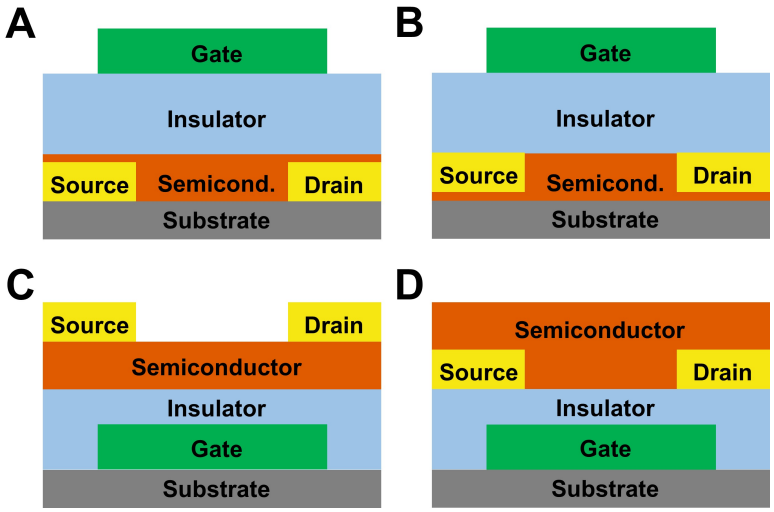

Figure 17: OFETS can be fabricated in different configurations. (A) Top-gate, bottom contact, (B) top-gate, top-contact, (C) bottom-gate, top-contact and (D) bottom-gate, bottom-contact (modified from [172]).

When a voltage is applied between the source and the gate electrodes, an electric field normal to the device surface will build up in the semiconductor, attracting charge carriers at the semiconductor-insulator interface (figure 18B). Operating an OFET in this way is called accumulation mode. When additionally applying a positive voltage between the source and drain electrode, a negative current flows across the channel area from the drain to the source as displayed in figure 18C. In case of a negative applied voltage, holes will flow from the source to the drain electrode, establishing a current through the semiconducting film (I_{SD}). This current can be modified by varying the applied voltages V_{GS} and V_{DS} [173, 172, 167].

An OFET can be used as a sensor for voltage changes on top of its channel, therefor it is also "able to sense" e.g action potentials of neurons by the change of the ion flux at the interface. This cellular electrical activity changes the electric field of the transistor and by these means its output current [121].

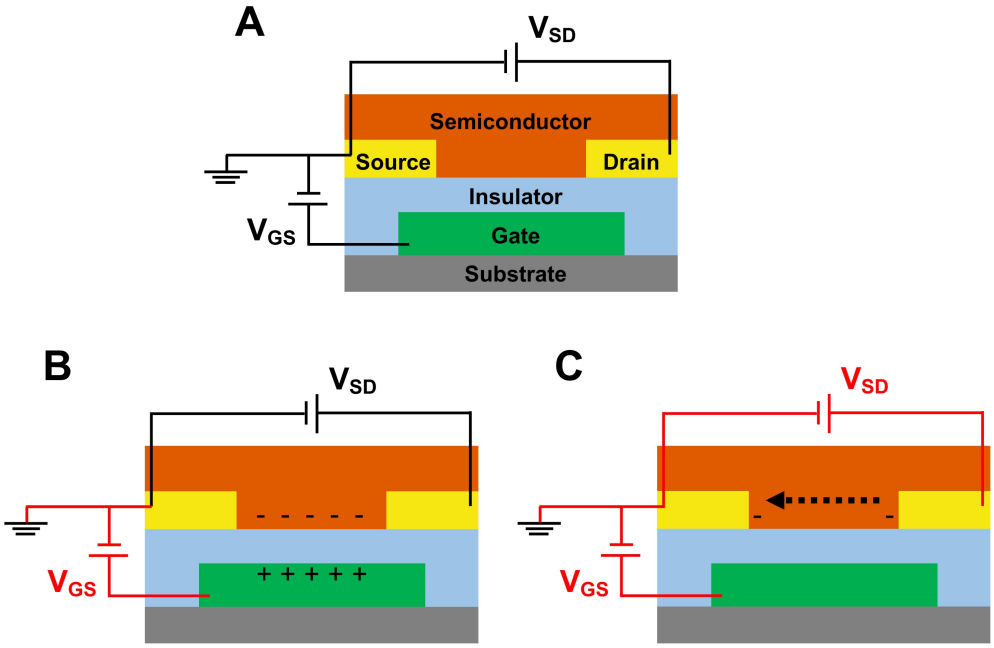

Figure 18: (A) OFET in bottom-gate, top-contact configuration without any voltages applied (black wires). (B) A voltage is applied between the gate and the source (V_{GS}) electrode (red wires). A charge separation is taking place at the interfaces and an electrical field is building up (accumulation mode). (C) An additional positive voltage is applied between source and drain (V_{DS}), resulting in a flux of negative charges from drain to source (black dotted arrow). (modified from [167]).

AN OFET AS CELL STIMULATING AND SENSING DEVICE The OFET (hereafter referred to as O-CST, see figure 19) used in this work was first introduced in a study carried out by my group in 2013, when DRG neurons were interfaced, stimulated and their response recorded with this O-CST [13]. DRG neurons were chosen for this study, because they are known to be almost electrically silent [174], which makes stimulation-evoked activity distinguishable from the occasional spontaneous firing. The O-CST device has a glass substrate coated with Indium Tin Oxide (ITO), double serving as a bottom gate electrode and mechanical support. As a transparent dielectric polymethylmethacrylat (PMMA) was used and P13 (as introduced in section 2.4.4) serves as the n-type semiconducting material. The source and drain electrodes are made of gold and are covered by an additional capping layer of P13 that acts as an insulator to avoid direct contact between the tissue culture medium and the electrodes. The distance between the two electrodes (=channel width) is 70 µm. To prevent also the evolvement of Faradaic currents in contact with tissue culture medium, the maximal voltage applied on the device in biological studies is 1 V [13]. In a first step of the study the P13, the material of the capping layer, coated with PDL and Laminin was found to allow adhesion and growth of primary DRG neurons (see figure 20A) and the presence of neurons was confirmed by staining for neuronal nuclear protein (NeuN) and growth-associated protein 43 (GAP-43), a neurite outgrowth marker (figure 20B and C respectively).

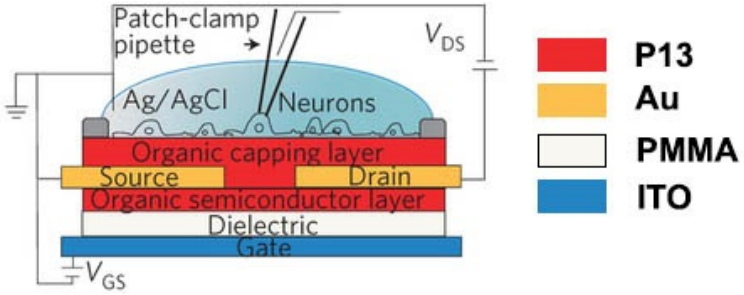

Figure 19: Schematic representation of the O-CST with a P13 capping and semiconducting layer (red), source and drain electrodes made of gold (Au, yellow), the dialectric made of PMMA (grey) and the ITO gate electrode (blue). The whole device is build up on a glass substrate (reprinted with permission from [13], Copyright 2016, Nature Publishing Group).

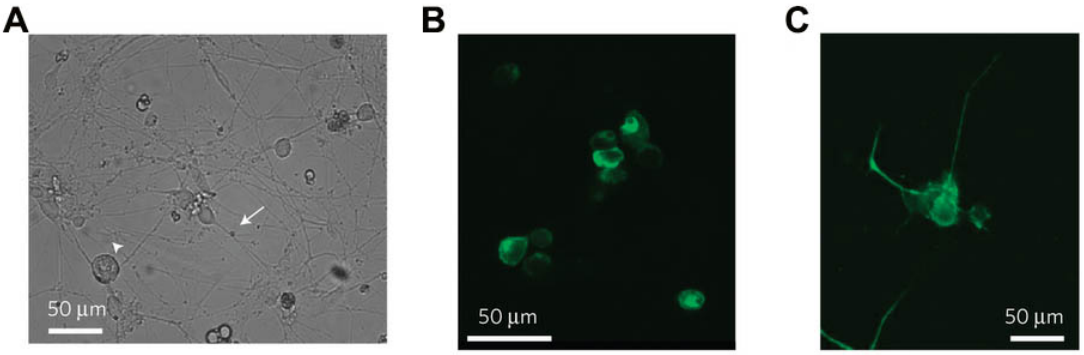

Figure 20: (A) Micrograph of DRG cultures on P13 thin films after 7 days in vitro. The arrowhead indicates a neuronal cell body, the arrow depicts neurite extension. (B) LSCM image of P13-plated DRG cells, stained for NeuN. (C) LSCM image of P13-plated DRG cells, stained for and GAP43 (reprinted with permission from [13], Copyright 2016, Nature Publishing Group).

The researchers then performed a computational study about the electric fields and electrostatic potentials when applying voltages to the electrodes to have a first guess about the effect on DRG neurons. Also field effect transistors like the O-CST can be operated in accumulation mode with the source grounded. When applying a small positive voltage (1V) at the gate electrode (V_{GS}), the capacitor is charged at the dielectric-semiconductor interface and an electric field is built up. Computational simulations showed that the electrostatic potential is null above the electrodes and about 0.7 V in the region above the channel (see Fig.21A). This value was assumed to be sufficient to evoke a capacitative depolarization of neuronal cells, because it is able to induce a relatively large potential in a localized region of space. A regular increase of V_{GS} over time is thus potentially able to realize a steady variation of the potential at the organic-solution interface from 0 to about 0.7 V.

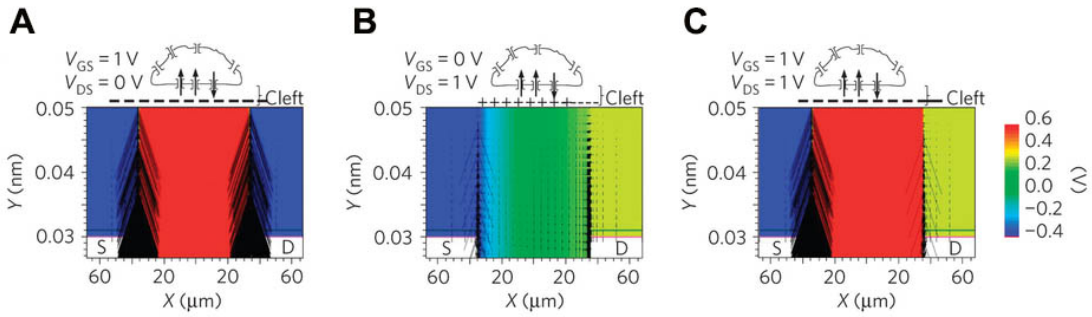

Figure 21: 2D simulation plots of the electric field (vectors) and electrostatic potential (color scale) in the capping layer of the O-CST for different biases. (Reprinted with permission from [13], Copyright 2016, Nature Publishing Group).

When V_{DS}=1V and V_{GS}=0V (see figure 21B) the intensity of the electric field was predicted as not constant along the channel length, resulting in a less intense field. Cells on top of the channel were expected to be exposed to a varying charge distribution along the channel, with an excess of positive charges in correspondence to the cleft - promoting a hyperpolarization of the neuronal membrane voltage.

When additionally applying a source-drain voltage (V_{GS}=1V, V_{DS}=1), the electric field distribution remains asymmetric, with an induced almost constant and positive electrostatic potential at the capping layer interface (figure 21C). Here an induced depolarization of the cell membrane was expected due to a negative ionic charge layer in the cleft between the cell membrane and the device surface.

The group of Valentina Benfenati performed also experiments to study the simultaneous recording and stimulation from O-CST. To this end, they first performed experiments stimulating with the O-CST applying the stimulation protocols described above, while recording the cellular response by performing whole-cell patch-clamp in current-clamp mode (figure 22). When giving a pulsed stimulation after a control recording period, they were able to detect spikes resembling action potentials, when the O-CST bias was around 800 mV (figure 22A). When using a constant V_{DS} of 1V and biasing the gate with a ramp from 0-1V, they observed a hyperpolarization of the membrane potential (as expected from the computational simulation) followed eventually by an action potential (figure 22B). By evoking action potentials by the means of a current-step stimulation protocol applied to the cell via patch-clamp, the possible use of the O-CST as a sensor was tested. They correlated the given stimulation and the so evoked action potentials with the extracellular recording by the O-CST. Even though the recorded signal was rather weak and noisy, they could demonstrate the O-CSTs ability to record from a single neuron (figure 22C-E). To compare the obtained results directly with the technology currently available on the market, the researchers coupled the output of the O-CST drain electrode with the amplifier and recording electronics of a MEA System (figure 23, see also section 2.3.2). They found that the O-CST device had an improved signal-to-noise ratio with respect to the MEA system by a factor of 16 on the same neuronal preparation. The attributed this to the efficient coupling between the organic semiconductor and the cells.

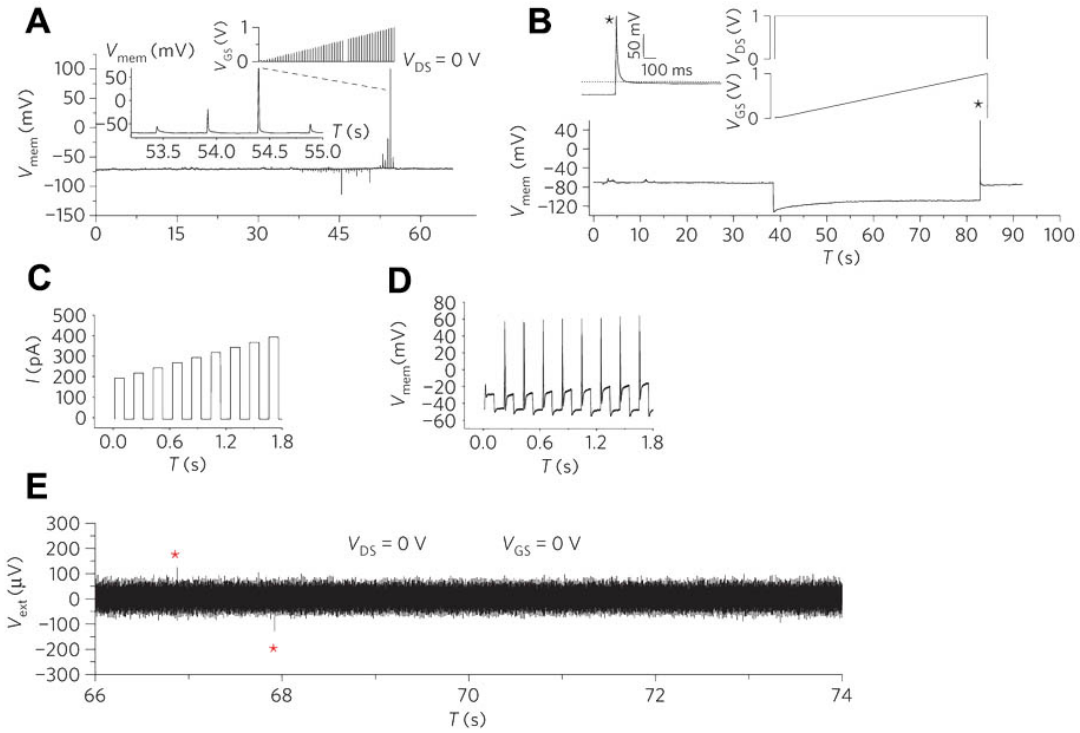

Figure 22: Patch-clamp experiments performed on DRG neurons seeded on the channel of the O-CST. (A) Current-clamp trace recorded before and during pulsed O-CST stimulation (protocol see upper inset). The dashed line indicates a zoom-in to highlight the action potential profile. (B) Current-clamp trace recorded upon continuous ramp stimulation by the O-CST (protocol see upper inset). A zoom-in (*) highlights the action potential profile. (C) Patch-clamp stimulation protocol consisting of a family of increasing current steps of 25 pA from 200 to 400 pA for 100 ms. (D) Patch-clamp trace recorded with the stimulation protocol of (C). (E) The evoked action potentials by stimulation with current steps in (D) were simultaneously recorded by the O-CST. Red stars indicate the detected spikes by off-line data analysis with custom software (reprinted with permission from [13], Copyright 2016, Nature Publishing Group).

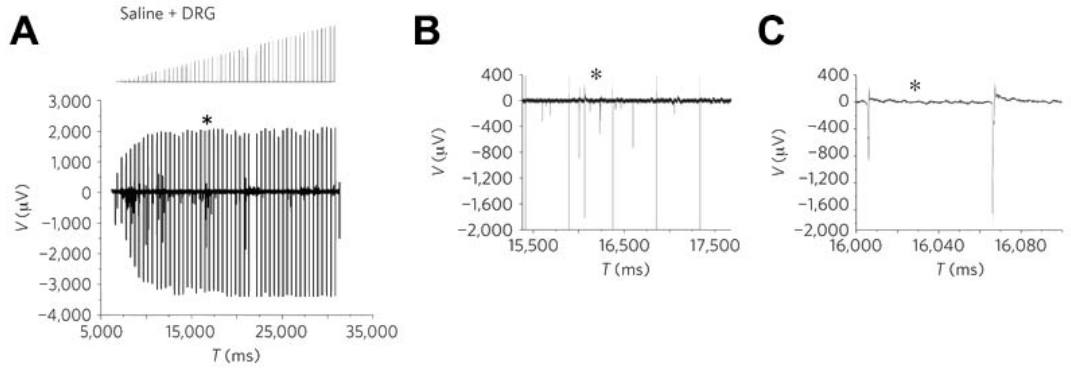

Figure 23: (A) Extracellular signals recorded by the O-CST upon applying a bias to the device with a pulsed stimulation protocol as depicted by the inset (V_{DS}=0V, V_{GS}=0-1V). (B-C) Respective zoom-ins highlighted by the asterisk in (A) and (B) respectively (reprinted with permission from [13], Copyright 2016, Nature Publishing Group).

2.5.3 *EGOFETs*

An electrolyte-gated organic field effect transistor (EGOFET) device is is a three-terminal field-effect transistor (FET) device comprising gate, source, and drain electrodes. The source and drain electrodes are separated by a region called the channel, which is build up by an organic semiconducting layer deposited between them. The difference between an EGOFET and a conventional OFET is the use of an electrolyte as gate insulator instead of a dielectric layer [175]. When applying a bias between the gate electrode and the grounded source, confined electric double layers are formed at the interface between the semiconductor and the electrolyte and the electrolyte and the gate. This process reaches a steady state, where the driving force for ion migration in the electrolyte layer is eliminated. The equivalent circuit of an EGOFET can be modeled as two capacitors in series, representing the two electric double layer interfaces.

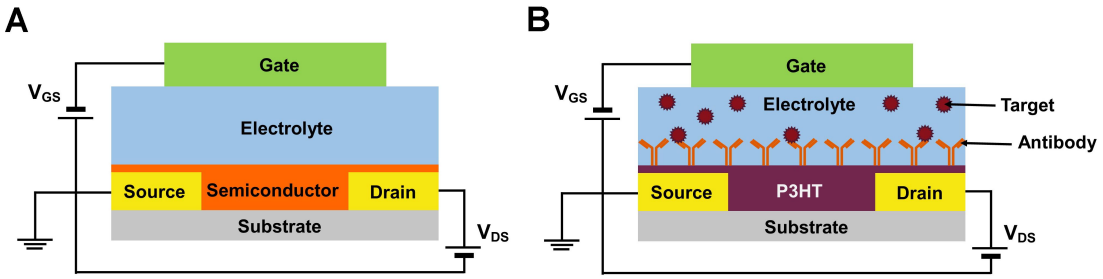

Figure 24: (A) Schematic representation of EGOFET (modified from [176]) (B) EGOFET with a modified organic semiconductor (here P3HT) to serve as a biosensor. A monoclonal antibody layer is physisorbed on the organic semiconducting layer, in presence of the antibody's target analyte an electrical response can be measured (modified from [177]).

An EGOFET can be transformed into a bio-sensor when anchoring recognition tools, such as antibodies or enzymes, onto one of these interfaces. This additional layer can be seen as an additional capacitor in the system. The capacitor of the biological layer is smaller than the other two and thereby highly sensitive to detecting changes in the bio-layer upon for example binding of a ligand (e.g the respective substrate of an enzyme or the specific target to the antibody). Due to this sensitivity and the possibility to detect both, charged and neutral ligands, EGOFETs are among the most promising devices for electronic biosensing applications [163].

In 2013, Cramer *et al.* introduced a liquid gated transistor as an interface for the recording and stimulation of neuronal cells (figure 25A) [178]. The semiconducting layer in this EGOEFT consisted of a pentacene film with a terraced morphology which was found to be biocompatible with murine neural stem cells for up to two weeks. By fine-tuning of the pentacene film properties, they were able to improve cell adhesion without adding an additional coating layer of extracellular matrix proteins. By these means, the group was able to reduce the cleft between the cells seeded on top and the actual device, expecting the capacitive coupling between the semiconductor and cells to be maximal due to direct contact. Murine neural stem cells on top of functional device were then differentiated into neuronal networks and during the different phases of neuronal differentiation, the OFET response was monitored (figure

25B). To this aim, a possible response of the neuronal population on the device was triggered by a voltage stimulus applied through the gate electrode (figure 25C). Only after the differentiation of the stem cells into interconnected neurons, they were able to measure electrical signals in the OFET current where the liquid-gated pentacene transistor transduced the electrostatic potential at the interface between the channel and the electrolyte.

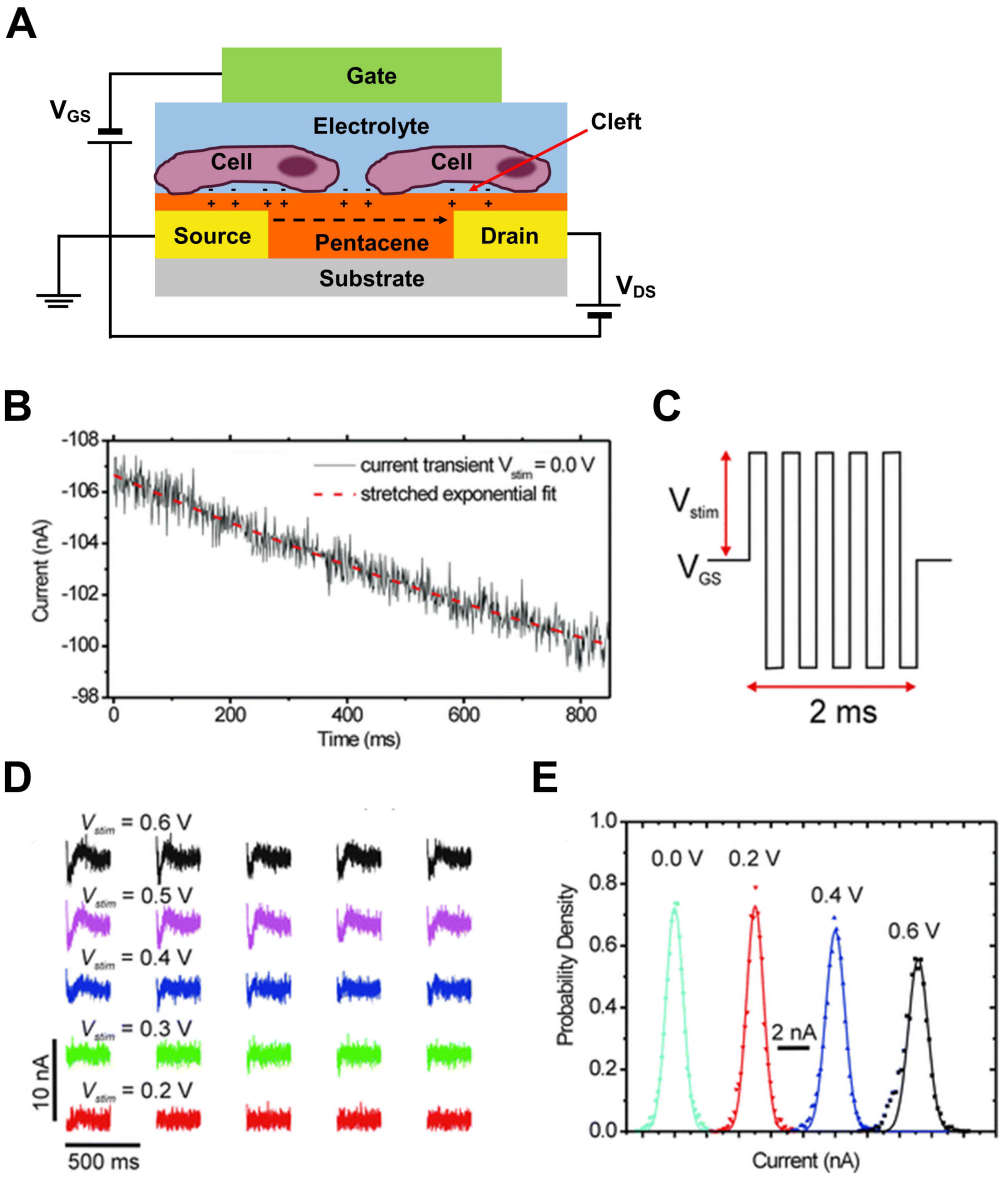

Figure 25: (A) Schematic representation of the liquid gated transistor. The dashed arrow indicated the current from the source to the drain electrode, which results from the average change in the potential at the cleft caused by the cell activity (modified from [178]). (B) Raw data trace showing the I_{DS} current drift and the stretched exponential fit (dashed line). (C) Stimulation pulse shape applied to the potential between the source and the gate electrode. (D) Absolute current traces measured after stimulation with different intensity. (E) Histogram of the current noise with their Gaussian fit (continuous lines) after stimulation. (reprinted with permission from [178], Copyright 2016, Royal Society of Chemistry).

In their study, the authors highlight that their device has a rather large area (0.2 mm^2) averaging the response of several hundred or thousand cells forming a neuronal network. Therefor its working principle cannot be seen as suitable for the detection of action potentials, or even the recording of single cells. Another disadvantage can be seen in the short durability of the device, which could operate with good response in tissue culture medium for up to nine days. A long term electrophysiological application is therefor excluded with this device's setup.

2.5.4 *OECTs*

Organic electrochemical transistors (OECTs) are three terminal devices in which the source and the drain electrodes are connected by a conducting polymer. The gate electrode is separated by an electrolyte from this polymer layer. The operation of an OECT is based on the doping and de-doping of the conducting polymer, which modifies the polymer's conductivity. Nowadays the most used conducting polymer is PEDOT:PSS (see also section 2.4.3). When no gate-voltage is applied, this polymer is conducting. When applying a bias at the gate, cations from the electrolyte solution enter the polymer bulk to compensate the negatively charged sulfonate moieties of the PSS. The result is a decrease in the hole density, and as a consequence a decrease in the polymer conductivity because only a lower current can flow through the channel [162]. In this way, an OECT device is capable of converting an ionic current into an electronic one. Taken together with the possibility of operating an OECT at low voltages (below 1V), which allows an operation in aqueous medium without introducing Faradaic currents, makes an OECT a favorable tool to monitor biological phenomena. One of the first application of an OECT at the interface with biology was the use as an enzymatic sensor, followed by applications as ion, nucleotide and other macromolecules sensors [179].

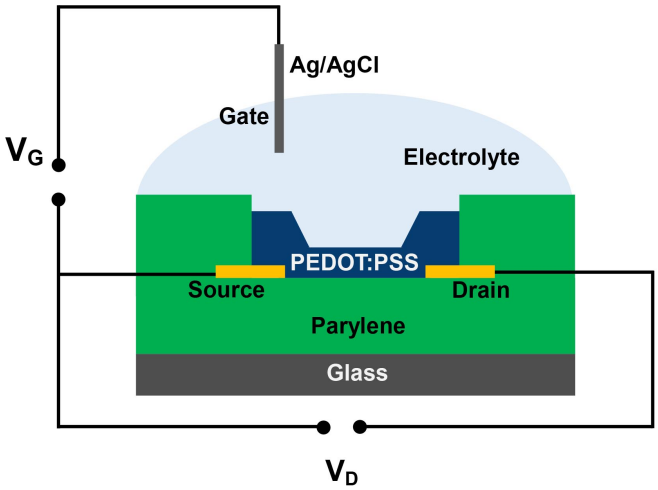

Figure 26: Schematic representation of the OECT used in the study of Malliaras *et al.* in 2013. The array is embedded in parylene, which provides a flexible the device. The semiconducting layer is made of PEDOT:PSS and the source and drain electrodes of gold (modified from [180]).

As described above in section 2.3.1, electrophysiological signals are generated by ionic currents and cells can be subdivided into excitable (neurons, cardiomyocytes etc.) and non-excitable cells (such as astrocytes). Theoretically OECTs would provide an optimal system to directly convert ionic currents from living tissue into electronic ones.

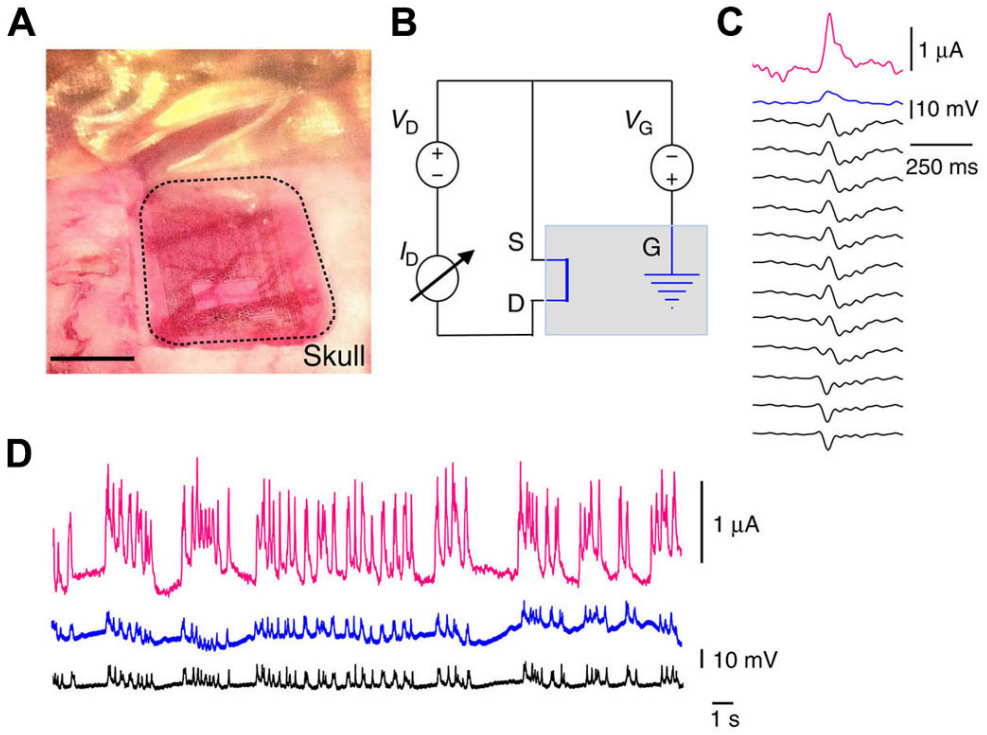

Figure 27: (A) ECoG probe placed over the somatosensory cortex of an anesthetized rat. (B) Electrical circuit of the OECT, the gray box indicates the brain of the rat. (C) Bicuculline-induced epileptiform spike recorded from a transistor (pink), a PEDOT:PSS surface electrode (blue) and 12 Ir-penetrating electrodes (black). (D) Recordings from an OECT (pink), a PEDOT:PSS surface electrode (blue) and an Ir-penetrating electrode (black). (Reprinted with permission from [180], Copyright 2016, Nature Publishing Group)

Currently in clinical use for the brain are three electrophysiological recording techniques: electroencephalography (EEG) with electrodes getting attached to the patient's skin, electrocorticography (ECoG) where electrodes are placed on the surface of the brain, and stereoelectroencephalography (SEEG) where probes are inserted deep into the brain [179]. However in 2013, the group of Malliaras reported for the first time in vivo electrophysiological recording of brain activity with an OECT [180]. The array was embedded in an ultra-thin film of patterned parylene, providing a highly flexible and conformable device, optimal for the brain surface. The semiconducting layer consisted of PEDOT:PSS and the integrated electrodes of gold. A schematic representation is shown in figure 26. This ECoG probe was then placed on the somatosensory cortex of an epileptic rat. By perfusing the GABAA-receptor antagonist bicuculline on the surface of the brain, they evoked a seizure-like spiking activity. In comparison to surface PEDOT:PSS microelectrodes and control penetrating electrodes, they reported a better signal-to-noise ratio, which they attributed to

the local signal amplification through the OECT. The obtained electrophysiological signal was described as similar to the one obtained with penetrating electrodes.

Due to the possibility to directly convert ionic to electric currents, together with the good biocompatibility, flexibility and the good signal-to-noise ratio, the OECT represents currently one of the most promising devices for extracellular electrophysiological recording. It is also imaginable that even slight changes in the membrane potentials of unexcitable cells like astrocytes might be recorded with an OECT. Still, one of the drawbacks of the OECT is the reference electrode and the counter electrode used in the measurements, which is an obstacle in miniaturization and still remaining bulky [181]. Moreover the PEDOT:PSS semiconducting layer tends to degrade rather quickly in the harsh biological environment, making the the OECT unsuitable for long term recordings.

2.5.5 *Hybrid biointerfaces*

Another important application for organic materials in bioelectronic interfaces is the realization of retinal prosthetic devices. Again the soft nature of the materials come into play, but also a reliable transduction of the information carried by light into electrical activity to be transferred in visual information processing networks is a crucial point. Organic semiconductors were described to be capable of closely reproducing the color response function of the human retina [155, 152].

In 2011, Ghezzi and others reported on the functional interfacing of an organic semiconductor with a neuronal network and demonstrated photostimulation of neuronal activity with visible light [155]. The active layer of the interface consisted of the polymer-blend P3HT:PCBM that was introduced in section 2.4.5, together with the working principle of a bulk heterojunction. As described above, P3HT works as the electron donor, whereas PCBM is the electron acceptor. The authors found ITO/P3HT:PCBM treated with PLL to be biocompatible with primary hippocampal neurons. Also the physiological properties of hippocampal neurons cultured on the material were evaluated with the patch-clamp technique and all evaluated parameters (V_{mem}, frequency and amplitude of spontaneous excitatory currents, firing rate) were found to be similar in comparison to control that consisted of ITO-coated glass with PLL.

To investigate whether the light efficacy would trigger neuronal activity, they performed whole-cell patch-clamp recordings under photostimulation (figure 28A, B). The authors were able to elicit spike trains with light pulses (20 ms at 1 Hz, figure 28C) with a percentage of failures below 15%. They found that when the stimulus was hitting precisely the cell body, action potentials could be reliably evoked, whereas it would be ineffective when it was placed beside the cell (figure 28D).

Even though a number of options were postulated, and the authors favored a purely capacitive mechanism due to very low generated photocurrents, the transduction mechanism remains unclear. The photostimulation was also stated as unspecific for selected neuronal populations. However this approach, taken also together with further studies of this group (see in particular *Ghezzi et al. 2013* [152], where a P3HT-based optoelectronic interface restored the light sensitivity in rat retinas with photoreceptor degeneration), it can be said that promising opportunities are arising for this type of devices to realize the goal of artificial vision.

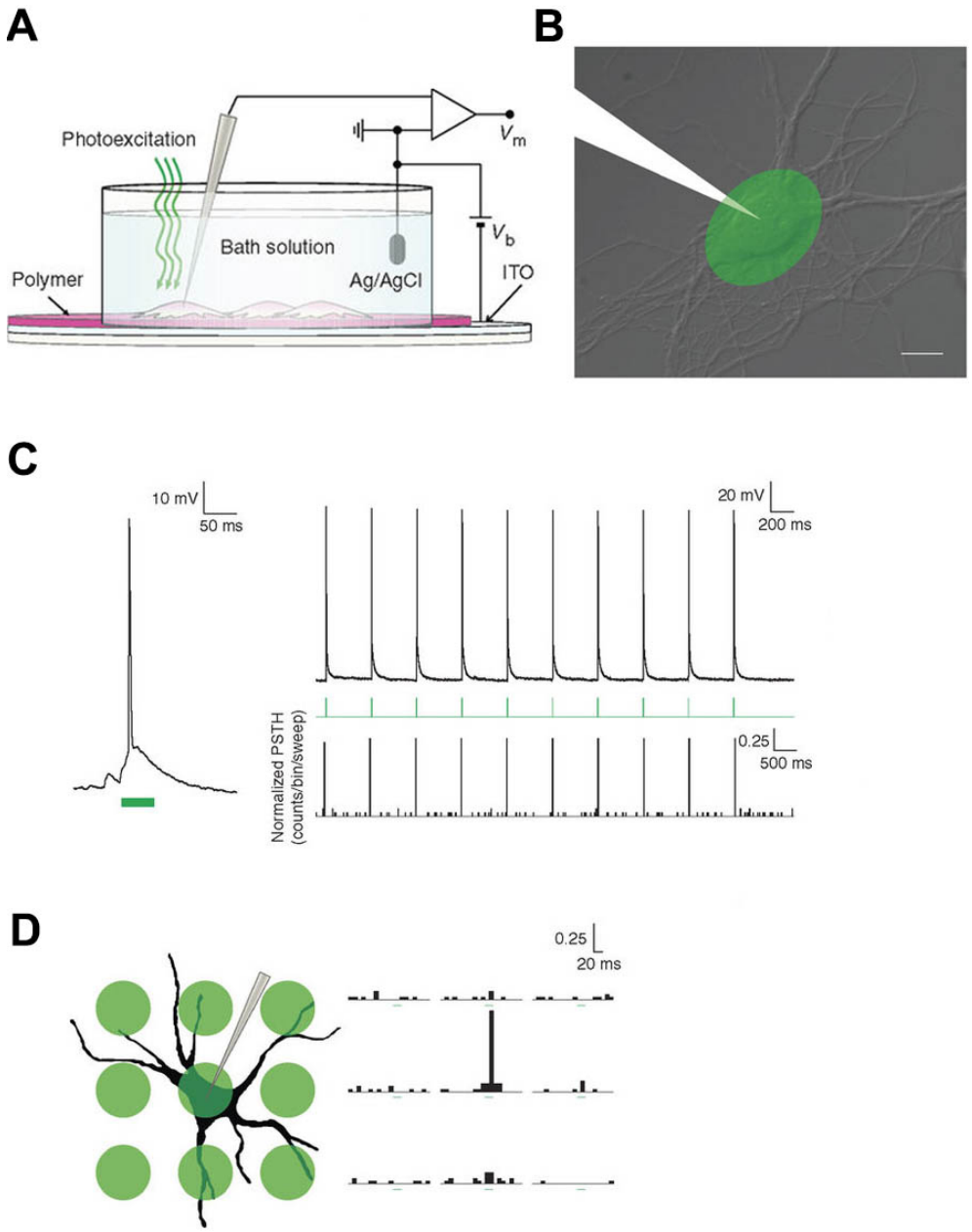

Figure 28: (A) Schematic representation of the photosensing interface. The neuronal network is grown on top of the polymer layer for patch-clamp recording (B) Schematic representation of the localization of the optical stimulus in the patched neuron. (C) Action-potential generated in response to the photostimulation pulse (50 ms) and spike train generated with a pulsed photostimulus. (20 ms pulses with a frequency of 1 Hz, green trace). (D) Spatial properties of the photostimulating interface. A grid of nine spots (diameter 20 µm, spacing 30 µm) was overlaid to a patched neuron and spikes were counted to exclude spontaneous activity. The little histogram plots on the right side represent the spike counts per number of sweeps in all recorded neurons. Each histogram represents spike count at the corresponding stimulation spot (green circles in the left panel). (Reprinted with permission from [155], Copyright 2016, Nature Publishing Group)

Part II

MATERIALS AND METHODS

3 MATERIALS AND METHODS

Manufacturers of chemicals, buffers and tissue culture media are listed in the appendix.

3.1 CELL CULTURE

All primary cell cultures were prepared at the Department of Pharmacy and Biotechnology of the University of Bologna. All procedures and handling of animals were performed according to procedures approved by the Ethical Committee for Animal Experimentation of the University of Bologna. Every effort was taken to reduce the number of animals and their suffering.

3.1.1 *Astrocytes*

PREPARATION OF ASTROCYTES Neonatal rats p0 - p2 (Sprague Dawley) were sacrificed by decapitation. The head was cleaned with 70% EtOH, then fixed with a sterile needle. The skin was opened at the midline of the head with microdissecting scissors, cutting from the base of the skull to the mid-eye area. The skull was opened at the midline fissure avoiding to cut into the brain tissue, then removed carefully with forceps. The meninges were gently peeled off by tipping over the brain tissue with sterile cotton swabs. With a scalpel, the cerebellum was cut off. With a spatula, the two hemispheres were separated, then a shallow layer of each cortical hemisphere was removed and transferred into 3 ml of tissue culture medium containing 15% FBS (see table 1). The tissue was dissociated mechanically, using a micropipette and tips with decreasing diameter, until the tissue was completely dissociated. The dissociated cortex was then filtered through a nylon cell strainer. Afterwards, the cell strainer itself was rinsed with medium. The filtrate was transferred into a 25 cm^2 tissue culture flask and incubated at 37°C, 5% CO_2.

Two days after preparation, the medium was carefully changed to remove the debris from preparation. Afterwards, every second day, the flasks were rinsed with pure Dulbecco's Modified Eagle Medium (DMEM) and shaken to remove debris and undesired cell types. The cells were maintained in medium containing 15% FBS (table 1) After reaching confluence, astrocytes were maintained in culture medium containing 10% FBS (see table 1). After 2-3 weeks, astrocytes were re-plated onto the respective substrates by enzymatical dispersion, using 0.25% trypsine-EDTA, seeded at the required concentration per substrate and maintained in culture medium containing 10 %FBS [182, 183, 184, 185].

	15% FBS	10% FBS
DMEM	84% (168 ml)	89% (178 ml)
FBS	15% (30 ml)	10% (20 ml)
PenStrep*	1% (2 ml)	1% (2ml)

Table 1: Medium for preparation and maintainance of primary astrocytes. Numbers in brackets indicate the volume needed for the preparation of 200 ml. *penicillin-streptomycin (100 U/mL and 100 mg/ml respectively) [182].

3.1.2 *Dorsal Root Ganglia*

PREPARATION OF DRG NEURONS Postnatal rats p7 - p21 (Spraugue Dawley) were anesthetized with Halotane prior to decapitation. A midline incision was made along the back with microdissecting scissors and the skin deflected laterally. The spinal column was removed and cleaned from attached tissue with a scalpel. The spinal column was then cut in half along the ventral side with a sharp scalpel, then pulled apart and the medula was taken out. The DRGs were located under a dissecting microscope in their small cavities along the lateral vertebral column and carefully spooned out by microforceps in order not to squeeze them, then transferred into a Petri dish with PBS (RT). With the scalpel any fibrous tissue surrounding the DRGs and the attached nerve roots were cut under the dissecting microscope. Afterwards, the ganglia were rinsed in an Eppendorf cup with PBS, then transferred into a Petri Dish with DMEM containing 5000 U/ml type IV collagenase for 45 - 75 min at 37°C, 5 % CO_2, and then dissociated gently with some passages through 0.5 mm and 0.6 mm sterile needles. Cells were washed by resuspension and centrifugation (960 rpm, 10 min) and then appropriately diluted in 1 ml of medium (see table 2). Cells were then seeded onto the respective substrates as described in 3.2 and maintained in medium completed with cytosine β-D-arabinofuranoside (ArAc, 1.5 mg/mL), a cytostatic that to reduces glial cell expression, and nerve growth factor (NGF, 50 ng/mL; see table 2) [186].

DMEM	89%	(44.5 ml)
FBS	10%	(5 ml)
PenStrep*	1%	(500 µl)
ArAc	0.1%	(50 µl)
NGF	0.1%	(50 µl)

Table 2: Complete medium for DRG neuron maintenance. Numbers in brackets indicate the volume needed for the preparation of 50 ml. *penicillin-streptomycin (100 U/mL and 100 mg/ml respectively) [13].

3.2 PREPARATION OF SUBSTRATES

3.2.1 *Coverslips*

Glass coverslips were soaked in 70% EtOH at RT overnight, then dried under laminar flow in a sterile hood.

3.2.1.1 *Coating of coverslips for cellular adhesion*

POLY-D-LYSINE PDL (PLL accordingly) was diluted to a final concentration of 0.1 mg/ml in PBS. A drop to wet the whole coverslip was applied, then the substrates were incubated for 20 min at RT. The drop was aspired and the coverslip rinsed three times with sterile, distilled water.

LAMININ For neuronal cells, coverslips were first treated with Poly-Lysine as described above. After the third washing step, the coverslips were incubated with Laminin in PBS at a final concentration of 10 µg/ml for 20 min. The solution was aspired and the coverslips rinsed three times with distilled sterilized water.

3.2.1.2 *Deposition of organic materials on coverslips*

T4LYSINE T4Lys was dissolved in distilled water to a concentration 1 mg/ml. 100 µl of solution was dropcasted on glass coverslips and left drying under laminar flux for 3 h at RT. The thickness of the films prepared for experiments with cell culture was measured by performing profile measurements on three different samples (Profilmeter KLA Tencor) and it was 244 $\pm$ 38 nm.

P13 P13 thin-films of the respective thickness (15, 50 or 80 nm) were sublimed under high vacuum in an Edwards 306 sublimation chamber at a rate of 0.1 $Å s^{-1}$ and at a pressure of $2x10^{-6}$ mbar onto pre-cleaned glass coverslips. P13-coated coverslips were then sterilized under the UV for 30 min. Afterwards, coating was applied as described above (see 3.2.1.1).

3.2.2 *O-CST*

O-CST FABRICATION O-CST devices were fabricated in top-contact and bottom-gate configuration with an additional capping layer of organic semiconducting material on top of the contacts. The substrates consisted of glass coated with a 150 nm thick layer of spattering deposited Indium Tin Oxide (ITO). Before deposition the substrates were cleaned by multiple sonications in acetone and 2-propanol. 420 nm of PMMA were deposited on top of the ITO layer by spin-coating in air and annealed for 12 h a 120 °C in vacuum. The 15 nm thick P13 thin film was grown by sublimation under high vacuum at a base pressure of 10^{-6} mbar in an Edwards 306 sublimation chamber at a rate of 0.1 $Å s^{-1}$. 30 nm thick gold electrodes were deposited in high vacuum at a pressure of 3-4 x 10^{-6} mbar at a growth rate of 0.1 nm s^{-1}. The channel length between two gold electrodes was set to 70 µm. A 50 nm thick P13 capping layer was vacuum sublimed on top of the gold electrodes under the same conditions as described before. O-OCST devices were then sterilized under the UV for 30 min.

Afterwards, additional coating for cell adhesion was applied as described above (see 3.2.1.1).

O-CST OPERATION Specific voltage protocols were applied to the O-CST by a custom-made 2612A Dual-channel System Source Meter Instrument (Keithley).

3.3 PATCH CLAMP

A general introduction into the working principles of the patch-clamp technique can be found in section 2.3.1. Electrophysiological experiments were performed on a setup based on a Nikon Eclipse Ti-S microscope. Whole-cell patch-clamp recordings were performed 24-72h after re-plating in voltage- or current-clamp mode at RT using patch pipettes (2-4 MΩ tip-resistance) pulled from thin-walled borosilicate glass capillaries. Responses were amplified (Multiclamp 700B, Axon Instruments), digitized (Digidata 1440A, Axon Instruments) and stored on a computer for off-line analysis. Further analyses were carried out using pClamp 10 (Axon Instruments) and Origin 9.0 (OriginLab Corporation). Capacitative transients were compensated by the nulling circuit of the recording amplifier. Because of the large current amplitude, the access resistance (below 10 MΩ) was corrected 70-90%.

Ion channel blockers were diluted to their final concentration as described in table 3 in external standard solution (see table 4). The bath saline was then replaced by saline containing the respective blocker and experiments were conducted after 5 min of incubation time. When perfusing the cells with salines containing different pharmacological agents, they were applied via a gravity-driven, local perfusion system with a flow rate of about 200 µl/min,

BAPTA-AM	10 µM
Brilliant Blue	1 µM
Carbenoxolone	50 µM
Gadolinium(III)chloride	10 µM
HC30031	30 µM
RN-1734	10 µM
Ruthenium Red	10 µM

Table 3: Final concentrations of blockers applied for patch-clamp and calcium imaging experiments prepared in external standard solution (see table 4)

3.3.1 *Calculation of astrocytic electrophysiological properties*

CAPACITANCE The capacitance of the cell membrane is proportional to the surface area with about 1µF/cm^2 [187]. The value the cell capacitance was taken directly before recording, using the cell capacitance compensation of the Multiclamp amplifier.

RESTING MEMBRANE POTENTIAL The resting membrane potential (= zero current potential) was obtained by setting the current given by the amplifier to zero.

REVERSAL POTENTIAL The reversal potential was obtained from ramp current trace recordings, plotting the current vs. the set voltage.

CURRENT DENSITY The maximal current density (I_{max}) was calculated by normalizing the obtained current value (I) at a chosen voltage (for the inward current density -120 mV, for the outward current density +60 mV) for the cell capacitance (Cp):

$$I_{max} = \frac{I}{Cp} \tag{2}$$

INPUT RESISTANCE The input resistance (IR) was obtained from recorded current traces, where the given stimulation was a voltage step (ΔV, from V_H= -60 mV to -120 mV for astrocytes). The change in current (ΔI) was then used to calculate the input resistance:

$$IR = \frac{\Delta V}{\Delta I} \tag{3}$$

SPECIFIC CONDUCTANCE The specific conductance (SG) was obtained from the reciprocal of the input resistance (IR), normalized by the cell capacitance (Cp):

$$SG = \frac{1}{IR} Cp \tag{4}$$

3.3.2 *Calculation of neuronal firing properties*

The capacitance and the resting V_{mem} (see figure 29-a) were obtained as described in section 3.3.1. The action potential (AP) and neuronal firing properties were recorded in current-clamp mode by injecting repetitive increasing current pulses from 25 to 250 pA of 100 ms duration. The AP amplitude was measured between the peak and AP threshold level. The current threshold I_{th} was determined as the minimum current injection required evoking an AP. The AP voltage threshold V_{th} was defined as the first point on the upstroke of an AP (figure 29-b). The AP rising time to peak (figure 29-c) was defined as the time for rising from baseline to the AP peak (figure 29-d). The after hyperpolarization potential (AHP) amplitude (figure 29-f) was measured between the maximum hyperpolarization and the voltage plateau final. The AHP duration was the time between these two points (figure 29-e). The maximal number of firing was calculated by counting the number of overshooting AP in response to a 100 ms pulse of current injection [14].

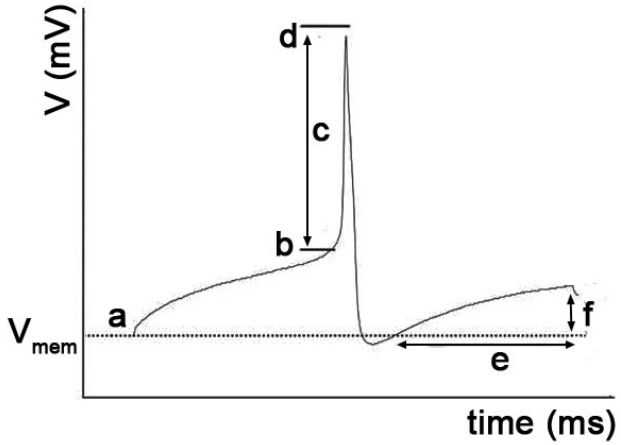

Figure 29: Parameters of DRG neuron action potentials. (a) Resting V_{mem}, (b) first point of upstroke, (c) time to peak, (d) peak, (e) AHP duration, (f) AHP amplitude (modified from [14])

3.3.3 *Patch-clamp standard solutions*

All salines for patch-clamp experiments were prepared with salts of the highest purity grade and de-ionized and sterilized water. After pH-adjustment with the respective acid or base, the osmolarity was adjusted with mannitol if not stated otherwise.

3.3.4 *Standard solutions for astroytes*

NaCl	140 mM
$MgCl_2$	2 mM
KCl	4 mM
$CaCl_2$	2 mM
HEPES	10 mM
Glucose	5 mM
Mannitol	20mM
pH 7.4 with 1N NaOH, osmolarity ~ 315 mOsm	

Table 4: External standard solution for astrocytes. [182]

KCl	144 mM
$MgCl_2$	2 mM
EGTA	5 mM
HEPES	10 mM
pH 7.2 with 1N KOH, osmolarity ~ 295 mOsm	

Table 5: Internal standard solution for astrocytes. [182]

CsCl	126 mM
$MgCl_2$	2 mM
EGTA	1 mM
TES	10 mM
pH 7.2 with 1N CsOH, osmolarity ~ 295 mOsm	

Table 6: Internal CsCl-solution for astrocytes. [188]

NaCl	140 mM
$MgCl_2$	4 mM
KCl	4 mM
HEPES	10 mM
EGTA	0.5 mM
Mannitol	20mM
pH 7.4 with 1N NaOH, osmolarity ~ 315 mOsm	

Table 7: Calcium free external standard solution for astrocytes. [182]

CsCl	140 mM
$MgCl_2$	2 mM
$CaCl_2$	2 mM
TES	10 mM
Glucose	5 mM
pH 7.4 with 1N CsOH, osmolarity ~ 315 mOsm	

Table 8: External cesium standard solution for astrocytes. [188]

CsCl	22 mM
$CaCl_2$	2 mM
$MgCl_2$	2 mM
TES	10 mM
Glucose	5 mM
Gluconic acid	100 mM
pH 7.2 with 1N CsOH, osmolarity ~ 295 mOsm	

Table 9: Internal CsGluconate solution for astrocytes. [188]

3.3.5 *Standard solutions for Dorsal Root Ganglia*

NaCl	140 mM
$MgCl_2$	2 mM
KCl	4 mM
$CaCl_2$	2 mM
HEPES	10 mM
Glucose	5 mM
Mannitol	20mM
pH 7.4 with 1N NaOH, osmolarity ~315 mOsm	

Table 10: External standard solution for DRG neurons. [13]

KCl	144 mM
$MgCl_2$	2 mM
NaATP	2 mM
EGTA	5 mM
HEPES	10 mM
pH 7.2 with 1N KOH, osmolarity ~295 mOsm	

Table 11: Internal standard solution for DRG neurons. [13]

3.4 FLUORESCEIN DIACETATE ASSAY CELL VIABILITY ASSAY

The Fluorescein diacetate (FDA) assay was used to test the cell viability. Cells are stained with cell-permeable FDA, a non- fluorescent fluorescein analogue. In living cells it is hydrolysed to fluorescent fluorescein by cellular esterase activity, cleaving off the acetate groups. In this way, living cells can be visualized by fluorescence microscopy [189].

The FDA stock solution (5 mg/ml) was prepared in acetone and 3.3 µl of the stock solution was diluted in 1 ml of phosphate buffered saline (PBS). Astrocytes plated on O-CSTs or coverslips were incubated with the FDA dilution for 5 min at RT, washed with PBS and characterized by Nikon eclipse 80i fluorescent inverted microscope equipped with a 20x or 40x air objective. Living cells were counted and the number of cells/area was calculated and compared at each desired time point.

3.5 STATISTICAL ANALYSIS

Data were compared by one-way ANOVA with Bonferroni post-test or student's t-test. A statistically significant difference was reported if $p<0.05$ or less. Data are reported as the mean $\pm$ Standard Error (SE) from at least three independent experiments.

Part III

RESULTS AND DISCUSSION

4

A BIOMODIFIED QUATERTHIOPHENE SEMICONDUCTOR AS ORGANIC NEURAL INTERFACE.

As described in 2.4.6, interfacing a semiconductor surface with cells requires still a coating layer of extracellular matrix proteins to enable the adhesion and growth of cells. These additional treatments are a nontrivial part within the fabrication procedure and limit the use of currently available technologies for electrophysiological recording by causing a decrease of the recording sensibility. For this purpose, a modified quaterthiophene bearing lysine-ends (T4Lys) was investigated as a functional platform for neural cell growth, aiming to combine a material's semiconducting functionalities while at the same time enhancing cell adhesion and neurite outgrowth.

4.1 BIOCOMPATIBILITY OF T4LYS WITH PRIMARY DRG NEURONS

As a first step to assess the capability of T4Lys to enable adhesion and growth of neural cells, primary DRG neuron cultures were plated on glass coverslips coated with T4Lys, T4, and PLL. Fluorescein diacetate (FDA) viability assays were performed after 2 and 8 div from cell plating. Fluorescent images, taken after 8 div (figure 30A), revealed that viable cells could be found on coverslips coated with PLL and T4Lys films. On contrary, almost no living cells could be detected on T4 crystals.

The histogram plot of averaged cell density (number of cells per area) at 2 and 8 div (figure 30B) showed that the total number of cells in the culture (neuronal and non-neuronal) was significantly lower on T4-Lys after 2 and 8 div compared to Glass+PLL seeded cells (figure 30B, grey and orange bars). Additionally a significantly higher number of cells was countable on T4Lys in comparison to pristine T4 at both time points (figure 30B, blue bars under red arrow).

The reason in the decreased adhesion of DRG neurons on T4 and T4Lys can be found in the material's properties. In case of pristine T4, the material forms scattered large rhomboidal crystals with a very high roughness and a decreased wettability/hydrophilicity (contact angle: 89.1 $\pm$ 2.6°). On the contrary, T4Lysine forms a uniform film, comparable to PLL on glass. Still T4Lys cast films show a considerably higher roughness (23.2 $\pm$ 1.9 nm) in comparison to Glass+PLL (0.35 $\pm$ 0.01 nm) and a contact angle of 44.8 $\pm$ 1.9°, which is higher than the one of PLL coated glass (29.6 $\pm$ 2.6°), suggesting that lysine functionalization of T4 improves the wettability/hydrophilicity with respect to the unmodified T4 substrate, but doesn't fully reach the properties of Glass+PLL [118]. Due to the negligible adhesion and growth of DRG neurons on T4, this material was not included in the further investigation.

To confirm that cells found on T4Lysine were indeed neurons, cells were stained for neuronal nuclear protein (NeuN), a neuronal nuclear antigen [190]. The average of percentage of NeuN-positive cells, with respect to the total number of cells, was found to be significantly higher in T4Lys plated DRG cultures than in Glass+PLL plated ones (78 $\pm$ 1% for T4Lys and 49 $\pm$ 2% for PLL, see figure 31A) [118].

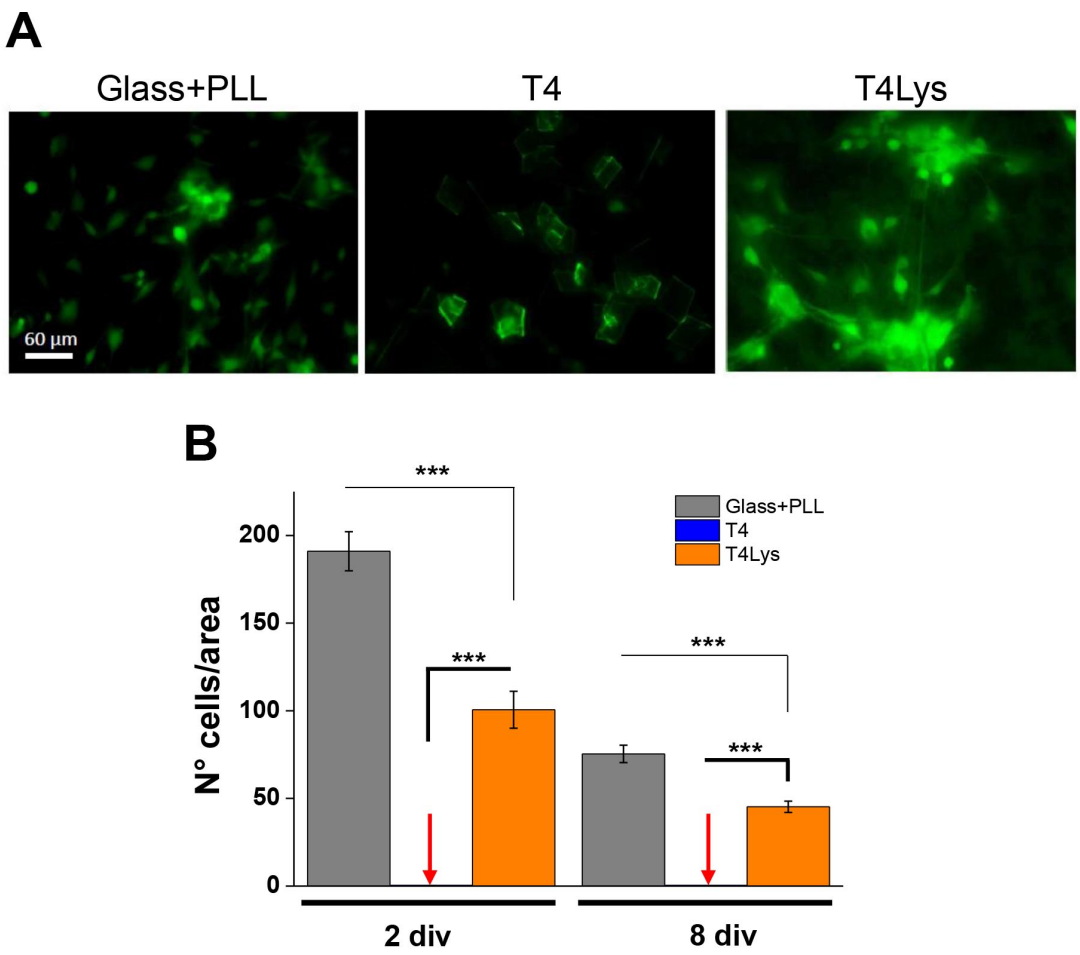

Figure 30: (A) Confocal images of fluorescein diacetate (FDA)-stained DRG cell cultures plated on Glass+PLL, casted T4 and T4Lys films, captured after 8 div. On pristine T4, due to the formation of scattered large rhomboidal crystals, almost no cells were able to adhere. (B) Histogram plot of FDA-positive cells, normalized by the area on DRG neurons grown on PLL, casted T4, and T4Lys, after 2 and 8 div. Red arrows: T4 crystals did not allow cell adhesion, therefor the number of cells is negligible (n=10 PLL, n=10 T4, and n=18 T4Lys for 2 div; n=10 PLL; n=10 T4, and n=18 T4Lys for 8 div. For each sample, 20 image fields were taken and analyzed. ***p<0.001, One-way ANOVA).

In order to verify the impact of T4Lys on neuronal neurite re-growth, cells were stained for growth-associated protein (GAP43), which is expressed in cell bodies and outgrowing neurites of DRG neurons [191]. GAP43 immunofluorescent staining performed after 5 div revealed not only the presence of neurons with axonal regenerating processes on T4Lys and Glass+PLL seeded neurons, but also that neurites of neurons grown on T4Lys were almost 50% longer than those on Glass+PLL control substrates (figure 31B).

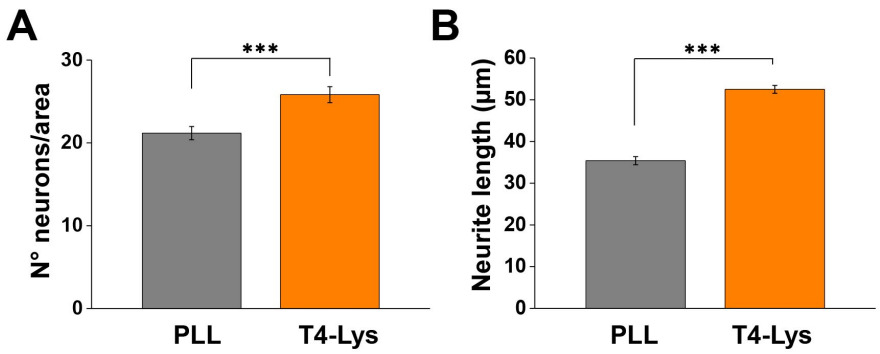

Figure 31: (A) Histogram plot of the number of NeuN-positive cells/area on Glass+PLL (grey bar) and T4Lys (orange bar) plated cell cultures. (n=79 for PLL and n=95 for T4Lys; ***p<0.001, One-way ANOVA) (B) Histogram plot representing neurite length measured in neurons grown on PLL (grey bar) and T4Lys (orange bar). (number of neurites measured for each condition: n=386 for PLL and n=789 for T4Lys; ***p<0.001, One-way ANOVA)

Taken together, these results indicate that the lysine functionalization of T4 results in enabling cell adhesion and differentiation of primary DRG neurons.

4.2 T4-LYSINE PRESERVES THE ELECTROPHYSIOLOGICAL PROPERTIES OF DRG NEURONS

An important aspect of interfacing neurons with organic bioelectronics is the capability of the interface to preserve the bioelectrical properties of neurons. By these means, whole-cell patch-clamp experiments on DRG neurons, 72 h after plating on Glass+PLL and T4Lys samples, were performed as shown in figure 32. Cells were voltage-clamped at a holding potential of −60mV in control intracellular and extracellular saline (see tables 4 and 6), then families of current pulses from 25 to 250 pA amplitude with increasing steps of 25 pA and a duration of 100 ms were injected to evoke neuronal action potentials. Representative current-clamp traces of the first action potential (AP) evoked from cultured DRG neurons plated on Glass+PLL and T4Lys are shown in figure 33A and B respectively. A comparative analysis of the evoked action potential and calculated passive and excitability properties is displayed in table 12.

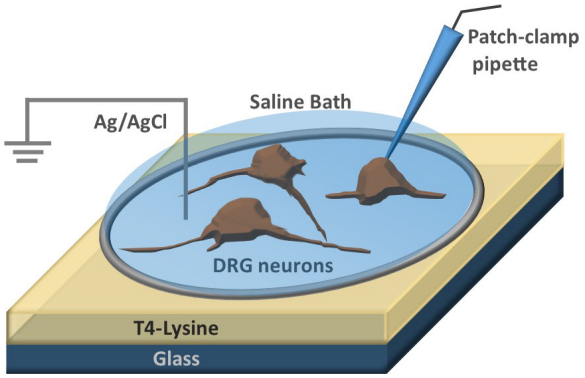

Figure 32: Schematic representation of patch-clamp experiments of DRG neurons seeded on T4Lysine coated coverslips.

In response to threshold current injection, neuron depolarization lead to neuronal firing, which occurred as single (figure 33) as well as repetitive (figure 34) firing in T4Lys as well as Glass+PLL seeded neurons. A slightly higher number of neurons with repetitive firing in T4Lys seeded cells compared to Glass+PLL cultured neurons could be found. In Glass+PLL cultured neurons, from 24 cells only three cells showed repetitive firing and 21 were firing single (phasic) action potentials. Of the 18 neurons analyzed in total on T4Lys, eight cells showed repetitive firing and ten cells single firing. Accordingly, the maximal firing rate was higher in T4Lys firing neurons compared to cells plated on Glass+PLL.

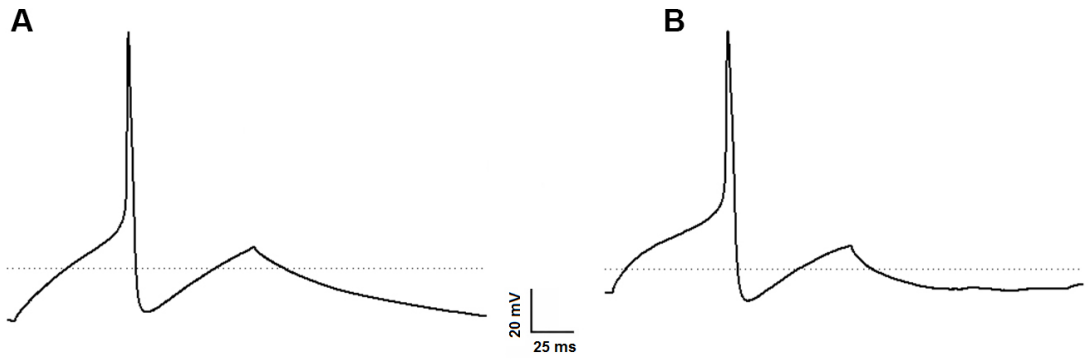

Figure 33: Representative traces of DRG neuron action potentials on Glass+PLL and T4Lys. Dotted line represents the holding potential of -60 mV.

The comparative analysis of the average active and passive electrophysiological properties revealed that the mean values of the cell capacitance were slightly higher in neurons plated on T4Lys, indicating a lightly increased cell surface. A possible explanation is the beginning of a significantly higher neurite outgrowth when short stumps start departing from the soma and increasing the cell surface, which leads in turn to a higher capacitance. A difference can also be reported for the resting membrane potential (resting V_{mem}) which is depolarized in neurons plated on T4Lys in comparison to Glass+PLL seeded cells and may serve as an explanation for the higher firing rate. In the other examined parameters which included the AP threshold current (I_{th}), the AP voltage threshold (V_{th}), AP peak, AP amplitude, time to peak and after hyperpolarization period (AHP) amplitude, no statistical difference could be found between the two experimental conditions.

	Cp [pF]	Resting V_{mem} [mV]	I_{th} [pA]	V_{th} [mV]	AP amplitude [mV]	Time to peak [ms]	AHP amplitude [mV]	AHP duration [ms]	Max. AP number (t=0,1s)
Glass+PLL	22.2 ± 1.2	-81.0 ± 1.2	206 ± 6	-34.8 ± 0.5	73.2 ± 1.7	2.4 ± 0.1	19.5 ± 1.7	37.7 ± 2.6	1.1 ± 0.1
T4Lys	26.4 ± 1.7	-71.4 ± 1.5 **	198 ± 6	-33.1 ± 1.2	67.7 ± 2.4	2.4 ± 0.1	17.8 ± 2.1	38.4 ± 3.0	1.5 ± 0.1 *

Table 12: Passive and excitability properties of DRG neurons seeded on T4Lys.
Cp: membrane capacitance; Resting V_{mem}: resting membrane potential; I_{th}: threshold current; V_{th}: voltage threshold; AP: action potential; AHP: after hyperpolarization period amplitude; (n=24 for Glass+PLL and n=18 for Glass+T4Lys. *p<0.05, **p<0.01, One-way ANOVA

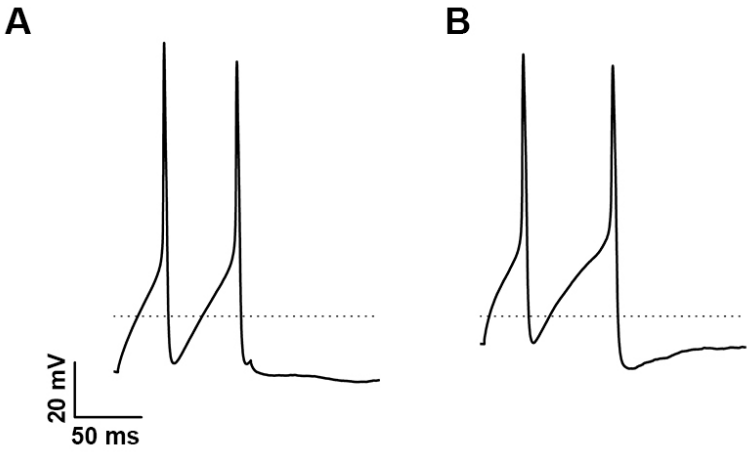

Figure 34: Representative current-clamp traces of the repetitive firing evoked from cultured DRG neurons on (A) PLL and (B) T4Lys in response to a pulse family of 100 ms duration. For PLL cultured neurons, n=3 for repetitive firing and n=21 for single firing (n=24 in total). For DRG neurons seeded on T4Lysine, n=8 for repetitive firing and n=10 for single firing (n=18 in total). The dotted line represents the holding potential of -60 mV.

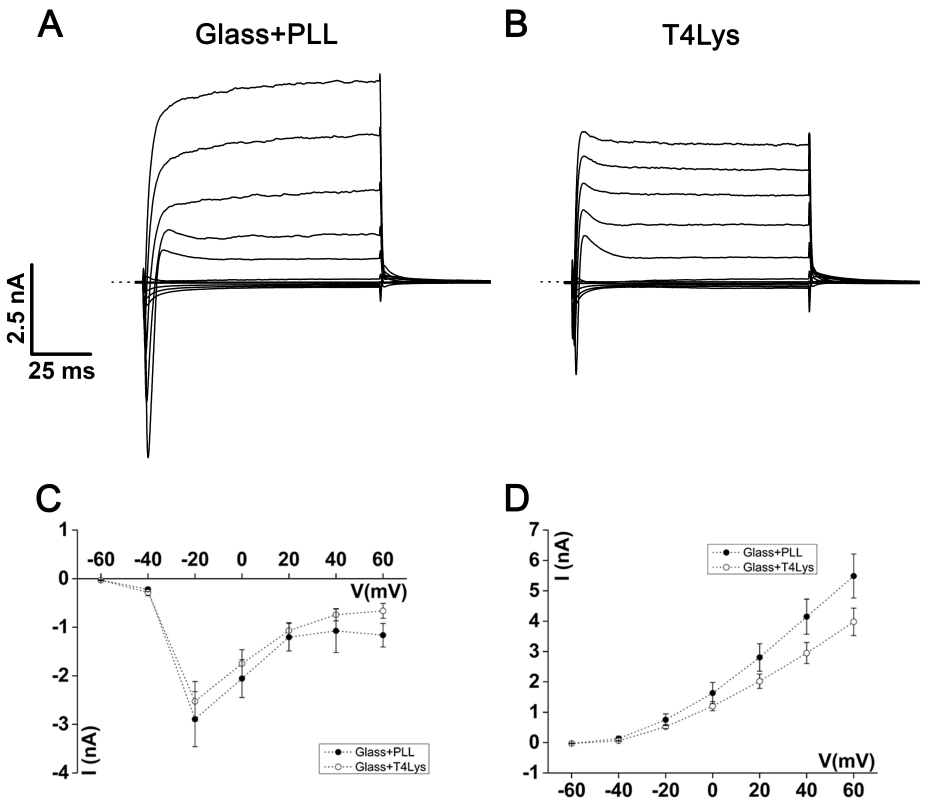

Figure 35: Representative traces of DRG neuron whole cell currents evoked with a step protocol on (A) Glass+PLL and (B) T4Lys seeded cells. Dotted line represents 0 nA. (C-D) I/V plots: Mean values of maximal inward (C) and outward (D) current densities recorded in neurons plated on PLL (black circles) and T4Lys (white circles). I/V plots have been generated by calculating the average of the maximal inward or outward current values recorded at each potential, and normalized for the relative cell capacitance values.

In order to obtain a profile of the whole-cell current of neurons plated on PLL and T4Lys, current traces (figure 35) were evoked with a family of cells voltage steps from a holding potential of −60 mV, from −120 mV to 60 mV in increments of 20 mV. The mean of maximal current density for each voltage step at peak and steady state in Glass+PLL and T4Lys seeded cells was compared, revealing a similar voltage-dependent profile of the whole cell current in the two conditions. The average threshold voltage for inward current activation was −30 mV with a maximal conductance at −20 mV. DRG neurons displayed a comparable inward current at different voltages and a similar maximum inward conductance (G_{in} max = 5.5 ± 1.1 ns pF^{-1} for PLL, n = 9, and G_{in} max = 5.3 ± 0.9 ns pF^{-1} for T4Lys cells, n = 10). In contrast, the average outward current recorded at voltages applied above 0 mV was significantly different in the two experimental conditions. (G_{out} max = 4.1 ± 0.5 ns pF^{-1} for PLL, n = 9 and G_{out} max = 3.2 ± 0.4 ns pF^{-1} for T4Lys cells, n = 10).

4.3 CONCLUSIONS

With T4Lysine, an innovative, water processable lysinated molecular organic semiconducting material was introduced [118]. Our study showed that the Lys insertion into T4 enables adhesion of primary culture of rat dorsal root ganglia. By whole-cell patch-clamp, it could be confirmed that the biofunctionality of primary DRG neurons cultured on this material was preserved. Collectively the data indicated that T4Lys is a favorable organic interface to promote the *in vitro* growth of primary DRG neurons. Moreover, the comparative quantitative analyses of the active and passive biophysical properties, in particular the difference in the resting membrane potential and the resulting increased repetitive firing of cells seeded on the novel material hint that T4Lys enables functional differentiation of primary DRG neurons. T4Lysine was the first material to be reported, where the optical and iono-electronic functionalities as well as the soft nature of an organic semiconducting material were combined with lysine for improved biocompatibility. Our study has shown the proper functioning of this innovative concept, which was then expanded on another semiconducting backbone: perylene diimide. In a second study, our group introduced the self-assembled lysinated perylene diimide (PDI-Lys, [161], see also 2.4.6) that was also found to be suitable to be interfaced with DRG neurons. These lysinated organic semiconductors have opened the door for a new type of material to be chemically realized and then integrated in bioorganic devices and can set the scene for a new step in terms of sensitivity of bidirectional communication between cells and device by reducing the cleft at the interface.

5

P13 - INTERFACING AN ORGANIC SEMICONDUCTOR WITH ASTROCYTES

5.1 P13 - A PERYLENE-BASED MATERIAL AND DEVICE

As described in 2.4.4, Perylene Tetracarboxylic Diimide derivatives such as N,No -ditridecyl perylene-3,4,9,10 tetracarboxylic diimide (P13) belong to the most promising small organic molecules to fabricate n-type organic thin film transistors (OTFTs). An organic field effect transistor (OFET) with P13 as semiconducting and capping layer has already been realized and successfully integrated with dorsal root ganglia [13]. Based on this work, P13 and a P13-OFET (hereinafter referred to as O-CST) were investigated as an interface with primary cortical astrocytes. To this end, the biocompatibility of P13 thin films with astrocytes was tested to determine the adhesion and growth of astrocytes. By patch-clamp studies the impact of P13 on astrocytic electrophysiological properties was studied. A further step was to interface cortical astrocytes with the actual device and study the modulation of the astrocytic ionic conductance with the patch-clamp technique while stimulating the cells by operating the O-CST in accumulation mode. Finally, making use of the O-CST's transparency, calcium imaging was performed on astrocytes stimulated by the O-CST, monitoring the changes of their intracellular Ca^{2+}-level.

5.1.1 *Biocompatibility of P13 thin films with astrocytes*

In order to test if P13 could be a suitable substrate to be interfaced with astrocytes, the first step was to evaluate the material's biocompatibility. Confluent astrocytes were re-plated at low density on coverslips coated with 50 nm P13. After 2, 7 and 15 days in vitro (div) from re-plating, fluorescein diacetate (FDA) cell viability assays were performed. Figure 36 A and B display single plane confocal images taken after 2 and 7 div, showing viable astrocytes plated on P13+PDL and on Glass+PDL control substrates.

Figure 36C shows the histogram plot of the cell counting study. The number of cells per area at the chosen time points reveals that the rate of adhesion, survival and proliferation was significantly higher on cells plated on P13+PDL substrates (red bars) in comparison to the Glass+PDL control (blue bars) after 2 and 7 div. After 15 div this number was comparable again on the two substrates. These data indicate that P13 is a biocompatible substrate not only for neural cells [13], but also suitable to be interfaced with primary cortical astrocytes promoting their adhesion and growth.

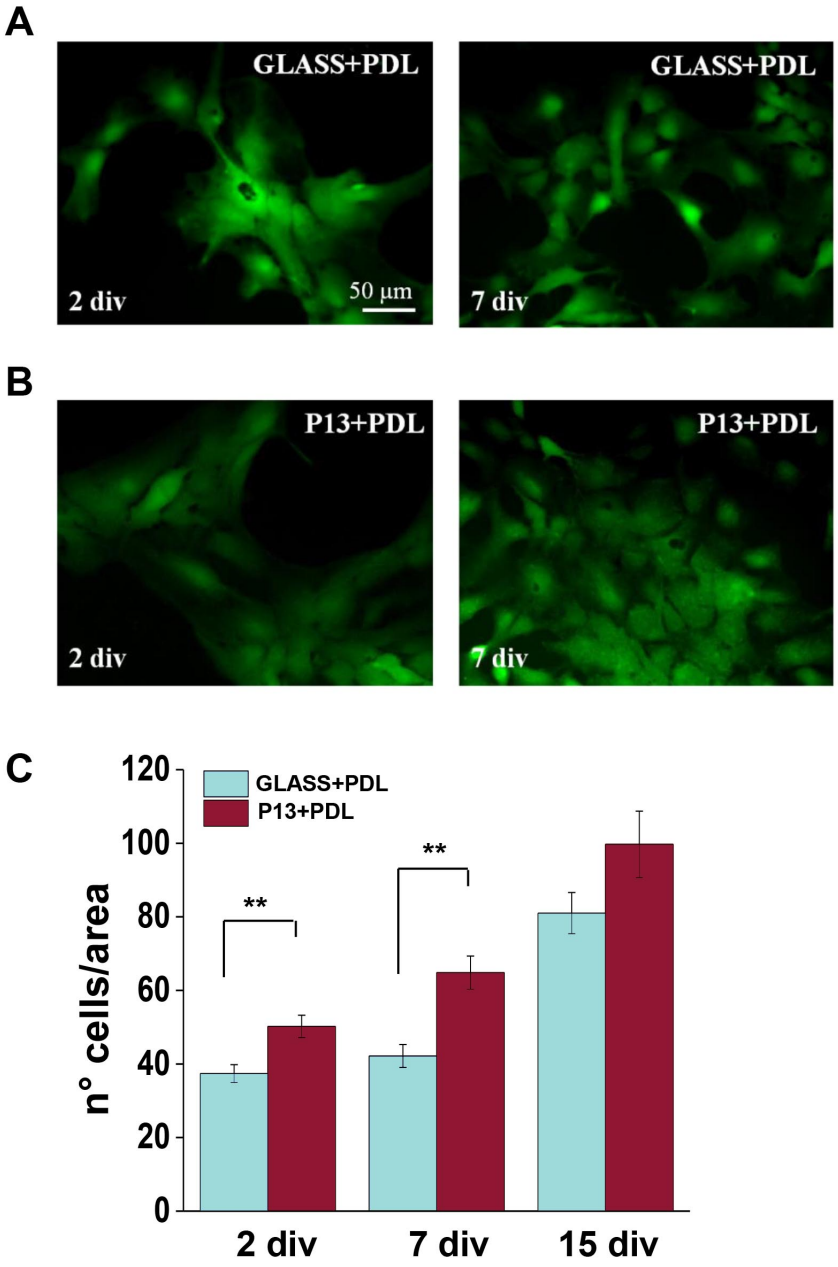

Figure 36: Fluorescent images taken after 2 and 7 DIV of astrocytes stained for FDA on (A) Glass+PDL and (B) P13+PDL (C) Histogram plot of averaged FDA positive cells/area counted on astrocytes plated on Glass+PDL and P13+PDL after 2, 7 and 15 div. A statistical difference was observed after 2 and 7 div (n= 91 PDL and n=108 P13+PDL after 2 div, n=95 PDL and n=93 P13+PDL after 7 div, n=30 PDL and n=21 P13+PDL after 15 div. ** $p<0.01$, One-way ANOVA).

5.1.2 *Evaluation of astrocytic electrophysiological properties on P13 thin films*

Primary cortical astrocytes in culture are characterized by a rapidly activating, non-inactivating, voltage-dependent current pattern, mainly carried by K^+ channels [183, 188]. PDL-plated cells display a depolarized resting membrane potential, high input resistance and a low specific conductance [182]. To verify, if the contact with

the organic material introduced any changes, whole-cell patch-clamp experiments were performed on cells seeded at low density, 24h after re-plating, on P13+PDL and Glass+PDL substrates. With control intra- and extracellular saline, cells were held at -60 mV and after stepping to -120 mV for 500 ms, a ramp from -120 mV to +60 mV (500 ms, see inset 37B) was applied to evoke whole-cell currents. Typical current traces evoked by the ramp protocol are shown in figure 37B for Glass+PDL and P13+PDL seeded cells.

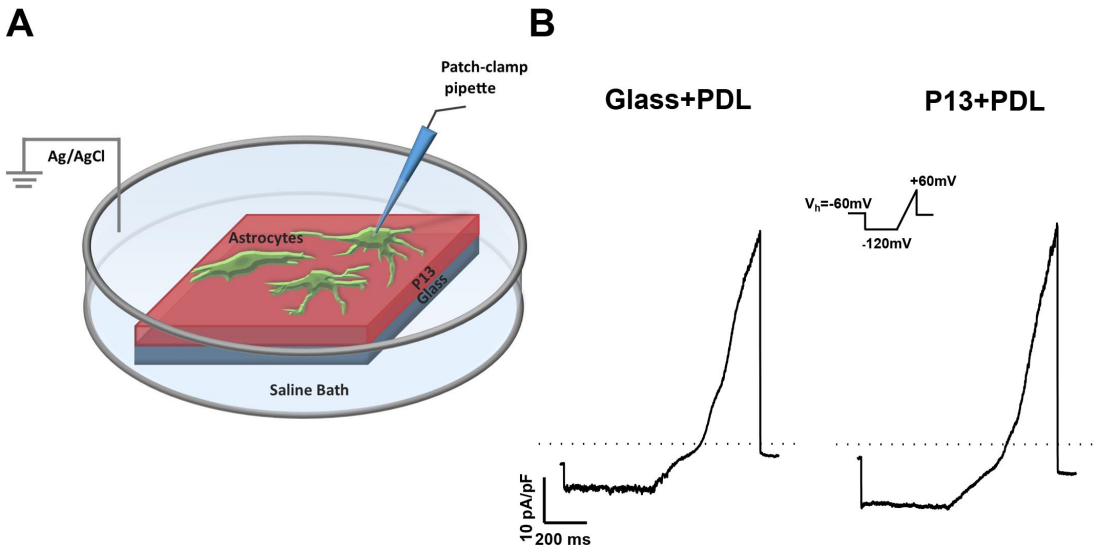

Figure 37: (A) Schematic representation of patch-clamp experiments on astrocytes seeded on P13 thin films. (B) Traces representative of astrocytic response to voltage ramp protocol from V_h of -60 mV, from -120 mV to +60 mV (depicted by the little inset). Dotted line represents 0 pA/pF.

The current amplitude was recorded and the membrane properties were calculated. A summary is shown in table 13. The resting membrane potentials and the reversal potential of cells plated on P13+PDL and Glass+PDL were comparable as well as the capacitance. Even though no statistical difference can be reported for the maximum inward current density, cells seeded on P13+PDL showed a slightly higher inward current density in comparison to cells seeded on Glass+PDL control substrates. A significant difference between the two conditions was observed in the input resistance, where the one of P13+PDL seeded cells showed was lower.

	V_{mem} (mV)	E_{rev} (mV)	Cp (pF)	I (-120mV) (pA/pF)	I (+60mV) (pA/pF)	IR (MΩ)	SG (ns/pF)
Glass+PDL	-34.9±3.2	-36.7 ± 2.9	45.71±3.9	-8.3±1.3	41.4±4.7	589.6±65.8	0.07±0.01
P13+PDL	-30.1±1.9	-35.4 ± 2.4	34.1±2.6	-12.9±2.5	38.4±3.3	404.8±34.4**	0.11±0.02

Table 13: Summary of electrophysiological properties of astrocytes seeded on Glass+PDL and P13+PDL.
Cp, membrane capacitance; V_{mem}, resting membrane potential; E_{rev}, reversal potential SG, mean specific conductance; IR, input resistance; I, current density. (n=33 for Glass+PDL and n=41 for astrocytes seeded on P13+PDL. **p<0.01, student's t-test)

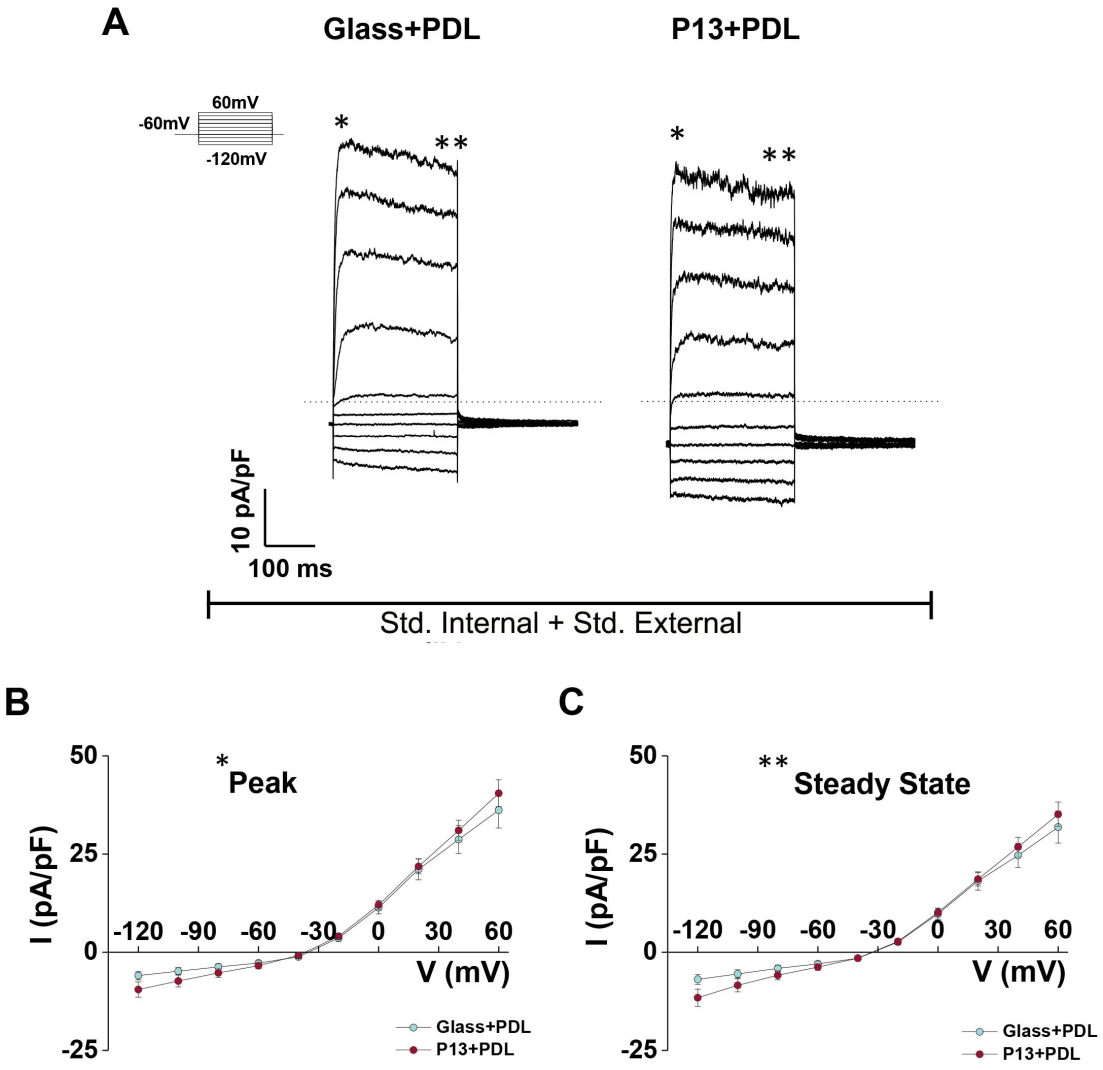

Figure 38: (A) Representative current traces evoked in astrocytes seeded on Glass+PDL and P13+PDL with a family of voltage steps from V_h of -60 mV, from -120 to 60 mV in 20 mV increments as depicted by the inset. (B-C) I/V- plots of the mean current density recorded at peak (*, B) and steady state (**, C) in astrocytes plated on Glass+PDL (blue circles) and P13+PDL (red circles). No statistical difference can be reported for peak and steady state (n=26 for Glass+PDL and n=31 for P13+PDL, *p<0.05 one-way ANOVA).

To investigate the conductance voltage-dependence of cells seeded on P13+PDL and Glass+PDL, astrocytes were stimulated with 500 ms voltage steps (V_h=-60 mV) from -120 mV to +60 mV in increments of 20 mV (inset figure 38A). Representative current traces of astrocytes plated on P13+PDL and Glass+PDL are shown in figure 38A. A comparative analysis obtained by an I/V plot of the maximal current density mean values, recorded for each voltage step, revealed a similar voltage-dependent profile of whole-cell peak (figure 38B) and steady state (figure 38C) currents of astrocytes plated on P13+PDL and Glass+PDL samples and no statistical difference can be reported.

5.2 O-CST AS A MODULATOR OF ASTROCYTIC WHOLE-CELL CONDUCTANCE

5.2.1 *Evaluation of astrocytic electrophysiological properties on the O-CST*

After testing the impact of P13 on the electrophysiological properties of primary cortical astrocytes (see 5.1.2), also the effect of the O-CST was verified on the astrocytes' electrophysiological properties. Even though the capping layer consists of 50 nm P13 like the coverslips, the P13 is not continously covering the complete O-CST surface, which consists of in total 4 seperate devices. Between these devices, PMMA is in contact with the tissue culture medium. Even though PMMA is described as biocompatible with living tissue and in particular astrocytes (see [192] and [193]), it can't be excluded that its interplay with P13 or circumstances arising from fabrication procedures and technical specifications, could still alter the astrocytic electrophysiological properties.

To this aim, whole-cell patch-clamp experiments were performed on single cells seeded at low density on Glass+PDL control substrates and on the channel of PDL-coated O-CSTs, 24h after re-plating. A scheme of the experimental setup is shown in figure 39A. Whole-cell currents were evoked by voltage clamping cells in control intracellular and extracellular saline at a holding potential (V_h) of -60 mV and, after stepping to -120 mV for 400 ms, applying a ramp from -120 to 60 mV (500ms, see inset in figure 39B). Representative current traces evoked by the ramp protocol are shown in figure 39B for Glass+PDL and O-CST+PDL seeded cells.

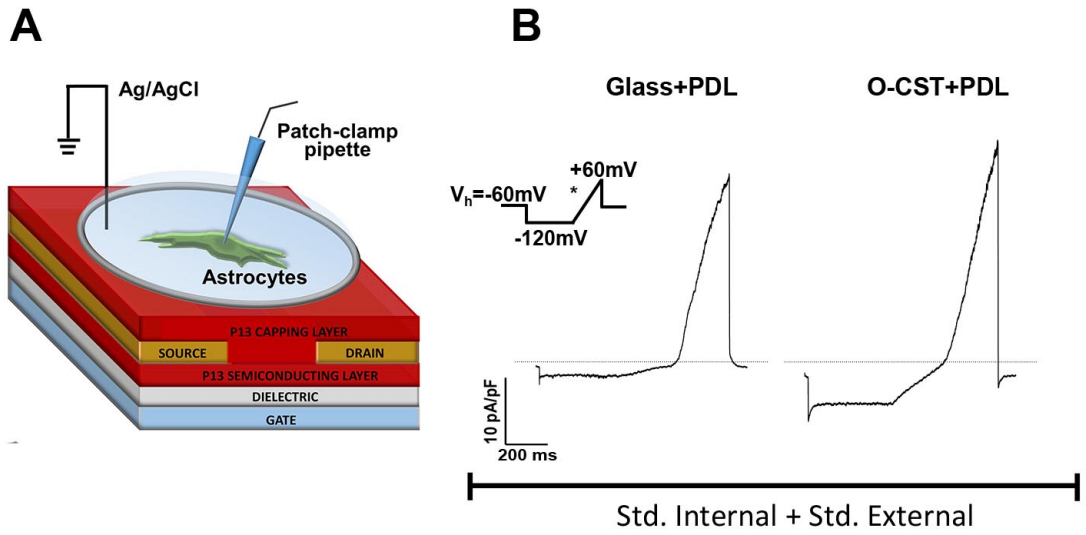

Figure 39: (A) Schematic representation of patch-clamp experiment on the O-CST with astrocytes seeded on the channel. (B) Representative ramp current traces of astrocytic response to voltage ramp protocol (inset) from V_h of -60 mV to -120 mV then applying a slow ramp to +60 mV, obtained under standard conditions. Dotted line represents 0 pA/pF.

	V_{mem} (mV)	Cp (pF)	I (-120mV) (pA/pF)	I (+60mV) (pA/pF)	IR (MΩ)	SG (ns/pF)
Glass+PDL	-36.6 ± 2.5	51.6 ± 5.6	-3.8 ± 0.8	32.1 ± 5.1	773.5 ± 89.7	0.01 ± 0.02
OCST+PDL	-26.7 ± 1.7**	47.4 ± 8.4	-8.2 ± 1.6*	35.3 ± 5.2	411.3 ± 65.8**	0.03 ± 0.01**

Table 14: Electrophysiological properties of astrocytes on PDL-coated O-CSTs.
Cp, membrane capacitance; V_{mem}, resting membrane potential; SG, mean specific conductance; IR, input resistance; I, current density. (n=12 for Glass+PDL and n=14 for astrocytes seeded on O-CST+PDL. * $p<0.05$, **$p<0.01$, one-way ANOVA)

A comparative analysis of these whole-cell patch-clamp experiments revealed that cells seeded on the channel of the O-CST displayed a more depolarized resting membrane potential (-26.7 $\pm$ 1.7 mV), a lower input resistance and higher specific conductance in comparison to PDL-seeded cells. No statistical difference could be reported in the maximum outward current density, whereas the inward current density was about two-fold increased in astrocytes seeded on O-CST+PDL. These differences in the electrophysiological properties might suggest that different materials on the surface of the O-CST together enable the differentiation of astroglial cells thereby altering their inward conductance.

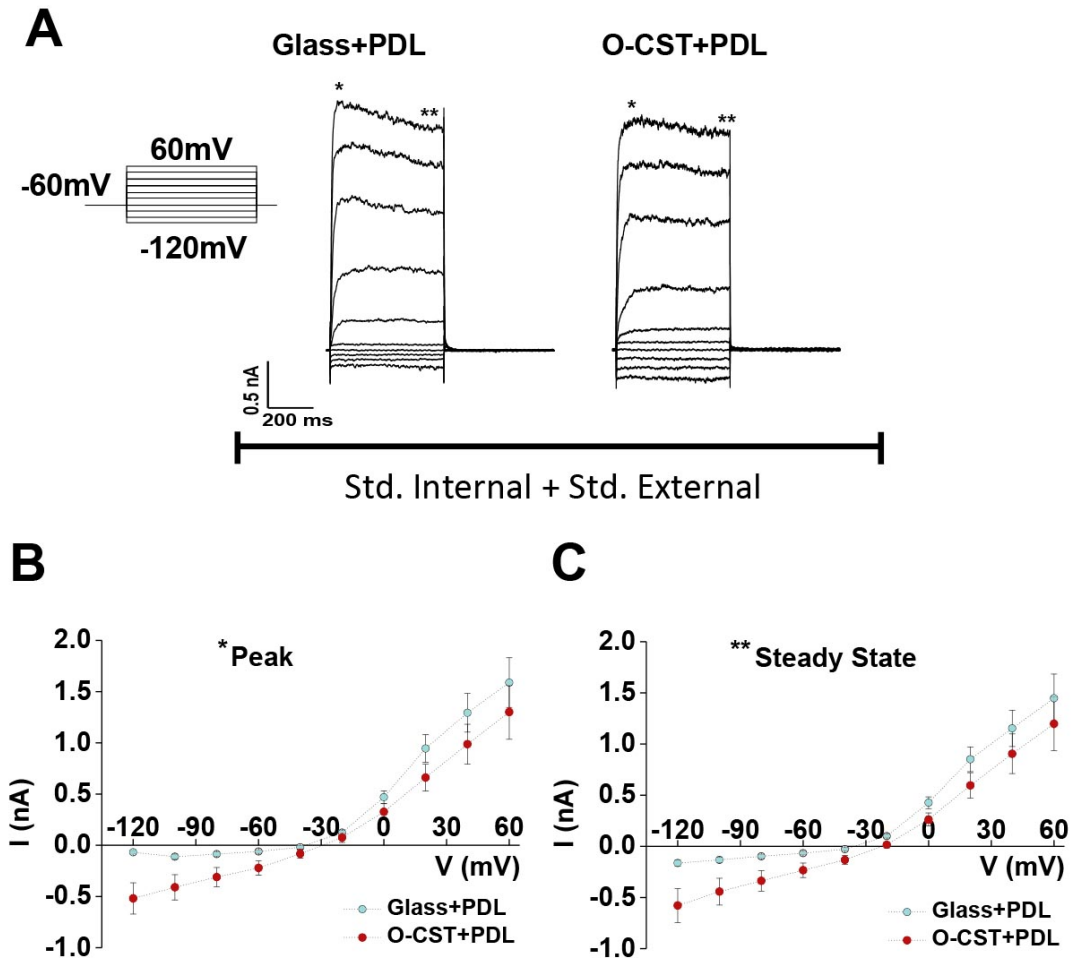

Figure 40: (A) Representative current traces evoked in astrocytes seeded on Glass+PDL and O-CST+PDL with a family of voltage steps from V_h of -60 mV, from -120 to 60 mV in 20 mV increments as depicted by the inset. Asterisks mark peak (*) and steady state (**).
(B-C) I/V plots: Mean current recorded at peak and steady state in astrocytes plated on Glass+PDL (blue circles) and O-CST+PDL (red circles). A statistical difference can be reported for peak and steady state at negative voltages (n=15 for Glass+PDL and n=13 for P13+PDL, $p<0.01$ one-way ANOVA).

Next the voltage dependence of the conductance of O-CST seeded cells was investigated and astrocytes therefor stimulated with 500 ms voltage steps (V_h=-60 mV) from -120 mV to +60 mV in increments of 20 mV (see inset in figure 40A). Representative current traces of astrocytes plated on Glass+PDL and O-CST+PDL are shown in figure 40A. A comparative analysis obtained by an I/V plot of maximal current density mean values, recorded for each voltage step, revealed a voltage-dependent profile of whole-cell peak (*, figure 40B) and steady state (**, figure 40C) current of astrocytes plated on O-CST+PDL and Glass+PDL samples with statistical differences in the whole-cell current evoked at negative voltages.

We next asked, what ion(s) were involved in this increased inward current. To this end, we replaced K^+ and Na^+ in the intracellular solution fully with cesium and used an bath saline without K^+ ($o[K^+]_{out}$). The obtained resulting current profile

(figure 41A, B) and the astrocytic current reversal potential (figure 41C, D) indicate the occurance of a Cl^--conductance [194].

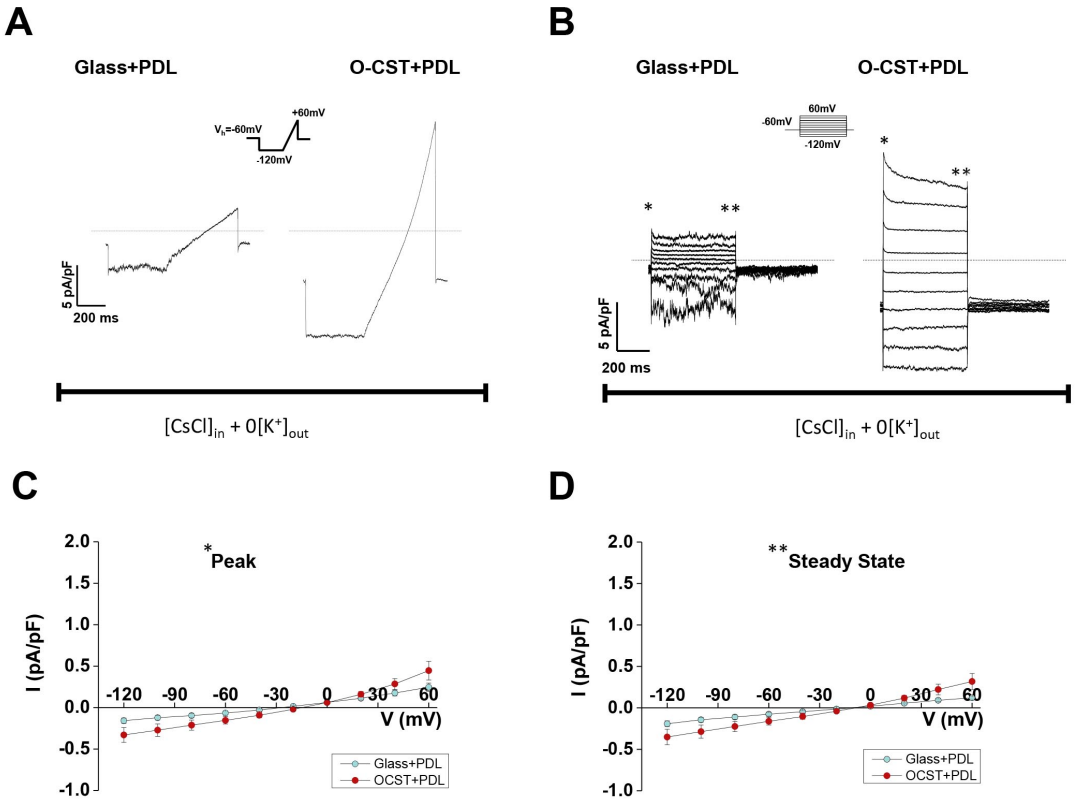

Figure 41: Patch-clamp experiments on broken O-CSTs with Cs-containing internal standard solution and K^+-free bath saline. (A) Representative current traces evoked in astrocytes seeded on Glass+PDL and O-CST+PDL with a ramp protocol as displayed by the inset. (B) Representative step current traces, evoked by a voltage step stimulation as displayed by the inset. (n=10 for Glass+PDL and n=6 for O-CST+PDL, $p<0.001$, one-way Anova).

5.2.2 *Modulation of astrocytic whole-cell currents by the O-CST*

As shown before, the O-CST is capable to enable depolarization and hyperpolarization of the DRG neuron membrane potential [13]. To investigate if the electric field spanned by the O-CST is also modulating the ionic conductance of astroglial cells, single-cell patch-clamp experiments on cells seeded on top of the O-CST channel were performed. A schematic representation of the experimental configuration is shown in figure 42A.

In standard intracellular and extracellular saline, cells were voltage clamped at a holding potential of -60 mV and, after stepping to -120 mV for 400 ms, a slow ramp (180 mV/500 ms) from -120 to 60 mV (upper inset in figure 42B, asterisk is highlighting the ramp part of the stimulation protocol) was applied to evoke whole-cell currents. We continuously recorded ramp-current traces obtained by applying this voltage-clamp protocol while operating the O-CST in accumulation mode by biasing the gate electrode from 0V to 1V (V_{GS}=0-1V) and keeping the drain electrode at 0V (V_{DS}=0V). In this experimental condition, the device operation in the saline solution does not exceed 1V in order to avoid detrimental Faradaic currents causing redox reactions at the electrodes[195].

During the experiments, the Ag/AgCl reference electrode of the patch-clamp set-up was immersed into the bath saline and connected to the source electrode of the O-CST, thereby double-serving as the grounded reference for all bias stimulation protocols.

The typical ramp current profile observed is shown in the I/V plot in figure 42B. The time course analysis of the percentage change in current density was sampled and analyzed every 15 seconds and is reported in figure 42C. We observed an increase in the inward current density during device operation over time, which also persisted 30s after the end of stimulation (figure 42B, purple trace, figure 42C white circles). In correspondence with the maximal stimulation provided by the O-CST when V_{GS}=1V, a peak in the inward current density can be observed at 85s (figure 42B, orange circle). In comparison, there was only a negligible change in the maximum outward current density (figure 42C, black circles) during and after operating the O-CST.

With intracellular and extracellular standard saline condition these effects were accompanied by a positive shift in the astrocytic reversal potential (see also lower inset in figure 42B) of 6.1 $\pm$ 2.3.mV, 30 s after stimulation with the O-CST. This shift was confirmed by a continuous current-clamp recording performed to monitor the membrane potential during the O-CST stimulation (figure 42D). These results demonstrate, that stimulation provided by the O-CST modulates astrocytic inward conductance.

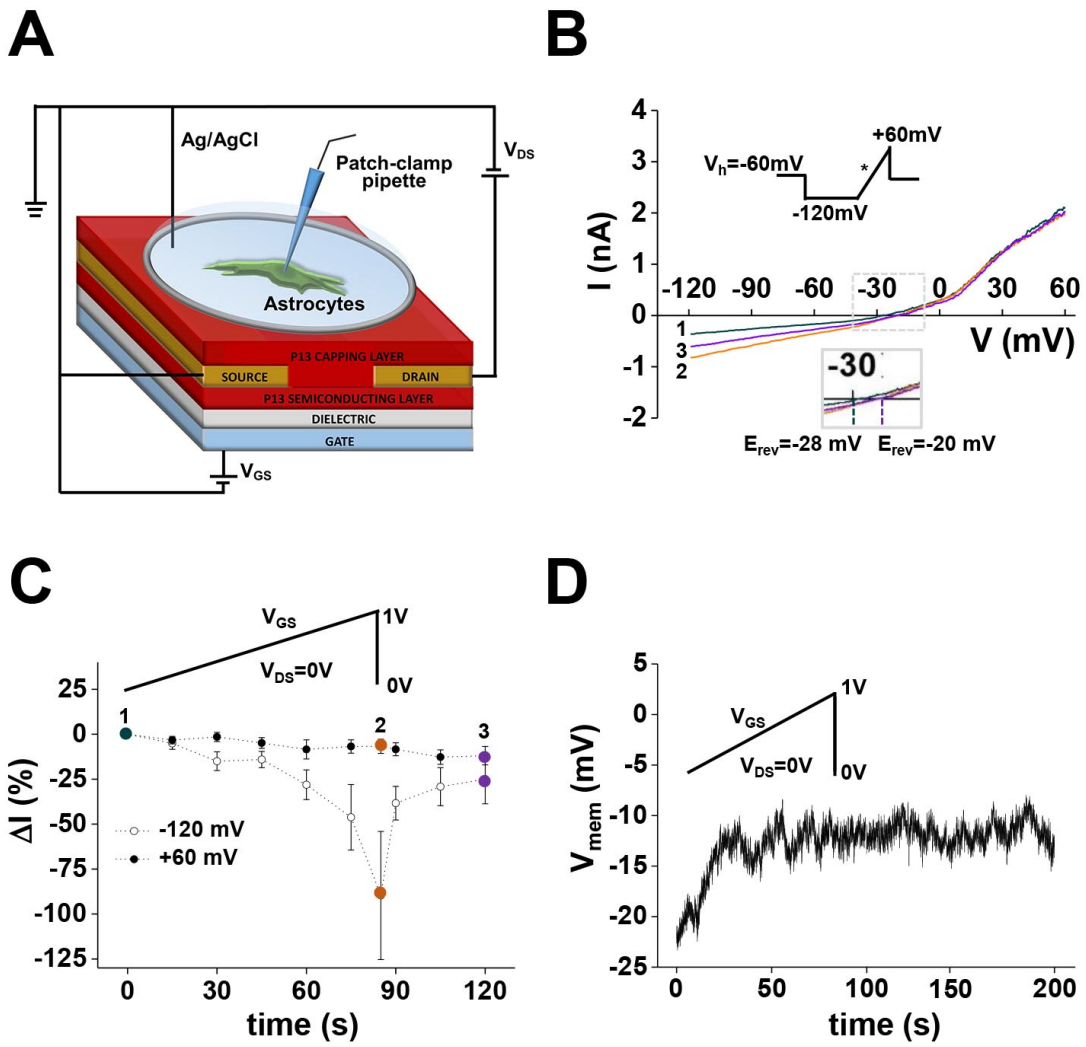

Figure 42: (A) Scheme of patch-clamp experiments on cells plated on O-CST device. (B) Ramp current traces, plotted as a function of the applied voltage, evoked in response to a voltage ramp protocol from -120 mV to +60 mV. Complete stimulation protocol is depicted by the inset, the voltage ramp is highlighted by the asterisk. While running the voltage-clamp ramp protocol, cells were stimulated operating the device with a transfer protocol with V_{GS}=0-1V and V_{DS}=0V. Reported traces corresponds to typical current traces recorded before (green trace, 1), at the end of device operation (after 85s of device operation, orange trace 2) and 30 s after switch-off of the O-CST (purple trace, 3). The zoom of the x-axis shows the shift in the reversal potential observed upon and after stimulation of the cell with the O-CST. (C) Time course of averaged percentage change in ramp current values with respect to the control, calculated at -120 mV and +60 mV. The time points marked with 1 (green circle), 2 (orange circle) and 3 (purple circle) corresponds to the time points marked with the same number and colors in panel B (n=11). (D) Continuous current-clamp recording of the resting membrane potential of an astrocyte recorded upon and after stimulation course with transfer protocol in external and internal standard saline.

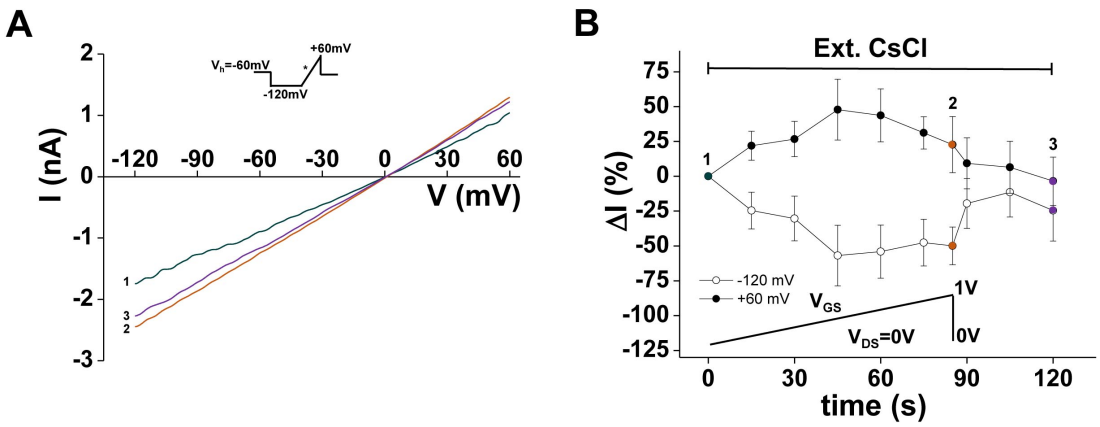

Figure 43: (A) I/V plot of ramp current traces measured before (1, green), after 60s of device operation (2, orange) and 35 s after operating the O-CST (3, purple) recorded in internal standard Cs-Gluconate saline and external standard solution containing Cesium. Ramp traces were recorded as depicted by the inset. (B) Percentage change of current density over time at -120 mV and +60 mV recorded upon and after stimulation course of the O-CST (V_{GS}=0-1, V_{DS}=0) compared to control (before stimulation, 1, green) recorded in external and internal standard solution containing Cesium (n=7). The points at 0s (1, green circle), 85s (2, orange circle) and 120s (3, purple circle) correspond with the ramp current traces shown in (A).

To study this O-CST-activated current in further depth K^+ and Na^+ in the intra- and extracellular solutions were replaced with cesium to avoid the occurance of these currents and intracellular Cl^- was partially replaced by cell impermeable gluconate. Ramp current traces were recorded as before within this particular ionic condition and are reported in figure 43A. Before O-CST stimulation a value of the reversal potential of the control current towards 0 mV was recorded which is consistent with the occurrence of a cationic current (figure 43A).

Moreover a dramatic change in the maximum outward current density due to Cs^+ blockage of K_{dr} mediated outward currents was observed (figure 43B) [196]. The membrane potential was evaluated during the external stimulation of the O-CST and only a negligible shift in the membrane potential could be observed, giving evidence that the observed activated inward current is mediated by a cation which is largely active already at resting state. Collectively these findings indicate the possible contribution of Ca^{2+} channels or another non-selective cation channel.

To this end, Ruthenium Red (RR), a potent inhibitor for a broad range of Ca^{2+} channels, including the TRPV family, TRPA1, several ryanodin-receptors and Ca^{2+}-binding proteins like calmodulin, was applied [197, 198].

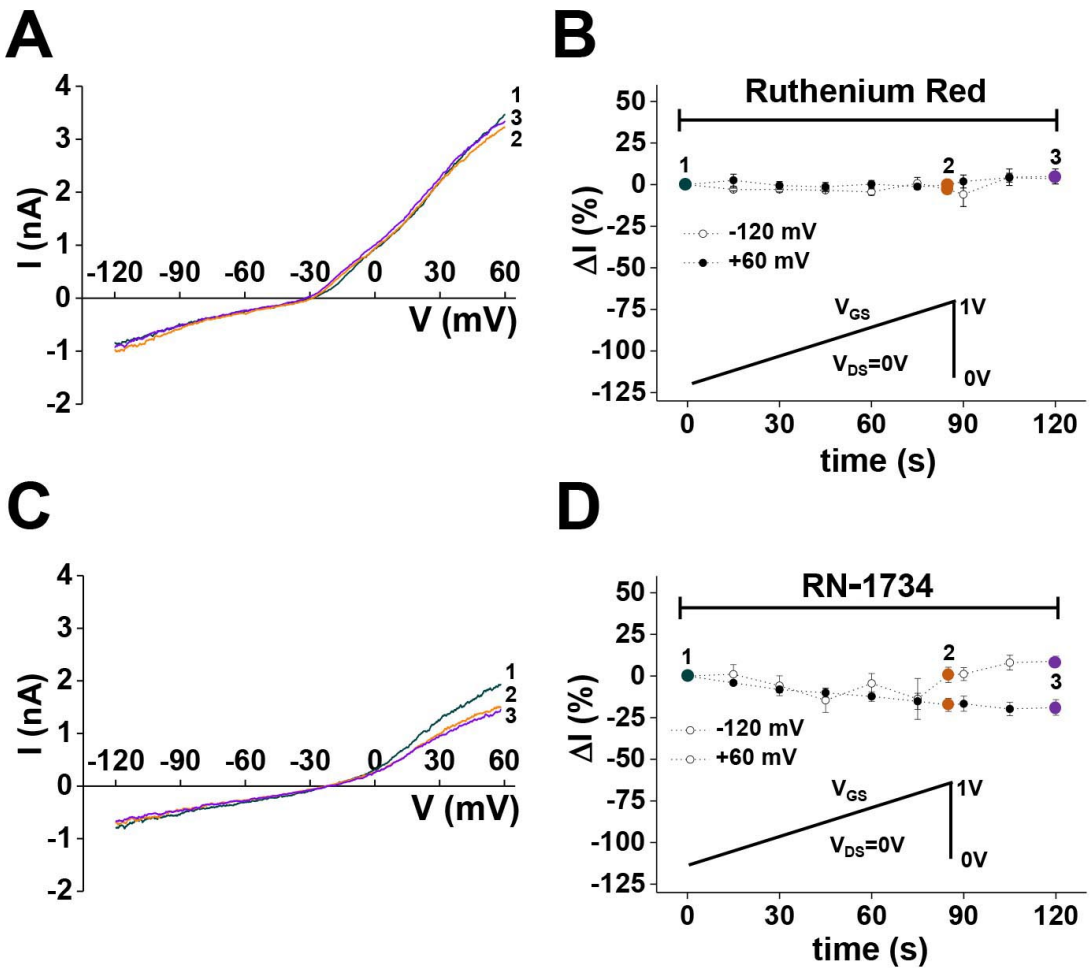

Figure 44: (A) Ramp current traces, were recorded as described above in presence of Ruthenium Red that was added before O-CST stimulation to the external standard saline to a final concentration of 10 µM. (B) Corresponding time course of averaged percentage change in current density at -120 mV and +60 mV recorded upon and after stimulation with O-CST in presence of 10 µM of RR. The time points marked with 1, green circle; 2, orange circle and 3, purple circle, correspond to the time points marked with the same number and colors in panel A (n=5). (C) Ramp current traces recorded as described above in presence of 10 µM RN-1734, applied to the external standard saline before recording. (D) Corresponding time course of averaged percentage change in current density at -120 mV and +60 mV recorded upon and after stimulation with O-CST in presence of 10 µM RN-1734. The time points marked with 1, green circle; 2, orange circle and 3, purple circle, correspond with the time points marked with the same number and colors in panel C (n=8).

Ramp current traces were recorded in internal and external standard saline and 10µM RR was applied prior to stimulation with O-CST (figure 44A). In this experimental condition, we couldn't observe either a change in the maximum inward (figure 44B, white circles) or outward (figure 44B, black circles) current density during and after stimulation with the O-CST. Also no shift in the reversal potential was found, even at the maximum voltage (V_{GS}=1V) applied to the O-CST. These data suggested that the observed current changes due to O-CST stimulation are mediated by ion channels that are inhibited by RR.

Among the different channels blocked by Ruthenium Red, TRPV4 as a non-selective cation channel has been shown to be highly abundant in astrocytes *in vitro* and in astrocytic endfeet in situ [188]. TRPV4 displays a high permeability for Ca^{2+} and activated by a variety of stimuli as described in 2.2.2. So we tested first a possible engagement of TRPV4 in the obtained response, the TRPV4-specific blocker RN-1734 (10 µM, [71]) was applied and ramp current traces recorded while operating the O-CST as described above (figure 44C). In this experimental condition, no change could be found in the inward current density before, during and after O-CST operation (figure 44D, white circles). Instead, a decrease in the outward current density was observed after O-CST operation (figure 44D, black circles). The abolition of the increase in the inward current density subsequent to O-CST provided stimulation by the application of the TRPV4-specific antagonist RN-1734 substantiates a crucial contribution of TRPV4 channels to the observed change in the inward current density.

The initial raise of $[Ca^{2+}]_i$ and the following sustained phase after stimulation under standard conditions match closely with TRPV4-mediated Ca^{2+} currents [188] as well as the change in the current profile due to the use of RR and RN-1734. Off note, during standard conditions, we observed an instability of Gigaohm seals, hinting a change of the cell volume. Monitoring of the cell capacitance during stimulation with the O-CST revealed an increase in the capacitance of 1.3 ± 0.5 pF, indicating a slight cell swelling. This behavior could not be observed during the use of RR and RN-1734, further underpinning the supposition of a TRPV4 involvement since it is well known that this channel can be activated by cell swelling. Thereby it is plausible to assume that the electric field provided by the O-CST is interacting with the lipid membrane of the cells inducing a swelling which in turn activates TRPV4 [66].

In figure 44, it can be seen that Ruthenium Red is fully blocking the change of current density evoked by device operation. The reason is its rather unspecific blocking of a broad range of channels. After getting a first strong indication of the involvement of TRPV4 by the use of RN-1734, we next asked whether there might be also other ions and their channels involved in the obtained response.

To this end, we fully replaced K^+ and Na^+ in the intra- and extracellular solutions with cesium to again avoid the occurrence of these currents and intracellular Cl^- was partially replaced by cell impermeable gluconate. While recording ramp current traces and stimulating the cell with the O-CST as before, the cells were perfused with the Cs- bath solution containing 10 µM RN-1734 (see figure 45A) to block TRPV4, Brilliant Blue to examine a potential contribution of the P2X7-pathway and in another experiment 30 µM HC030031 to block TRPA1 (see figure 45C). We found also in this ionic condition that as before, with RN-1734 the change in the inward current density can be abolished. Also no shift in the reversial potential could be observed. These findings underline one more time the crucial contribution of the TRPV4 channel to the obtained increase in the inward current density and the origin of the obtained inward current is Ca^{2+}.

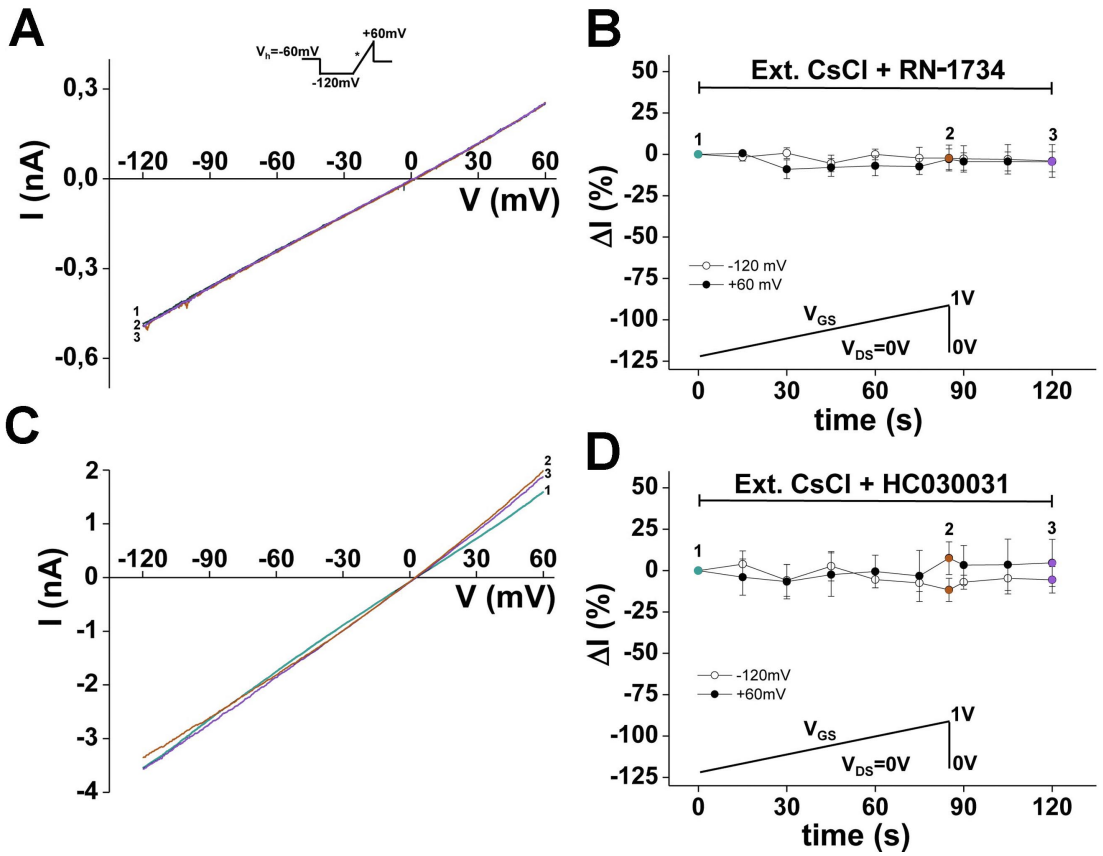

Figure 45: (A) Ramp current traces, recorded as described above while perfusing the cells with Cs-bath saline containing 10 µM RN-1734 during O-CST stimulation. (B) Corresponding time course of averaged percentage change in current density at -120 mV and +60 mV recorded upon and after stimulation with O-CST in presence of 10 µM of RN-1734 in Cs-bath saline. The time points marked with 1, green circle; 2, orange circle and 3, purple circle, correspond to the time points marked with the same number and colors in panel A (n=5). (C) Ramp current traces, recorded as described above while perfusing the cells with Cs-bath saline containing 30 µM HC030031 during O-CST stimulation. (D) Corresponding time course of averaged percentage change in current density at -120 mV and +60 mV recorded upon and after stimulation with O-CST in presence of 30 µM HC030031. The time points marked with 1, green circle; 2, orange circle and 3, purple circle, correspond with the time points marked with the same number and colors in panel C (n=5).

To rule out a Ca^{2+}-entry through the purinergic receptor P2X7, cells were perfused with Cs-bath saline containing 10 µM l and 1 µM of Brilliant Blue. At both concentrations of this blocker, cells showed almost immediately signs of blebbing, therefor no results can be shown of this experimental condition as the combination of Cs-bath saline and Brilliant Blue must be considered as cell toxic.

Surprisingly a rather similar picture can be found when perfusing the cell with the TRPA1-specific blocker HC030031 in Cs-bath saline (see figure 45C). Only a very small increase in the inward and outward current density due to stimulation with the O-CST can be found and no shift in the reversial potential. Therefor it must be taken into account that also TRPA1 could play a role in the obtained increase in inward current density under standard conditions. TRPA1 could hereby be directly activated itself by the spanning of the electric field due to device operation. But also a

secondary onset via a stretch activated pathway due to the slight cell swelling might have been thinkable.

5.2.3 *The role of O-CST architecture and device integrity*

In order to investigate the role of the specific O-CST device architecture in the observed increase of inward current density, the impact of the O-CST structure integrity and device working functionality on the astrocytic response was investigated. Figure 46A shows the leakage gate current of a working O-CST (green circles) and of an O-CST with a leakage in the dielectric (red squares), recorded upon the stimulation transfer protocol by biasing the gate electrode from 0V to 1V (V_{GS} = 0 - 1V) and keeping the drain electrode at 0V (V_{DS} = 0V). Respectively, the working O-CST device has a maximum leakage current of 2 nA whereas the device with leaking dielectric shows a thousand fold higher leakage current of about 2 µA. A device compromised in this way is not able to build up an electric field in the channel and thereby not providing sufficient stimulation to the cells.

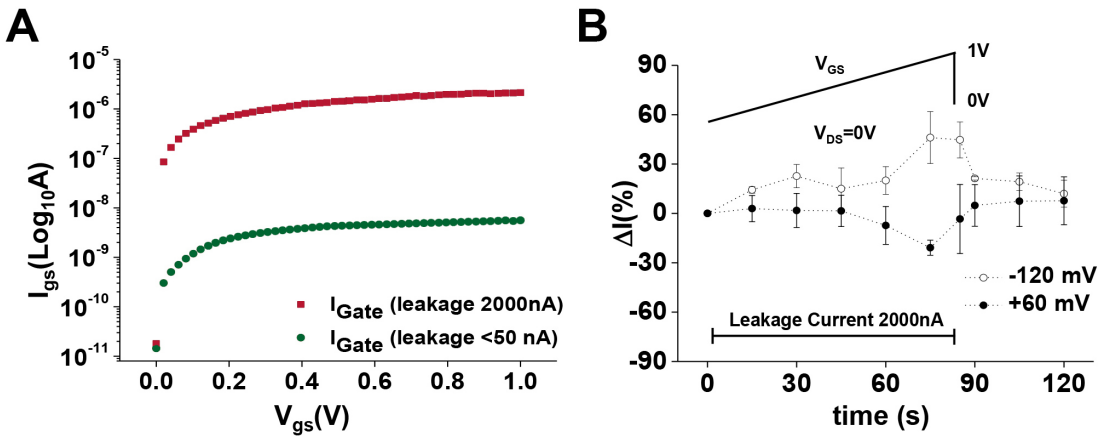

Figure 46: (A) I/V curve representing an O-CST with low gate leakage current (green trace) in comparison to a device with a high leakage of 2 µA (red trace). (B) Time course of percentage change in current density at -120 mV and +60 mV upon and after O-CST stimulation recorded on cells plated O-CSTs with a high gate leakage current of 2 µA (n=3). Note that the leakage current is not changing over time.

Again we performed patch-clamp experiments, continuously recording ramp traces with the same settings as described in figure 42B. The corrupted O-CST was operated in accumulation mode where V_{GS} was spanned from 0 to 1 V within a duration of 85 s, while V_{DS} was kept at 0V (see stimulation protocol in figure 46B). Figure 46B shows the changes in inward and outward current density of astrocytes seeded on an O-CST with a gate leakage-current of 2 µA. With the corrupted device, only a decreased percentage change of the maximum current density during and after stimulation with the O-CST with respect to a working device could be observed. This finding shows, that it is indeed the stimulation by the electric field built up by a working O-CST device that evokes the prior observed changes in the inward current density of astrocytes seeded on the channel as described in 5.2.2.

5.3 CONCLUSIONS

By the means of patch-clamp experiments, it could be demonstrated that the O-CST is capable of stimulating astrocytes seeded on top of the channel and thereby increasing astrocytic inward current. By the use of specific blockers, this response could be attributed to an influx of Ca^{2+} through mainly two members of the TRP-family: TRPV4 and TRPA1. But also the integrity and function of the O-CST was found to play a major role.

The TRPV4 channel, as a member of the vannilloid subfamily of TRP-channels, is activated by a broad variety of chemical and physical stimuli and displays a large permeability for Ca^{2+} over other monovalent cations [199]. In the brain, TRPV4 was shown by immunogold-staining to be highly expressed in astrocytic endfeet *in situ*, which are also enriched in AQP4. Astrocytic endfeed are abutting the blood capillaries and the pial surface [188]. TRPV4 has been discussed as an osmosensor, for it has been shown to be involved in osmoregulation [200, 201]. By interacting with AQP4, TRPV4 has been shown to play a role in cell volume regulation, for a manipulation of the TRPV4 and AQP4 expression led to changes in the regulatory volume decrease following a hypotonic challenge [202]. In adult rats, TRPV4 has been shown to be involved ischemia-induced Ca^{2+}-entry and been suspected to play a role in the pathogenic mechanism leading for example to cell swelling [203].

TRPA1 as the sole member of the anikyrin-subfamily in mammals is also a promiscuous channel when it comes to the stimuli activating it. It was found to be predominantly expressed in sensory neurons [78], for example co-expressed with the capsaicin receptor TRPV1 in DRG-neurons, where it is thought to be an irritant sensor. TRPA1, was described as a transducer of irritant stimuli into nociceptor activity, thereby playing a role in pain and acute inflammation [204]. TRPA1 was also debated to be a mechanosenor necessary in auditory transduction, because hair cells of the inner ear were found to express TRPA1 on the RNA and protein level, even though it couldn't be confirmed in knock-out mice studies [205]. In astrocytes, it was reported to be regulator of astrocytic basal calcium levels [76].

Even though the O-CST can be seen as a stepstone to create novel tools for understanding the complex background in astrocytic Ca^{2+}-signalling, there are still questions left open for follow-up studies. Also the current setup of the O-CST leaves room for improvement. As discussed above, P13, the capping layer of the O-CST is a material that is highly hydrophobic, thereby requires still treatment with PDL to enable cell adhesion. The question that arises directly from this fact is: would the astrocytic response be comparable, yet even stronger with the use of an O-CST? Seeding cells on the O-CST for patch-clamp experiments revealed that cell adhesion took place mostly outside the channel, even with coating of PDL. Without additional treatment, almost no cells were found on the channel, so this experimental scenario was not feasible. To overcome this major issue of the O-CST, new materials were investigated. In this context the group of Valentina Benfenati (CNR-ISOF, Bologna) characterized a new perylene diimide material bearing lysine end substituents (PDI-Lys, see [161]). The introduced lysine ends enabled water processability of the perylene diimide derivative. Furthermore, the ionic nature of the lysine framework enhanced the overall hydrophilicity of the final material, overcoming one of the major disadvantages of P13 in terms of cell adhesion: its high hydrophobicity. The lysine functionalization of

PDI promoted good cell adhesion of neural cells and a high in vitro biocompatibility and differentiation of the neural cells while skipping the step of additional coating with Poly-Lysine. Taken together with the good filmability and electrical transport of PDI-Lys, this material could be a suitable candidate as active layer in organic electronics for neural interfacing. Also because the response of astrocytes to low and high frequency stimulation was shown in 2015 by two different groups [206, 207], an O-CST with a capping layer that improves cell adhesion and reduces the cleft between the organic interface and the cells, may serve as a simple tool to finally help unravel the role of TRPV4 and TRPA1 channels, their interplay and their specific functions in CNS physiology and pathophysiology.

6

PROJECT SUMMARY AND OUTLOOK

The first part of the results obtained during my PhD show that the novel material T4-Lys, a quaterthiophene bearing lysine-ends, is biocompatible with DRG neurons and enables cell adhesion and promotes the outgrowth of neurites without the need of any further coating of the interface. The alteration of the electrophysiological properties and the enhanced firing rate indicate that T4Lys enables functional differentiation of DRG primary neurons. These pieces of evidence indicate that T4Lys is a suitable organic interface for DRG primary neurons.

The second part of the results were aimed to test the suitability of the O-CST, an organic field effect transistor that had been shown to work as both a cell stimulating and cell response sensing device with primary DRG neurons, as an interface with primary astroglial cells. We could show that the organic field effect transistor structure whose P13 capping layer was introduced as a biocompatible substrate to be interfaced with DRG neurons, was also a biocompatible with astroglial cells. The device treated with PDL as an additional coating was able to promote astrocytic adhesion and growth. The astrocytic electrophysiological properties were found to be preserved. We were able to stimulate astrocytes with these O-CST devices in accumulation mode (V_{GS} = 0-1V and V_{DS} = 0V, transfer stimulation protocol) and could determine by patch-clamp experiments that the provided stimulation addresses the astrocytic whole-cell inward current. By the use of different blockers (Ruthenium Red, RN-1734 and HC030031) and Cs-bath saline during stimulation, we found that the ion responsible for the response was Ca^{2+} and we could attribute the obtained modulation of the inward current to the TRPV4 and TRPA1 channels. When stimulating the cells with the O-CST while parallel reading out the astrocytic calcium response, we found that the stimulation by the O-CST (V_{GS} = 0-1V and V_{DS} = 0V) evokes an increase in intracellular Ca^{2+}, which is perfectly in line with the findings of the patch-clamp studies, where we found an increased inward flux of Ca^{2+}. Finally, the dependence of astrocytic response on the O-CST device architecture and functionality could be demonstrated, where a lack of the proper localized field effect did not lead to the response obtained with a fully functional O-CST.

The research and the obtained results during my PhD-studies opened the door for several interesting follow-up studies. After testing the O-CST separately on DRG neurons and cortical astrocytes, a next step might be to test neurons and astrocytes together, also in regard of their interplay upon stimulation. Furthermore with the introduction of T4Lys and PDILys, in the near future the additional coating of the O-CST can probably be skipped by integrating these novel materials into the device. This might help to overcome the major issue of P13's hydrophobicity and thereby making the O-CST an important stepping stone on the way of bridging the brain to the world.

BIBLIOGRAPHY

[1] A. D. Wade, A. J. Nelson, and G. J. Garvin, "A synthetic radiological study of brain treatment in ancient egyptian mummies.," *Homo : internationale Zeitschrift für die vergleichende Forschung am Menschen*, vol. 62, no. 4, pp. 248–269, 2011.

[2] T. Breitenfeld, M. J. Jurasic, and D. Breitenfeld, "Hippocrates: the forefather of neurology.," *Neurological sciences : official journal of the Italian Neurological Society and of the Italian Society of Clinical Neurophysiology*, vol. 35, no. 9, pp. 1349–1352, 2014.

[3] E. Crivellato and D. Ribatti, "Soul, mind, brain: Greek philosophy and the birth of neuroscience.," *Brain research bulletin*, vol. 71, no. 4, pp. 327–336, 2007.

[4] J. Rocca, "Galen and the ventricular system," *Journal of the History of the Neurosciences*, vol. 6, no. 3, pp. 227–239, 1997.

[5] A. P. Alivisatos, A. M. Andrews, E. S. Boyden, M. Chun, G. M. Church, K. Deisseroth, J. P. Donoghue, S. E. Fraser, J. Lippincott-Schwartz, L. L. Looger, S. Masmanidis, P. L. McEuen, A. V. Nurmikko, H. Park, D. S. Peterka, C. Reid, M. L. Roukes, A. Scherer, M. Schnitzer, T. J. Sejnowski, K. L. Shepard, D. Tsao, G. Turrigiano, P. S. Weiss, C. Xu, R. Yuste, and X. Zhuang, "Nanotools for neuroscience and brain activity mapping.," *ACS nano*, vol. 7, no. 3, pp. 1850–1866, 2013.

[6] WHO, "Mental disorders affect one in four people, howpublished = "http://www.who.int/whr/2001/media_centre/press_release/en/", year = 2001, note = "[online; accessed 15-january-2016]"."

[7] WHO, "2015 Alzheimer's Disease Facts and Figures, howpublished = "http://www.alz.org/facts/downloads/facts_figures_2015.pdf", year = 2015, note = "[online; accessed 15-january-2016]"."

[8] WHO, "NEUROLOGICAL DISORDERS public health challenges, howpublished = "http://www.who.int/mental_health/neurology/neurological_disorders_report_web.pdf", year = 2006, note = "[online; accessed 15-january-2016]"."

[9] S. Löffler, B. Libberton, and A. Richter-Dahlfors, "Organic bioelectronic tools for biomedical applications," *Electronics*, vol. 4, no. 4, p. 879, 2015.

[10] H. Sorribas, D. Braun, L. Leder, P. Sonderegger, and L. Tiefenauer, "Adhesion proteins for a tight neuron-electrode contact," *Journal of Neuroscience Methods*, vol. 104, no. 2, pp. 133–141, 2001.

[11] P. Fromherz, A. Offenhäusser, T. Vetter, and J. Weis, "A neuron-silicon junction: a retzius cell of the leech on an insulated-gate field-effect transistor.," *Science*, vol. 252, no. 5010, pp. 1290–1293, 1991.

[12] M. Grattarola, M. Bove, S. Martinoia, and G. Massobrio, "Silicon neuron simulation with spice: tool for neurobiology and neural networks.," *Medical & biological engineering & computing*, vol. 33, no. 4, pp. 533–536, 1995.

[13] V. Benfenati, S. Toffanin, S. Bonetti, G. Turatti, A. Pistone, M. Chiappalone, A. Sagnella, A. Stefani, G. Generali, G. Ruani, D. Saguatti, R. Zamboni, and M. Muccini, "A transparent organic transistor structure for bidirectional stimulation and recording of primary neurons," *Nature Materials*, vol. 12, no. 7, pp. 672–680, 2013.

[14] S. Toffanin, V. Benfenati, A. Pistone, S. Bonetti, W. Koopman, T. Posati, A. Sagnella, M. Natali, R. Zamboni, G. Ruani, and M. Muccini, "N-type perylene-based organic semiconductors for functional neural interfacing," *Journal of Materials Chemistry B*, vol. 1, no. 31, pp. 3850–3859, 2013.

[15] O. Project, "www.olimpiaproject.eu, howpublished = "http://www.olimpiaproject.eu/", year = 2013, note = "online; accessed 25-march-2017"."

[16] A. L. Hodgkin, A. F. Huxley, and B. Katz, "Measurement of current-voltage relations in the membrane of the giant axon of loligo.," *The Journal of physiology*, vol. 116, pp. 424–448, Apr 1952.

[17] A. L. Hodgkin and R. D. Keynes, "The potassium permeability of a giant nerve fibre," *The Journal of Physiology*, vol. 128, no. 1, pp. 61–88, 1955.

[18] E. Neher and B. Sakmann, "Single-channel currents recorded from membrane of denervated frog muscle fibres.," *Nature*, vol. 260, Apr 1976.

[19] J. G. Nicholls, A. R. Martin, P. A. Fuchs, D. A. Brown, M. E. Diamond, and D. A. Weisblat, *Ionic basis of the resting potential*, pp. 99–111. Sinauer Associates, Inc., 2012.

[20] A. L. Hodgkin and B. Katz, "The effect of sodium ions on the electrical activity of giant axon of the squid.," *The Journal of physiology*, vol. 108, no. 1, pp. 37–77, 1949.

[21] D. E. Goldman, "Potential, impedance, and rectification in membranes.," *The Journal of general physiology*, vol. 27, pp. 37–60, Sep 1943.

[22] L. T. Troland, "The "all or none" law in visual response," *The Journal of the Optical Society of America*, vol. 4, pp. 160–185, May 1920.

[23] H. C. Lai and L. Y. Jan, "The distribution and targeting of neuronal voltage-gated ion channels.," *Nature reviews. Neuroscience*, vol. 7, pp. 548–562, Jul 2006.

[24] W. Commons, "From Wikimedia Commons, the free media repository, howpublished = "https://commons.wikimedia.org/wiki/File:Action_potential_basic_shape.svg", year = 2015, note = "online; accessed 09-september-2016"."

[25] W. Commons, "From Wikimedia Commons, the free media repository, howpublished = "https://commons.wikimedia.org/wiki/File:Action_potential.svg", year = 2007, note = "[online; accessed 09-september-2016]"."

[26] H. Lodish, A. Berk, and S. Zipursky, *The Action Potential and Conduction of Electric Impulses.* W. H. Freeman, 2000.

[27] M. R. Markham, "Electrocyte physiology: 50 years later," *Journal of Experimental Biology*, vol. 216, no. 13, pp. 2451–2458, 2013.

[28] M. E. Spira, Y. Yarom, and D. Zeldes, "Neuronal interactions mediated by neurally evoked changes in the extracellular potassium concentration.," *The Journal of experimental biology*, vol. 112, pp. 179–197, Sep 1984.

[29] X. Wang, T. Takano, and M. Nedergaard, "Astrocytic calcium signaling: mechanism and implications for functional brain imaging," *Methods in Molecular Biology*, vol. 489, pp. 93–109, 2009.

[30] T. A. Fiacco and K. D. McCarthy, "Astrocyte calcium elevations: properties, propagation, and effects on brain signaling," *Glia*, vol. 54, no. 7, pp. 676–690, 2006.

[31] C. Agulhon, J. Petravicz, A. B. McMullen, E. J. Sweger, S. K. Minton, S. R. Taves, K. B. Casper, T. A. Fiacco, and K. D. McCarthy, "What is the role of astrocyte calcium in neurophysiology?," *Neuron*, vol. 59, no. 6, pp. 932–946, 2008.

[32] S. W. Kuffler, "Neuroglial cells: physiological properties and a potassium mediated effect of neuronal activity on the glial membrane potential.," *Proceedings of the Royal Society of London. Series B, Biological sciences*, vol. 168, pp. 1–21, Jun 1967.

[33] B. R. Ransom and S. Goldring, "Ionic determinants of membrane potential of cells presumed to be glia in cerebral cortex of cat.," *Journal of neurophysiology*, vol. 36, pp. 855–868, Sep 1973.

[34] H. Sontheimer, E. Fernandez-Marques, N. Ullrich, C. A. Pappas, and S. G. Waxman, "Astrocyte na+ channels are required for maintenance of na+/k(+)-atpase activity.," *The Journal of neuroscience : the official journal of the Society for Neuroscience*, vol. 14, pp. 2464–2475, May 1994.

[35] B. A. Barres, L. L. Chun, and D. P. Corey, "Ion channels in vertebrate glia.," *Annual review of neuroscience*, vol. 13, pp. 441–474, 1990.

[36] F. W. Tse, D. D. Fraser, S. Duffy, and B. A. MacVicar, "Voltage-activated k+ currents in acutely isolated hippocampal astrocytes.," *The Journal of neuroscience : the official journal of the Society for Neuroscience*, vol. 12, pp. 1781–1788, May 1992.

[37] S. Bevan, P. T. Gray, and J. M. Ritchie, "A calcium-activated cation-selective channel in rat cultured schwann cells.," *Proceedings of the Royal Society of London. Series B, Biological sciences*, vol. 222, pp. 349–355, Sep 1984.

[38] H. Sontheimer and S. G. Waxman, "Ion channels in spinal cord astrocytes in vitro. ii. biophysical and pharmacological analysis of two na+ current types.," *Journal of neurophysiology*, vol. 68, pp. 1001–1011, Oct 1992.

[39] H. Sontheimer, J. A. Black, B. R. Ransom, and S. G. Waxman, "Ion channels in spinal cord astrocytes in vitro. i. transient expression of high levels of na+ and k+ channels.," *Journal of neurophysiology*, vol. 68, pp. 985–1000, Oct 1992.

[40] H. K. Kimelberg, B. A. Macvicar, and H. Sontheimer, "Anion channels in astrocytes: biophysics, pharmacology, and function.," *Glia*, vol. 54, pp. 747–757, Nov 2006.

[41] H. Sontheimer, "Astrocytes, as well as neurons, express a diversity of ion channels.," *Canadian journal of physiology and pharmacology*, vol. 70 Suppl, pp. S223–S238, 1992.

[42] D. Rossi and A. Volterra, "Astrocytic dysfunction: insights on the role in neurodegeneration.," *Brain research bulletin*, vol. 80, no. 4-5, pp. 224–232, 2009.

[43] A. Verkhratsky, J. J. Rodriguez, and V. Parpura, "Calcium signalling in astroglia," *Molecular and Cellular Endocrinology*, vol. 353, no. 1-2, pp. 45–56, 2012.

[44] D. A. Coulter and T. Eid, "Astrocytic regulation of glutamate homeostasis in epilepsy.," *Glia*, vol. 60, pp. 1215–1226, Aug 2012.

[45] D. Coulter and C. Steinhauser, "Role of astrocytes in epilepsy," *Cold Spring Harbor Perspectives in Medicine*, vol. 5, no. 3, 2015.

[46] J. A. Hubbard, M. S. Hsu, M. M. Seldin, and D. K. Binder, "Expression of the astrocyte water channel aquaporin-4 in the mouse brain.," *ASN neuro*, vol. 7, Sep/Oct 2015.

[47] M. Xiao and G. Hu, "Involvement of aquaporin 4 in astrocyte function and neuropsychiatric disorders.," *CNS neuroscience & therapeutics*, vol. 20, pp. 385–390, May 2014.

[48] N. J. Abbott, L. Rönnbäck, and E. Hansson, "Astrocyte-endothelial interactions at the blood-brain barrier.," *Nature reviews. Neuroscience*, vol. 7, pp. 41–53, Jan 2006.

[49] R. Cabezas, M. Avila, J. Gonzalez, R. S. El-Bachá, E. Báez, L. M. García-Segura, J. C. Jurado Coronel, F. Capani, G. P. Cardona-Gomez, and G. E. Barreto, "Astrocytic modulation of blood brain barrier: perspectives on parkinson's disease.," *Frontiers in cellular neuroscience*, vol. 8, p. 211, Aug 2014.

[50] J. I. Alvarez, T. Katayama, and A. Prat, "Glial influence on the blood brain barrier.," *Glia*, vol. 61, pp. 1939–1958, Dec 2013.

[51] A. Falkowska, I. Gutowska, M. Goschorska, P. Nowacki, D. Chlubek, and I. Baranowska-Bosiacka, "Energy metabolism of the brain, including the cooperation between astrocytes and neurons, especially in the context of glycogen metabolism.," *International journal of molecular sciences*, vol. 16, pp. 25959–25981, Oct 2015.

[52] A. M. Brown and B. R. Ransom, "Astrocyte glycogen and brain energy metabolism.," *Glia*, vol. 55, pp. 1263–1271, Sep 2007.

[53] E. Cekanaviciute and M. S. Buckwalter, "Astrocytes: Integrative regulators of neuroinflammation in stroke and other neurological diseases.," *Neurotherapeutics : the journal of the American Society for Experimental NeuroTherapeutics*, vol. 13, pp. 685–701, Oct 2016.

[54] J. E. Burda, A. M. Bernstein, and M. V. Sofroniew, "Astrocyte roles in traumatic brain injury.," *Experimental neurology*, vol. 275 Pt 3, pp. 305–315, Jan 2016.

[55] O. K. Bitzer-Quintero and I. González-Burgos, "Immune system in the brain: a modulatory role on dendritic spine morphophysiology?," *Neural plasticity*, vol. 2012, p. 348642, Apr 2012.

[56] Y. Dong and E. N. Benveniste, "Immune function of astrocytes.," *Glia*, vol. 36, pp. 180–190, Nov 2001.

[57] A. Cornell-Bell, S. Finkbeiner, M. Cooper, and S. Smith, "Glutamate induces calcium waves in cultured astrocytes: long-range glial signaling," *Science*, vol. 247, no. 4941, pp. 470–473, 1990.

[58] A. Verkhratsky and H. Kettenmann, "Calcium signalling in glial cells," *Trends in Neurosciences*, vol. 19, no. 8, pp. 346–352, 1996.

[59] T. A. Weissman, P. A. Riquelme, L. Ivic, A. C. Flint, and A. R. Kriegstein, "Calcium waves propagate through radial glial cells and modulate proliferation in the developing neocortex.," *Neuron*, vol. 43, pp. 647–661, Sep 2004.

[60] M. V. L. Bennett, J. E. Contreras, F. F. Bukauskas, and J. C. Sáez, "New roles for astrocytes: gap junction hemichannels have something to communicate.," *Trends in neurosciences*, vol. 26, no. 11, pp. 610–617, 2003.

[61] V. Benfenati, M. Caprini, G. P. Nicchia, A. Rossi, M. Dovizio, C. Cervetto, M. Nobile, and S. Ferroni, "Carbenoxolone inhibits volume-regulated anion conductance in cultured rat cortical astroglia.," *Channels*, vol. 3, no. 5, pp. 323–336, 2009.

[62] J. C. Sáez, J. E. Contreras, F. F. Bukauskas, M. A. Retamal, and M. V. L. Bennett, "Gap junction hemichannels in astrocytes of the cns.," *Acta physiologica Scandinavica*, vol. 179, no. 1, pp. 9–22, 2003.

[63] A. Verkhratsky, R. C. Reyes, and V. Parpura, "Trp channels coordinate ion signalling in astroglia," *Reviews of physiology, biochemistry and pharmacology*, vol. 166, pp. 1–22, 2014.

[64] T. Voets, J. Prenen, J. Vriens, H. Watanabe, A. Janssens, U. Wissenbach, M. Bodding, G. Droogmans, and B. Nilius, "Molecular determinants of permeation through the cation channel trpv4," *Journal of Biological Chemistry*, vol. 277, no. 37, pp. 33704–33710, 2002.

[65] D. A. Ryskamp, P. Witkovsky, P. Barabas, W. Huang, C. Koehler, N. P. Akimov, S. H. Lee, S. Chauhan, W. Xing, R. C. Rentería, W. Liedtke, and D. Krizaj, "The polymodal ion channel transient receptor potential vanilloid 4 modulates calcium flux, spiking rate, and apoptosis of mouse retinal ganglion cells.," *The*

Journal of neuroscience : the official journal of the Society for Neuroscience, vol. 31, no. 19, pp. 7089–7101, 2011.

[66] A. Garcia-Elias, S. Mrkonjic, C. Jung, C. Pardo-Pastor, R. Vicente, and M. A. Valverde, "The trpv4 channel," *Mammalian Transient Receptor Potential (Trp) Cation Channels, Vol I*, vol. 222, pp. 293–319, 2014.

[67] R. Strotmann, C. Harteneck, K. Nunnenmacher, G. Schultz, and T. Plant, "Otrpc4, a nonselective cation channel that confers sensitivity to extracellular osmolarity," *Nature Cell Biology*, vol. 2, no. 10, pp. 695–702, 2000.

[68] X. Gao, L. Wu, and R. G. O'Neil, "Temperature-modulated diversity of trpv4 channel gating - activation by physical stresses and phorbol ester derivatives through protein kinase c-dependent and -independent pathways," *Journal of Biological Chemistry*, vol. 278, no. 29, pp. 27129–27137, 2003.

[69] J. Vriens, H. Watanabe, A. Janssens, G. Droogmans, T. Voets, and B. Nilius, "Cell swelling, heat, and chemical agonists use distinct pathways for the activation of the cation channel trpv4," *Proceedings of the National Academy of Sciences of the United States of America*, vol. 101, no. 1, pp. 396–401, 2004.

[70] H. Haeberle, L. A. Bryan, T. J. Vadakkan, M. E. Dickinson, and E. A. Lumpkin, "Swelling-activated ca2+ channels trigger ca2+ signals in merkel cells.," *PloS one*, vol. 3, no. 3, p. e1750, 2008.

[71] F. Vincent, A. Acevedo, M. Nguyen, M. Dourado, J. DeFalco, A. Gustafson, P. Spiro, D. Emerling, M. Kelly, and M. Duncton, "Identification and characterization of novel trpv4 modulators," *Biochemical and Biophysical Research Communications*, vol. 389, no. 3, pp. 490–494, 2009.

[72] R. Day, P. Kitchen, D. Owen, C. Bland, L. Marshall, A. Conner, R. Bill, and M. Conner, "Human aquaporins: Regulators of transcellular water flow," *Biochimica Et Biophysica Acta*, vol. 1840, no. 5, pp. 1492–1506, 2014.

[73] H. Pasantes-Morales and S. Cruz-Rangel, "Brain volume regulation: Osmolytes and aquaporin perspectives," *Neuroscience*, vol. 168, no. 4, pp. 871–884, 2010.

[74] E. Hansson and L. Ronnback, "Glial neuronal signaling in the central nervous system," *Faseb Journal*, vol. 17, no. 3, pp. 341–348, 2003.

[75] J. S. Guimaraes MZP, *TRPA1 : A Sensory Channel of Many Talents.* CRC Press Taylor & Francis, 2007.

[76] E. Shigetomi, O. Jackson-Weaver, R. T. Huckstepp, T. J. O'Dell, and B. S. Khakh, "Trpa1 channels are regulators of astrocyte basal calcium levels and long-term potentiation via constitutive d-serine release," *Journal of Neuroscience*, vol. 33, no. 24, pp. 10143–10153, 2013.

[77] E. Shigetomi, X. Tong, K. Kwan, D. Corey, and B. Khakh, "Trpa1 channels regulate astrocyte resting calcium and inhibitory synapse efficacy through gat-3," *Nature Neuroscience*, vol. 15, no. 1, pp. 70–U215, 2012.

[78] J. Chen and D. H. Hackos, "Trpa1 as a drug target–promise and challenges.," *Naunyn-Schmiedeberg's archives of pharmacology*, vol. 388, pp. 451–463, Apr 2015.

[79] S. M. Mueller-Tribbensee, M. Karna, M. Khalil, M. F. Neurath, P. W. Reeh, and M. A. Engel, "Differential contribution of trpa1, trpv4 and trpm8 to colonic nociception in mice.," *PloS one*, vol. 10, p. e0128242, Jul 2015.

[80] D. Lim, V. Ronco, A. A. Grolla, A. Verkhratsky, and A. A. Genazzani, "Glial calcium signalling in alzheimer's disease.," *Reviews of physiology, biochemistry and pharmacology*, vol. 167, pp. 45–65, 2014.

[81] V. Parpura and A. Verkhratsky, "Astrogliopathology: could nanotechnology restore aberrant calcium signalling and pathological astroglial remodelling?," *Biochimica et biophysica acta*, vol. 1833, no. 7, pp. 1625–1631, 2013.

[82] X. Tong, Y. Ao, G. C. Faas, S. E. Nwaobi, J. Xu, M. D. Haustein, M. A. Anderson, I. Mody, M. L. Olsen, M. V. Sofroniew, and B. S. Khakh, "Astrocyte kir4.1 ion channel deficits contribute to neuronal dysfunction in huntington's disease model mice.," *Nature neuroscience*, vol. 17, pp. 694–703, May 2014.

[83] S. E. Nwaobi, V. A. Cuddapah, K. C. Patterson, A. C. Randolph, and M. L. Olsen, "The role of glial-specific kir4.1 in normal and pathological states of the cns.," *Acta neuropathologica*, vol. 132, pp. 1–21, Jul 2016.

[84] L. Shang, C. J. Lucchese, S. Haider, and S. J. Tucker, "Functional characterisation of missense variations in the kir4.1 potassium channel (kcnj10) associated with seizure susceptibility.," *Brain research. Molecular brain research*, vol. 139, pp. 178–183, Sep 2005.

[85] M. C. Papadopoulos and A. S. Verkman, "Aquaporin-4 and brain edema.," *Pediatric nephrology (Berlin, Germany)*, vol. 22, pp. 778–784, Jun 2007.

[86] A. M. Fukuda and J. Badaut, "Aquaporin 4: a player in cerebral edema and neuroinflammation.," *Journal of neuroinflammation*, vol. 9, p. 279, Dec 2012.

[87] H. Ikeshima-Kataoka, "Neuroimmunological implications of aqp4 in astrocytes.," *International journal of molecular sciences*, vol. 17, Aug 2016.

[88] M. Potokar, J. Jorgačevski, and R. Zorec, "Astrocyte aquaporin dynamics in health and disease.," *International journal of molecular sciences*, vol. 17, Jul 2016.

[89] H.-G. Bernstein, J. Steiner, and B. Bogerts, "Glial cells in schizophrenia: pathophysiological significance and possible consequences for therapy.," *Expert review of neurotherapeutics*, vol. 9, pp. 1059–1071, Jul 2009.

[90] H.-G. Bernstein, J. Steiner, P. C. Guest, H. Dobrowolny, and B. Bogerts, "Glial cells as key players in schizophrenia pathology: recent insights and concepts of therapy.," *Schizophrenia research*, vol. 161, pp. 4–18, Jan 2015.

[91] G. Stuart, *Patch-Pipet Recording in Brain Slices*. John Wiley & Sons, Inc., 2001.

[92] Y. Zhao, S. Inayat, D. A. Dikin, J. H. Singer, R. S. Ruoff, and J. B. Troy, "Patch clamp technique: Review of the current state of the art and potential contributions from nanoengineering," *Proceedings of the Institution of Mechanical Engineers, Part N: Journal of Nanoengineering and Nanosystems*, vol. 222, no. 1, pp. 1–11, 2008.

[93] L. Avery, D. Raizen, and S. Lockery, "Electrophysiological methods.," *Methods in cell biology*, vol. 48, pp. 251–269, 1995.

[94] B. Sakmann and E. Neher, "Patch clamp techniques for studying ionic channels in excitable membranes.," *Annual review of physiology*, vol. 46, pp. 455–472, 1984.

[95] W. Commons, "From Wikimedia Commons, the free media repository, howpublished = "https://commons.wikimedia.org/wiki/File:Blausen_0213_CellularDiffusion.png", year = 2013, note = "[online; accessed 09-september-2016]"."

[96] A. Blau, A. Murr, S. Wolff, E. Sernagor, P. Medini, G. Iurilli, C. Ziegler, and F. Benfenati, "Flexible, all-polymer microelectrode arrays for the capture of cardiac and neuronal signals.," *Biomaterials*, vol. 32, no. 7, pp. 1778–1786, 2011.

[97] Y. H. Kim, G. H. Kim, N. S. Baek, Y. H. Han, A.-Y. Kim, M.-A. Chung, and S.-D. Jung, "Fabrication of multi-electrode array platforms for neuronal interfacing with bi-layer lift-off resist sputter deposition," *Journal of Micromechanics and Microengineering*, vol. 23, no. 9, p. 097001, 2013.

[98] M.-G. Liu, X.-F. Chen, T. He, Z. Li, and J. Chen, "Use of multi-electrode array recordings in studies of network synaptic plasticity in both time and space.," *Neuroscience bulletin*, vol. 28, pp. 409–422, Aug 2012.

[99] I. Suzuki, M. Fukuda, K. Shirakawa, H. Jiko, and M. Gotoh, "Carbon nanotube multi-electrode array chips for noninvasive real-time measurement of dopamine, action potentials, and postsynaptic potentials.," *Biosensors & bioelectronics*, vol. 49, pp. 270–275, Nov 2013.

[100] M. E. Spira and A. Hai, "Multi-electrode array technologies for neuroscience and cardiology.," *Nature nanotechnology*, vol. 8, no. 2, pp. 83–94, 2013.

[101] A. Gilletti and J. Muthuswamy, "Brain micromotion around implants in the rodent somatosensory cortex," *Journal of Neural Engineering*, vol. 3, no. 3, p. 189, 2006.

[102] M. Pekny and M. Nilsson, "Astrocyte activation and reactive gliosis.," *Glia*, vol. 50, no. 4, pp. 427–434, 2005.

[103] J. N. Turner, W. Shain, D. H. Szarowski, M. Andersen, S. Martins, M. Isaacson, and H. Craighead, "Cerebral astrocyte response to micromachined silicon implants.," *Experimental neurology*, vol. 156, no. 1, pp. 33–49, 1999.

[104] R. W. Griffith and D. R. Humphrey, "Long-term gliosis around chronically implanted platinum electrodes in the rhesus macaque motor cortex.," *Neuroscience letters*, vol. 406, no. 1-2, pp. 81–86, 2006.

[105] J. E. Burda and M. V. Sofroniew, "Reactive gliosis and the multicellular response to cns damage and disease.," *Neuron*, vol. 81, no. 2, pp. 229–248, 2014.

[106] F. Greve, S. Frerker, A. G. Bittermann, C. Burkhardt, A. Hierlemann, and H. Hall, "Molecular design and characterization of the neuron-microelectrode array interface.," *Biomaterials*, vol. 28, no. 35, pp. 5246–5258, 2007.

[107] M. L. Block, L. Zecca, and J.-S. Hong, "Microglia-mediated neurotoxicity: uncovering the molecular mechanisms.," *Nature reviews. Neuroscience*, vol. 8, no. 1, pp. 57–69, 2007.

[108] C. Grienberger and A. Konnerth, "Imaging calcium in neurons.," *Neuron*, vol. 73, pp. 862–885, Mar 2012.

[109] R. Rudolf, M. Mongillo, R. Rizzuto, and T. Pozzan, "Looking forward to seeing calcium.," *Nature reviews. Molecular cell biology*, vol. 4, pp. 579–586, Jul 2003.

[110] S. K. Kong and C. Y. Lee, "The use of fura 2 for measurement of free calcium concentration," *Biochemical Education*, vol. 23, no. 2, pp. 97–98, 1995.

[111] K. R. Gee, K. A. Brown, W. N. Chen, J. Bishop-Stewart, D. Gray, and I. Johnson, "Chemical and physiological characterization of fluo-4 ca(2+)-indicator dyes.," *Cell calcium*, vol. 27, pp. 97–106, Feb 2000.

[112] K. Kikuchi, "Design, synthesis and biological application of chemical probes for bio-imaging.," *Chemical Society reviews*, vol. 39, pp. 2048–2053, Jun 2010.

[113] C. N. Kanchiswamy, M. Malnoy, A. Occhipinti, and M. E. Maffei, "Calcium imaging perspectives in plants.," *International journal of molecular sciences*, vol. 15, pp. 3842–3859, Mar 2014.

[114] W. Wang, J. L. Collinger, M. A. Perez, E. C. Tyler-Kabara, L. G. Cohen, N. Birbaumer, S. W. Brose, A. B. Schwartz, M. L. Boninger, and D. J. Weber, "Neural interface technology for rehabilitation: exploiting and promoting neuroplasticity.," *Physical medicine and rehabilitation clinics of North America*, vol. 21, no. 1, pp. 157–178, 2010.

[115] R. V. Bellamkonda, S. B. Pai, and P. Renaud, "Materials for neural interfaces," *MRS Bulletin*, vol. 37, pp. 557–561, 2012.

[116] P. Kollmannsberger, C. M. Bidan, J. W. C. Dunlop, and P. Fratzl, "The physics of tissue patterning and extracellular matrix organisation: how cells join forces," *Soft Matter*, vol. 7, pp. 9549–9560, 2011.

[117] D. F. Williams, *Biofunctionality and Biocompatibility*. Wiley-VCH Verlag GmbH & Co. KGaA, 2006.

[118] S. Bonetti, A. Pistone, M. Brucale, S. Karges, L. Favaretto, M. Zambianchi, T. Posati, A. Sagnella, M. Caprini, S. Toffanin, R. Zamboni, N. Camaioni, M. Muccini, M. Melucci, and V. Benfenati, "A lysinated thiophene-based semiconductor as a multifunctional neural bioorganic interface," *Advanced Healthcare Materials*, vol. 4, no. 8, pp. 1190–1202, 2015.

[119] J. Isaksson, P. Kjäll, D. Nilsson, N. D. Robinson, M. Berggren, and A. Richter-Dahlfors, "Electronic control of ca2+ signalling in neuronal cells using an organic electronic ion pump.," *Nature materials*, vol. 6, no. 9, pp. 673–679, 2007.

[120] G. Lanzani, "Materials for bioelectronics: organic electronics meets biology.," *Nature materials*, vol. 13, pp. 775–776, Aug 2014.

[121] J. Rivnay, R. M. Owens, and G. G. Malliaras, "The Rise of Organic Bioelectronics," *Chemistry of Materials*, vol. 26, no. 1, SI, pp. 679–685, 2014.

[122] R. Capelli, J. Amsden, G. Generali, S. Toffanin, V. Benfenati, M. Muccini, D. Kaplan, F. Omenetto, and R. Zamboni, "Integration of silk protein in organic and light-emitting transistors," *Organic Electronics*, vol. 12, no. 7, pp. 1146–1151, 2011.

[123] H. Spanggaard and F. C. Krebs, "A brief history of the development of organic and polymeric photovoltaics," *Solar Energy Materials and Solar Cells*, vol. 83, no. 2-3, pp. 125 – 146, 2004.

[124] X. Pi, "Doping Silicon Nanocrystals with Boron and Phosphorus," *Journal of Nanomaterials*, 2012.

[125] A. Campana, T. Cramer, D. T. Simon, M. Berggren, and F. Biscarini, "Electrocardiographic recording with conformable organic electrochemical transistor fabricated on resorbable bioscaffold," *Advanced Materials*, vol. 26, no. 23, pp. 3874–3878, 2014.

[126] S.-C. Chang, Y.-J. Hsiao, T.-C. Lin, T.-S. Li, S.-A. Zeng, and C.-E. Yu, "Improving Power Conversion Efficiency of P3HT/PCBM based Organic Solar Cells by Optimizing Graphene Doping Concentration and Annealing Temperature," *International Journal of Electrochemical Science*, vol. 11, pp. 5819–5828, JUL 2016.

[127] B. Lüssem, M. Riede, and K. Leo, "Doping of organic semiconductors," *physica status solidi (a)*, vol. 210, no. 1, pp. 9–43, 2013.

[128] Y. S. Kim, E. K. Lee, K. Eun, and S.-H. Choa, "Electromechanical properties of amorphous in-zn-sn-o transparent conducting film deposited at various substrate temperatures on polyimide substrate," *Japanese Journal of Applied Physics*, vol. 54, no. 9, p. 095501, 2015.

[129] C.-W. Yang and J.-W. Park, "The cohesive crack and buckle delamination resistances of indium tin oxide (ito) films on polymeric substrates with ductile metal interlayers," *Surface and Coatings Technology*, vol. 204, no. 16-17, pp. 2761 – 2766, 2010.

[130] L. Groenendaal, F. Jonas, D. Freitag, H. Pielartzik, and J. R. Reynolds, "Poly(3,4-ethylenedioxythiophene) and its derivatives: Past, present, and future," *Advanced Materials*, vol. 12, pp. 481–494, 4 2000.

[131] M. Döbbelin, R. Marcilla, M. Salsamendi, C. Pozo-Gonzalo, P. M. Carrasco, J. A. Pomposo, and D. Mecerreyes

[132] J. Ouyang, C.-W. Chu, F.-C. Chen, Q. Xu, and Y. Yang, "High-conductivity poly(3,4-ethylenedioxythiophene):poly(styrene sulfonate) film and its application in polymer optoelectronic devices," *Advanced Functional Materials*, vol. 15, no. 2, pp. 203–208, 2005.

[133] J. Kim, J. Jung, D. Lee, and J. Joo, "Enhancement of electrical conductivity of poly(3,4-ethylenedioxythiophene)/poly(4-styrenesulfonate) by a change of solvents," *Synthetic Metals*, vol. 126, no. 2-3, pp. 311 – 316, 2002.

[134] K. Sun, S. Zhang, P. Li, Y. Xia, X. Zhang, D. Du, F. H. Isikgor, and J. Ouyang, "Review on application of pedots and pedot:pss in energy conversion and storage devices," *Journal of Materials Science: Materials in Electronics*, vol. 26, no. 7, pp. 4438–4462, 2015.

[135] P. Gkoupidenis, N. Schaefer, B. Garlan, and G. G. Malliaras, "Neuromorphic functions in pedot:pss organic electrochemical transistors," *Advanced Materials*, vol. 27, no. 44, pp. 7176–7180, 2015.

[136] J. Weickert, H. Sun, C. Palumbiny, H. C. Hesse, and L. Schmidt-Mende, "Spray-deposited pedot:pss for inverted organic solar cells," *Solar Energy Materials and Solar Cells*, vol. 94, no. 12, pp. 2371 – 2374, 2010.

[137] Y. Nagao, "Synthesis and properties of perylene pigments," *Progress in Organic Coatings*, vol. 31, no. 1, pp. 43 – 49, 1997.

[138] E. Kozma and M. Catellani, "Perylene diimides based materials for organic solar cells," *Dyes and Pigments*, vol. 98, no. 1, pp. 160 – 179, 2013.

[139] J. E. Anthony, A. Facchetti, M. Heeney, S. R. Marder, and X. Zhan, "n-Type Organic Semiconductors in Organic Electronics," *Advanced Materials*, vol. 22, no. 34, pp. 3876–3892, 2010.

[140] C. Rost, D. Gundlach, S. Karg, and W. Riess, "Ambipolar organic field-effect transistor based on an organic heterostructure," *Journal of Applied Physics*, vol. 95, no. 10, pp. 5782–5787, 2004.

[141] G. Barbarella, M. Melucci, and G. Sotgiu, "The versatile thiophene: An overview of recent research on thiophene-based materials," *Advanced Materials*, vol. 17, no. 13, pp. 1581–1593, 2005.

[142] A. R. Murphy and J. M. J. Fr'echet, "Organic semiconducting oligomers for use in thin film transistors," *Chemical Reviews*, vol. 107, no. 4, pp. 1066–1096, 2007.

[143] M.-H. Yoon, A. Facchetti, C. E. Stern, and T. J. Marks, "Fluorocarbon-modified organic semiconductors: molecular architecture, electronic, and crystal structure tuning of arene- versus fluoroarene-thiophene oligomer thin-film properties.," *Journal of the American Chemical Society*, vol. 128, pp. 5792–5801, May 2006.

[144] S. Cheylan, A. Fraleoni-Morgera, J. Puigdollers, C. Voz, L. Setti, R. Alcubilla, G. Badenes, P. Costa-Bizzarri, and M. Lanzi, "Study of a thiophene-based polymer for optoelectronic applications," *Thin solid films*, vol. 497, pp. 16–19, FEB 21 2006.

[145] H.-A. Ho, M. Béra-Ab'erem, and M. Leclerc, "Optical sensors based on hybrid dna/conjugated polymer complexes," *Chemistry - A European Journal*, vol. 11, no. 6, pp. 1718–1724, 2005.

[146] K. Nilsson and O. Inganäs, "Chip and solution detection of dna hybridization using a luminescent zwitterionic polythiophene derivative," *Nature Materials*, vol. 2, no. 6, pp. 419–424, 2003.

[147] H.-A. Ho and M. Leclerc, *Chemical and Biological Sensors Based on Polythiophenes*, pp. 813–831. John Wiley & Sons, Ltd, 2009.

[148] B. Liu and G. C. Bazan, "Homogeneous fluorescence-based dna detection with water-soluble conjugated polymers," *Chemistry of Materials*, vol. 16, no. 23, pp. 4467–4476, 2004.

[149] H. Ho, M. Boissinot, M. Bergeron, G. Corbeil, K. Dore, D. Boudreau, and M. Leclerc, "Colorimetric and fluorometric detection of nucleic acids using cationic polythiophene derivatives," *Angewandte Chemie - International Edition*, vol. 41, no. 9, pp. 1548–1551, 2002.

[150] V. Ho, B. W. Boudouris, B. L. McCulloch, C. G. Shuttle, M. Burkhardt, M. L. Chabinyc, and R. A. Segalman, "Poly(3-alkylthiophene) diblock copolymers with ordered microstructures and continuous semiconducting pathways.," *Journal of the American Chemical Society*, vol. 133, pp. 9270–9273, Jun 2011.

[151] W. Ma, C. Yang, X. Gong, K. Lee, and A. Heeger, "Thermally stable, efficient polymer solar cells with nanoscale control of the interpenetrating network morphology," *Advanced Functional Materials*, vol. 15, no. 10, pp. 1617–1622, 2005.

[152] D. Ghezzi, M. R. Antognazza, R. Maccarone, S. Bellani, E. Lanzarini, N. Martino, M. Mete, G. Pertile, S. Bisti, G. Lanzani, and F. Benfenati, "A polymer optoelectronic interface restores light sensitivity in blind rat retinas.," *Nature photonics*, vol. 7, pp. 400–406, May 2013.

[153] S. Sharma, G. Sharma, and J. Mikroyannidis, "Improved power conversion efficiency of bulk heterojunction poly(3-hexylthiophene):pcbm photovoltaic devices using small molecule additive," *Solar Energy Materials and Solar Cells*, vol. 95, no. 4, pp. 1219 – 1223, 2011.

[154] P. Vanlaeke, A. Swinnen, I. Haeldermans, G. Vanhoyland, T. Aernouts, D. Cheyns, C. Deibel, J. D'Haen, P. Heremans, J. Poortmans, and J. Manca, "P3ht/pcbm bulk heterojunction solar cells: Relation between morphology and electro-optical characteristics," *Solar Energy Materials and Solar Cells*, vol. 90, no. 14, pp. 2150 – 2158, 2006.

[155] D. Ghezzi, M. R. Antognazza, M. Dal Maschio, E. Lanzarini, F. Benfenati, and G. Lanzani, "A hybrid bioorganic interface for neuronal photoactivation.," *Nature communications*, vol. 2, p. 166, 2011.

[156] U. Hersel, C. Dahmen, and H. Kessler, "RGD modified polymers: biomaterials for stimulated cell adhesion and beyond," *Biomaterials*, vol. 24, no. 24, pp. 4385–4415, 2003.

[157] K. Sango, H. Horie, S. InoueE, Y. Takamura, and T. Takenaka, "Age-related changes of DRG neuronal attachment to extracellular matrix proteins in vitro.," *Neuroreport*, vol. 4, no. 6, pp. 663–666, 1993.

[158] W. Schoonveld, R. Stok, J. Weijtmans, J. Vrijmoeth, J. Wildeman, and T. Klapwijk, "Morphology of quaterthiophene thin films in organic field effect transistors," *Synthetic Metals*, vol. 84, no. 1-3, pp. 583–584, 1997.

[159] A. Mishra, C. Q. Ma, and P. Bauerle, "Functional oligothiophenes: molecular design for multidimensional nanoarchitectures and their applications," *Chemical Reviews*, vol. 109, no. 3, pp. 1141–1276, 2009.

[160] M. Melucci, M. Durso, L. Favaretto, M. L. Capobianco, V. Benfenati, A. Sagnella, G. Ruani, M. Muccini, R. Zamboni, V. Fattori, and N. Camaioni, "Silk doped with a bio-modified dye as a viable platform for eco-friendly luminescent solar concentrators," *RSC Advances*, vol. 2, pp. 8610–8613, 2012.

[161] S. Bonetti, M. Prosa, A. Pistone, L. Favaretto, A. Sagnella, I. Grisin, M. Zambianchi, S. Karges, A. Lorenzoni, T. Posati, R. Zamboni, N. Camaioni, M. Muccini, F. Mercuri, M. Melucci, and V. Benfenati, "A self-assembled lysinated perylene diimide film as multifunctional material for neural interfacing," *Journal of Materials Chemistry B*, vol. 4, pp. 2921–2932, 2016.

[162] L. Kergoat, B. Piro, M. Berggren, G. Horowitz, and M.-C. Pham, "Advances in organic transistor-based biosensors: from organic electrochemical transistors to electrolyte-gated organic field-effect transistors," *Analytical and Bioanalytical Chemistry*, vol. 402, no. 5, pp. 1813–1826, 2012.

[163] K. Melzer, M. Brandlein, B. Popescu, D. Popescu, P. Lugli, and G. Scarpa, "Characterization and simulation of electrolyte-gated organic field-effect transistors," *Faraday Discuss.*, vol. 174, pp. 399–411, 2014.

[164] D. M. Mattox, *Introduction*, pp. 1–24. William Andrew, 2010.

[165] H. P. Creighton J.R., *Introduction to Chemical Vapor Deposition (CVD)*, pp. 1–22. ASM International, 2001.

[166] "Spray deposition of organic semiconducting thin-films: Towards the fabrication of arbitrary shaped organic electronic devices," *Organic Electronics*, vol. 11, no. 6, pp. 1031 – 1038, 2010.

[167] H. N. Tsao and K. Muellen, "Improving polymer transistor performance via morphology control," *Chemical Society Reviews*, vol. 39, no. 7, pp. 2372–2386, 2010.

[168] R. G. Poulsen, "Plasma etching in integrated circuit manufacture - a review," *Journal of Vacuum Science & Technology*, vol. 14, no. 1, pp. 266–274, 1977.

[169] L. E. Scriven, "Physics and applications of dip coating and spin coating," *MRS Proceedings*, vol. 121, 1 1988.

[170] L. Basiricó, P. Cosseddu, B. Fraboni, and A. Bonfiglio, "Inkjet printing of transparent, flexible, organic transistors," *Thin Solid Films*, vol. 520, no. 4, pp. 1291 – 1294, 2011.

[171] H. Goldberg, R. Brown, D. Liu, and M. Meyerhoff, "Screen printing: a technology for the batch fabrication of integrated chemical-sensor arrays," *Sensors and Actuators B: Chemical*, vol. 21, pp. 171–183, SEP 1994.

[172] M. Barbaro, A. Caboni, P. Cosseddu, G. Mattana, and A. Bonfiglio, "Active devices based on organic semiconductors for wearable applications.," *IEEE transactions on information technology in biomedicine : a publication of the IEEE Engineering in Medicine and Biology Society*, vol. 14, pp. 758–766, May 2010.

[173] H. E. Katz and J. Huang, "Thin-Film Organic Electronic Devices," *Annual Review of Materials Research*, vol. 39, pp. 71–92, 2009.

[174] N. Kitamura, A. Konno, T. Kuwahara, and Y. Komagiri, "Nerve growth factor-induced hyperexcitability of rat sensory neuron in culture," *Biomedical Research*, vol. 26, no. 3, pp. 123–130, 2005.

[175] M. Y. Mulla, P. Seshadri, L. Torsi, K. Manoli, A. Mallardi, N. Ditaranto, M. V. Santacroce, C. Di Franco, G. Scamarcio, and M. Magliulo, "Uv crosslinked poly(acrylic acid): a simple method to bio-functionalize electrolyte-gated ofet biosensors," *Journal of Materials Chemistry B*, vol. 3, pp. 5049–5057, 2015.

[176] S. Casalini, F. Leonardi, T. Cramer, and F. Biscarini, "Organic field-effect transistor for label-free dopamine sensing," *Organic Electronics*, vol. 14, pp. 156–163, JAN 2013.

[177] M. Magliulo, D. De Tullio, I. Vikholm-Lundin, W. M. Albers, T. Munter, K. Manoli, G. Palazzo, and L. Torsi, "Label-free c-reactive protein electronic detection with an electrolyte-gated organic field-effect transistor-based immunosensor," *Analytical and Bioanalytical Chemistry*, vol. 408, no. 15, pp. 3943–3952, 2016.

[178] T. Cramer, B. Chelli, M. Murgia, M. Barbalinardo, E. Bystrenova, D. M. de Leeuw, and F. Biscarini, "Organic ultra-thin film transistors with a liquid gate for extracellular stimulation and recording of electric activity of stem cell-derived neuronal networks," *Physical Chemistry Chemical Physics*, vol. 15, no. 11, pp. 3897–3905, 2013.

[179] X. Strakosas, M. Bongo, and R. M. Owens, "The organic electrochemical transistor for biological applications," *Journal of Applied Polymer Science*, vol. 132, no. 15, pp. n/a–n/a, 2015.

[180] D. Khodagholy, J. Rivnay, M. Sessolo, M. Gurfinkel, P. Leleux, L. H. Jimison, E. Stavrinidou, T. Herve, S. Sanaur, R. M. Owens, and G. G. Malliaras, "High transconductance organic electrochemical transistors.," *Nature communications*, vol. 4, p. 2133, 2013.

[181] J. Liao, S. Lin, M. Zeng, and Y. Yang, "A miniature photoelectrochemical sensor based on organic electrochemical transistor for sensitive determination of

chemical oxygen demand in wastewaters," *Water Research*, vol. 94, pp. 296 – 304, 2016.

[182] V. Benfenati, S. Toffanin, R. Capelli, L. M. Camassa, S. Ferroni, D. L. Kaplan, F. G. Omenetto, M. Muccini, and R. Zamboni, "A silk platform that enables electrophysiology and targeted drug delivery in brain astroglial cells," *Biomaterials*, vol. 31, no. 31, pp. 7883–7891, 2010.

[183] P. S. S Ferroni, C Marchini and C. Rapisarda, "Two distinct inwardly rectifying conductances are expressed in long term dibutyryl-cyclic-amp treated rat cultured cortical astrocytes," *Febs Letters*, vol. 370, no. 3, pp. 282–282, 1995.

[184] C. Albuquerque, D. J. Joseph, P. Choudhury, and A. B. MacDermott, "Dissection, plating, and maintenance of cortical astrocyte cultures.," *Cold Spring Harbor protocols*, vol. 2009, Aug 2009.

[185] K. D. McCarthy and J. de Vellis, "Preparation of separate astroglial and oligodendroglial cell cultures from rat cerebral tissue.," *The Journal of cell biology*, vol. 85, pp. 890–902, Jun 1980.

[186] T. H. Burkey, C. M. Hingtgen, and M. R. Vasko, "Isolation and culture of sensory neurons from the dorsal-root ganglia of embryonic or adult rats," *Methods in Molecular Medicine*, vol. 99, pp. 189–202, 2004.

[187] T. Sakaba, A. Hazama, and Y. Maruyama, *Patch-Clamp Capacitance Measurements*, pp. 277–286. Tokyo: Springer Japan, 2012.

[188] V. Benfenati, G. P. Nicchia, M. Svelto, C. Rapisarda, A. Frigeri, and S. Ferroni, "Functional down-regulation of volume-regulated anion channels in aqp4 knockdown cultured rat cortical astrocytes," *Journal of Neurochemistry*, vol. 100, no. 1, pp. 87–104, 2007.

[189] V. Green, D. Stott, and M. Diack, "Assay for fluorescein diacetate hydrolytic activity: Optimization for soil samples," *Soil Biology and Biochemistry*, vol. 38, no. 4, pp. 693 – 701, 2006.

[190] R. J. Mullen, C. R. Buck, and A. M. Smith, "Neun, a neuronal specific nuclear protein in vertebrates.," *Development (Cambridge, England)*, vol. 116, pp. 201–211, Sep 1992.

[191] C. E. Van der Zee, H. B. Nielander, J. P. Vos, S. Lopes da Silva, J. Verhaagen, A. B. Oestreicher, L. H. Schrama, P. Schotman, and W. H. Gispen, "Expression of growth-associated protein b-50 (gap43) in dorsal root ganglia and sciatic nerve during regenerative sprouting.," *The Journal of neuroscience : the official journal of the Society for Neuroscience*, vol. 9, pp. 3505–3512, Oct 1989.

[192] R. Q. Frazer, R. T. Byron, P. B. Osborne, and K. P. West, "Pmma: an essential material in medicine and dentistry.," *Journal of long-term effects of medical implants*, vol. 15, no. 6, pp. 629–639, 2005.

[193] E. S. Ereifej, S. Khan, G. Newaz, J. Zhang, G. W. Auner, and P. J. VandeVord, "Characterization of astrocyte reactivity and gene expression on biomaterials

for neural electrodes.," *Journal of biomedical materials research. Part A*, vol. 99, pp. 141–150, Oct 2011.

[194] C. D. Lascola and R. P. Kraig, "Whole-cell chloride currents in rat astrocytes accompany changes in cell morphology.," *The Journal of neuroscience : the official journal of the Society for Neuroscience*, vol. 16, pp. 2532–2545, Apr 1996.

[195] M. Eickenscheidt, M. Jenkner, R. Thewes, P. Fromherz, and G. Zeck, "Electrical stimulation of retinal neurons in epiretinal and subretinal configuration using a multicapacitor array," *Journal of Neurophysiology*, vol. 107, no. 10, pp. 2742–2755, 2012.

[196] V. Benfenati, K. Stahl, C. Gomis-Perez, S. Toffanin, A. Sagnella, R. Torp, D. L. Kaplan, G. Ruani, F. G. Omenetto, R. Zamboni, and M. Muccini, "Biofunctional silk/neuron interfaces," *Advanced Functional Materials*, vol. 22, no. 9, pp. 1871–1884, 2012.

[197] R. Tapia and I. Velasco, "Ruthenium red as a tool to study calcium channels, neuronal death and the function of neural pathways," *Neurochemistry International*, vol. 30, no. 2, pp. 137–147, 1997.

[198] T. Sasaki, M. Naka, F. Nakamura, and T. Tanaka, "Ruthenium red inhibits the binding of calcium to calmodulin required for enzyme activation.," *The Journal of biological chemistry*, vol. 267, no. 30, pp. 21518–21523, 1992.

[199] G. Owsianik, K. Talavera, T. Voets, and B. Nilius, "Permeation and selectivity of trp channels.," *Annual review of physiology*, vol. 68, pp. 685–717, 2006.

[200] A. Mizuno, N. Matsumoto, M. Imai, and M. Suzuki, "Impaired osmotic sensation in mice lacking trpv4.," *American journal of physiology. Cell physiology*, vol. 285, pp. C96–101, Jul 2003.

[201] W. Liedtke and J. M. Friedman, "Abnormal osmotic regulation in trpv4-/- mice.," *Proceedings of the National Academy of Sciences of the United States of America*, vol. 100, pp. 13698–13703, Nov 2003.

[202] V. Benfenati, M. Caprini, M. Dovizio, M. N. Mylonakou, S. Ferroni, O. P. Ottersen, and M. Amiry-Moghaddam, "An aquaporin-4/transient receptor potential vanilloid 4 (aqp4/trpv4) complex is essential for cell-volume control in astrocytes.," *Proceedings of the National Academy of Sciences of the United States of America*, vol. 108, pp. 2563–2568, Feb 2011.

[203] O. Butenko, D. Dzamba, J. Benesova, P. Honsa, V. Benfenati, V. Rusnakova, S. Ferroni, and M. Anderova, "The increased activity of trpv4 channel in the astrocytes of the adult rat hippocampus after cerebral hypoxia/ischemia.," *PloS one*, vol. 7, p. e39959, Jun 2012.

[204] V. Meseguer, Y. A. Alpizar, E. Luis, S. Tajada, B. Denlinger, O. Fajardo, J.-A. Manenschijn, C. Fernández-Peña, A. Talavera, T. Kichko, B. Navia, A. Sánchez, R. Señarís, P. Reeh, M. T. Pérez-García, J. R. López-López, T. Voets, C. Belmonte, K. Talavera, and F. Viana, "Trpa1 channels mediate acute neurogenic inflammation and pain produced by bacterial endotoxins.," *Nature communications*, vol. 5, p. 3125, 2014.

[205] K. Nagata, A. Duggan, G. Kumar, and J. García-Añoveros, "Nociceptor and hair cell transducer properties of trpa1, a channel for pain and hearing.," *The Journal of neuroscience : the official journal of the Society for Neuroscience*, vol. 25, pp. 4052–4061, Apr 2005.

[206] L. Roux, A. Madar, M. M. Lacroix, C. Yi, K. Benchenane, and C. Giaume, "Astroglial connexin 43 hemichannels modulate olfactory bulb slow oscillations.," *The Journal of neuroscience : the official journal of the Society for Neuroscience*, vol. 35, pp. 15339–15352, Nov 2015.

[207] W. Fleischer, S. Theiss, J. Slotta, C. Holland, and A. Schnitzler, "High-frequency voltage oscillations in cultured astrocytes.," *Physiological reports*, vol. 3, May 2015.

COLOPHON

This document was typeset using the typographical look-and-feel `classicthesis` developed by André Miede. The style was inspired by Robert Bringhurst's seminal book on typography *"The Elements of Typographic Style"*.

http://code.google.com/p/classicthesis/

Figures were drawn using Microsoft Publisher, Microsoft Power Point or Adobe Creative Suite 6 and plots were generated with Origin 9.0.

DECLARATION

I hereby declare that I have completed the present thesis

"*Organic bio-electronics for interfacing, stimulating and recording of neural cells*"

independently, without help from others and without using resources other than indicated and named. All phrases that are taken directly or indirectly from other sources (incl. electronic resources), quoted verbatim or paraphrased are indicated accordingly.

I declare that the thesis in its present or a similar form has not been submitted to any other domestic or foreign university in connection with a doctoral application or for other examination purposes.

Bologna, March 31, 2017

Saskia Katharina Karges